DESIGNING REACTIVE OXYGEN SPECIES PRODUCING MATERIALS FOR CANCER AND WASTEWATER TREATMENTS

by

NIL KANATHA PANDEY

Presented to the Faculty of the Graduate School of

The University of Texas at Arlington in Partial Fulfillment

of the Requirements for the Degree of

DOCTOR OF PHILOSOPHY

THE UNIVERSITY OF TEXAS AT ARLINGTON

August 2021

Supervising Committee:

Dr. Wei Chen, Supervising Professor

Dr. Muhammad N. Huda

Dr. Zui Pan

Dr. Mingwu Jin

Dr. Yujie Chi

Dedicated to:

My parents Daya Ram Pandey and Til Kumari Pandey

Acknowledgments

I would like to express my deepest sense of gratitude and sincere appreciation to my supervising professor Dr. Wei Chen for his guidance, advice, and support throughout the course of my Ph.D. journey. I am highly impressed by his broad spectrum of knowledge not only in nanomedicine but also in several areas of science, which has inspired me to think and work beyond my comfort zone. Dr. Chen will be one of the people behind my every success in the future. Many thanks to Dr. Muhammad N. Huda, Dr. Zui Pan, Dr. Mingwu Jin, and Dr. Yujie Chi for their interest in my research and for taking the time to serve on my committee.

I would like to express my wholehearted thanks to all my professors and the whole staff of the Physics Department, including Ms. Stacey Cody and Mr. Victor Reece, for their direct or indirect support and assistance during my Ph.D. training. I would further like to extend my sincere appreciation and thanks to the Chair of the Physics department Dr. Alex Weiss and my academic advisor Dr. Qiming Zhang for their continuous encouragement, guidance, and support. I also would like to thank Dr. Suman Satyal for being a supportive lab coordinator.

In addition, I would like to thank all the present and past lab members of the Nano-Bio Physics Lab, especially Dr. Lalit Chudal, Dr. Sunil Sahi, Eric Amador, and Jonathan Phan, for their help in my research work. Their valuable suggestions helped in many ways to broaden my knowledge. I would also like to acknowledge all my co-authors for all their help and support throughout the research. I cannot forget my friends Dr. Ananta Chalise, Matthew Millard, and Tabin Gautam for making my life easier here at UTA.

I would like to express my deepest feelings toward my parents and all my friends and relatives for their continuous support and encouragement. I am forever indebted to my wife, Kamala, for her unconditional love, care, and support in all my endeavors. The completion of this work would not have been possible without her support and patience. Last but not least, a sweet thanks to my astounding kids Nirmal and Nisma for being a constant source of motivation in this journey.

August 8, 2021

Abstract

DESIGNING REACTIVE OXYGEN SPECIES PRODUCING MATERIALS FOR CANCER AND WASTEWATER TREATMENTS

Nil Kanatha Pandey, Ph.D.

The University of Texas at Arlington, 2021

Supervising Professor: Dr. Wei Chen

This dissertation is focused on using nanotechnology to improve conventional photodynamic therapy (PDT) and advanced oxidation processes (AOPs) for cancer and wastewater treatments, respectively. Even though PDT has a great potential for cancer treatment, the insufficient penetration depth of the external light source and hypoxic nature of the tumor microenvironment severely hinder PDT's applications in clinical settings. Fortunately, microwaves (MWs) offer a potential opportunity to overcome these limitations. In the first part of the dissertation, a facile synthesis method of copper-cysteamine (Cu-Cy) nanoparticles is discussed, and their reactive oxygen species (ROS) production and cancer cell killing performances upon MW exposure are investigated. Our results demonstrate that the new synthesis method not only decreased the synthesis time but also improved the efficacy of Cu-Cy nanoparticles for cancer treatment.

Another disadvantage of conventional PDT is that conventional photosensitizers usually suffer from aggregation-caused fluorescence quenching and a remarkable reduction in ROS generation in aqueous solutions. Intriguingly, aggregation-induced emission lumiogens (AIEgens) offer a potential opportunity to overcome this drawback. Accordingly, two AIEgens (**TPEPy-I**

and **TPEPy-PF6**) were designed, and their ROS production performance and cancer cell killing capabilities upon MW radiation were explored in a systematic way. For the first time, we found that these two AIEgens can generate ROS upon MW irradiation and can efficiently destroy cancer cells.

ROS also plays a vital role to degrade organic pollutants contained in wastewater. The third part of the dissertation investigates the oxidative degradation of various toxic and nonbiodegradable organic pollutants using Cu-Cy nanoparticles. We discovered that the catalytic effect of Cu-Cy can be enhanced upon MW exposure. Our findings showed that Cu-Cy nanoparticles are promising heterogeneous Fenton-like catalysts for wastewater treatment. Considering the facile and green synthesis method of Cu-Cy and the ability to degrade wide varieties of organic contaminants in a relatively short time, it is believed that this work provides a simple yet efficient and economical catalyst ideal for the removal of toxic organic pollutants from wastewater. Overall, this dissertation would be beneficial to the further development of fundamental research in the field of "ROS Science," which is an emerging scientific discipline.

Nil Kanatha Pandey, Ph.D.

The University of Texas at Arlington, 2021

Table of Contents

Contents

List of Figures

List of Schemes

List of Tables

Chapter 1

General Introduction

1.1. Reactive oxygen species (ROS): A brief introduction

ROS are oxygen-containing reactive molecules. There are two types of ROS: (1) free radicals, which contain one or more unpaired electrons in their outer molecular orbitals, such as superoxide radical ($\bullet O_2^-$) and ($\bullet$OH) hydroxyl radical, and (2) non-radicals, which do not have unpaired electrons but are chemically reactive and can be converted to radical ROS, such as singlet oxygen ($^1O_2$) and hydrogen peroxide (H_2O_2).

Molecular oxygen ($^3O_2$) is a paramagnetic diradical with two electrons occupying separate π antibonding orbitals with parallel spins (Figure 1.1). Most organic molecules are diamagnetic, with electron pairs of opposite spins. A spin restriction applies for $^3O_2$ to involve in redox reactions with other molecules or atoms as it has to accept a pair of electrons that have the same spin so they can fit into the vacant spaces in the π antibonding orbitals of $^3O_2$. Thus, $^3O_2$ cannot efficiently oxidize biomolecules through 2-electron process [1, 2]. However, $^3O_2$ can convert to more reactive oxygen-containing forms. Energy transfer to $^3O_2$ results in the production of the highly reactive $^1O_2$, which has paired electrons with opposite spins (Figure 1.1). Accordingly, the spin restriction is removed, thereby increasing the oxidizing capability of $^1O_2$ [1, 2].

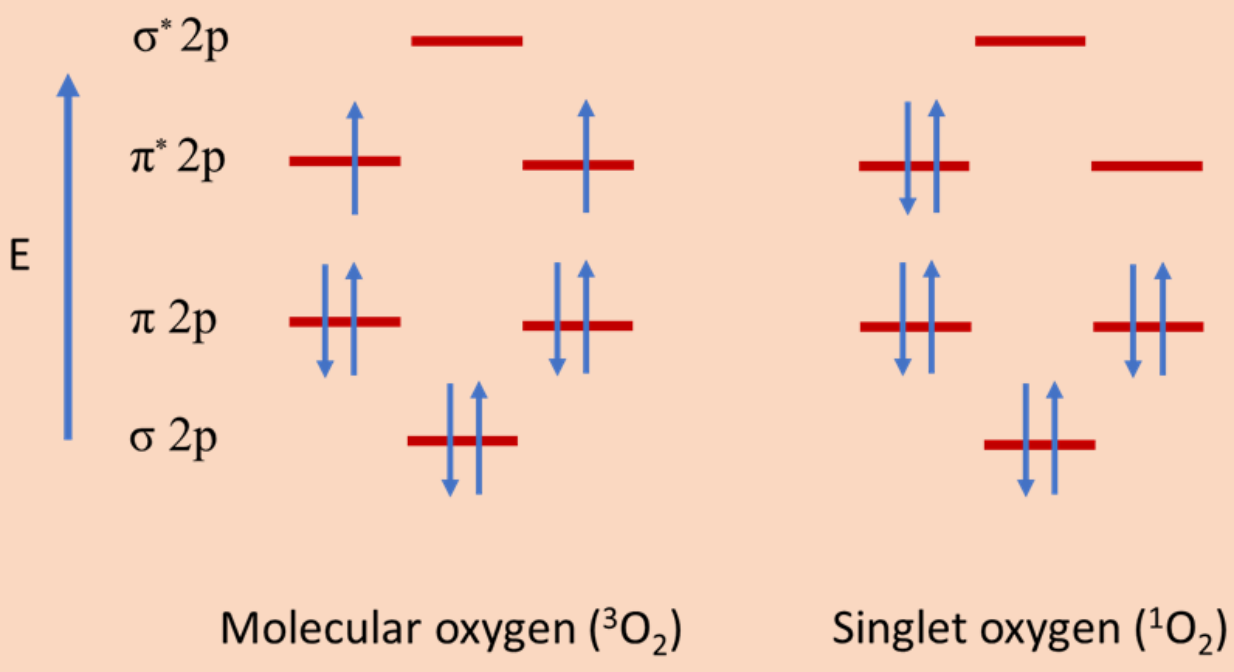

Figure 1.1. Schematic molecular orbital diagrams of molecular oxygen ($^3O_2$) and singlet oxygen ($^1O_2$).

As shown in Figure 1.2, the redox potential of $^3O_2$ is -0.16 V, making it relatively inert to most biomolecules. However, one-electron reduction of $^3O_2$ produces $\bullet O_2^-$, which has a higher reduction potential (+0.94 V). But $\bullet O_2^-$ has limited reactivity with electron-rich molecules due to its anionic charge [1, 2]. Upon protonation of $\bullet O_2^-$, perhydroxyl radical ($\bullet HO_2$) is formed. Although $\bullet HO_2$ has an enhanced reduction potential (+1.06 V) and is a better oxidizing agent, the biological effect of the $\bullet HO_2$ is minor owing to its low concentration at physiological pH [2]. One-electron reduction of $\bullet O_2^-$ results in the generation of H_2O_2. Despite the positive one-electron reduction potential of H_2O_2, it is considered relatively stable under physiological pH [1, 2]. On the contrary, •OH, with a one-electron reduction potential of +2.33 V, is one of the most powerful oxidizing agents reacting at virtually diffusion-limited rates with most organic matters [1, 2].

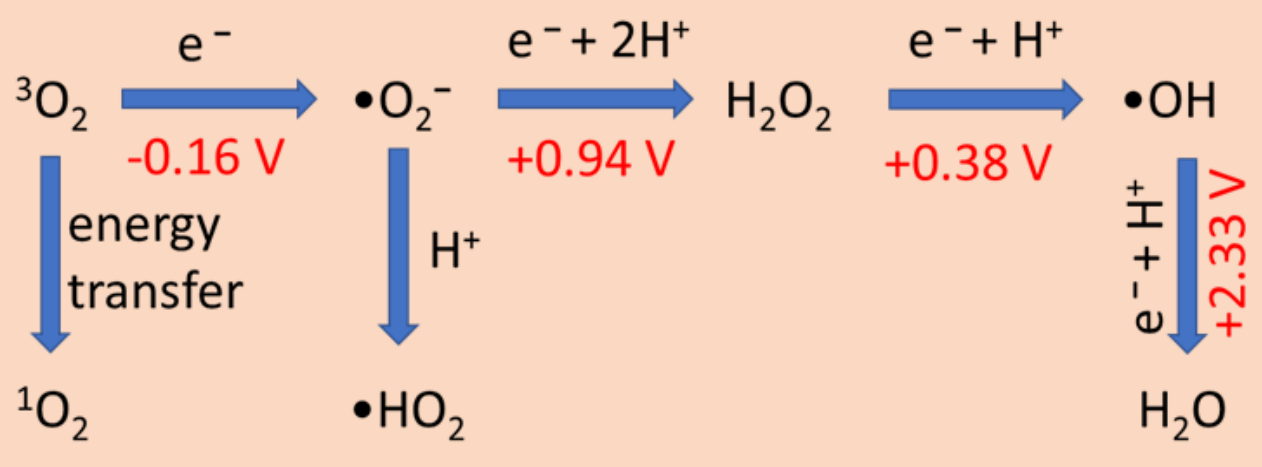

Figure 1.2. Generation of ROS via energy and electron transfer reactions.

In 1894, Fenton reported strong oxidation characteristics of hydrogen peroxide (H_2O_2) with ferrous ion (Fe^{2+}) [3, 4], which has opened an era of ROS chemistry [4]. In 1908, Warburg reported increased consumption of oxygen in sea urchin eggs after fertilization [4, 5]. It is considered the first milestone in ROS biology [4]. Since then, several types of research have shown the intercorrelations among ROS, nature, materials, and biological milieu. The interdependent relationship among ROS chemistry, ROS biology, and ROS nanotechnology have led to propose the concept of "ROS science," an emerging scientific discipline [4]. With the rapid development of nanotechnology, various materials that use the ROS-related mechanism for cancer and wastewater treatments have grown dramatically in recent years [4, 6, 7].

1.2. Cancer

Cancer is the second leading cause of death in the United States and is a major health problem worldwide [8]. In 2021, the projected numbers of new cancer cases and deaths in the United States are 1,898,160 (the equivalent of 5200 new cases per day) and 608,570 (correspond to more than 1600 deaths per day), respectively [8]. Even though the cancer mortality rate has declined

continuously due to reductions in smoking and improvements in early detection and treatment [8], innovative cancer detection and treatment modalities are urgently needed to further reduce the cancer death rate.

Although progress in basic research has led to the design of many novel therapeutic agents, many clinical trials for cancer, with some exceptions, have been able to detect only minor differences in therapeutic outcomes [9]. Additionally, the number of new clinically approved drugs is disappointingly low [9]. Such a frustrating success rate suggests that it is necessary to emphasize other existing but still underappreciated therapeutic modalities to improve clinical outcomes [9]. Although surgery, chemotherapy, and radiotherapy are major clinical treatment options, photodynamic therapy (PDT) can meet various currently unmet medical needs [9].

1.2.1. Photodynamic therapy (PDT)

PDT is a clinically approved promising cancer treatment modality with minimal invasiveness, low side effects, and negligible drug resistance. A photosensitizer (PS), a light of suitable wavelength, and molecular oxygen ($^3O_2$) are three key components required for PDT (Figure 1.3). None of these is individually toxic, but together they induce a photochemical reaction that generates highly cytotoxic $^1O_2$ and other types of ROS, which can cause apoptosis or necrosis to the treated cells. Additionally, PDT can be employed either alone or in combination with other therapies, such as chemotherapy, surgery, immunotherapy, or radiotherapy [9-11].

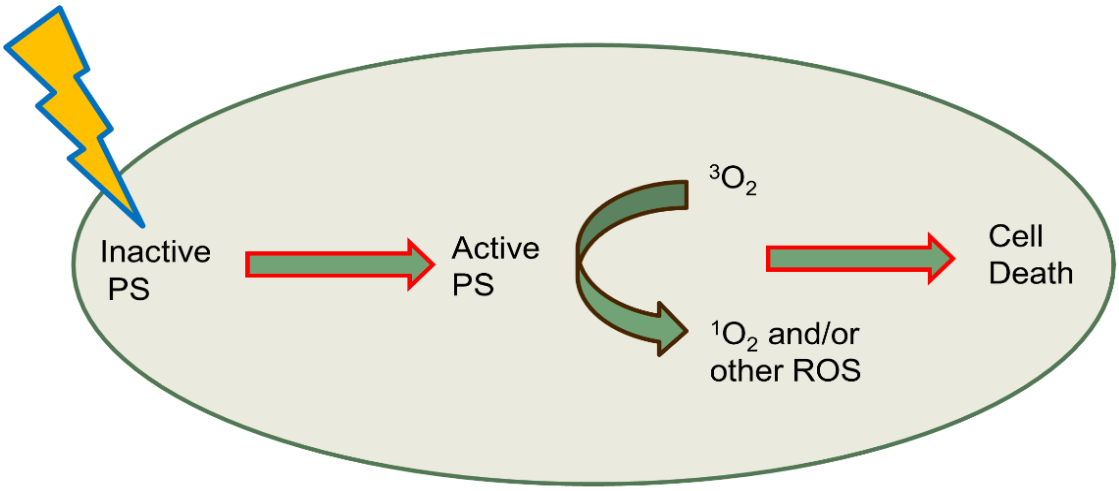

Figure 1.3. A schematic representation of photodynamic therapy (PDT).

1.2.2. A brief history of PDT

Light has been utilized as a therapeutic agent for thousands of years, but it was only in the last century that PDT was realized [12, 13]. Ancient Egyptian, Indian, and Chinese civilizations employed light to cure different diseases, such as rickets, psoriasis, and skin cancer [12, 13]. The ancient Greeks used to expose whole-body to sunlight to cure disease, and their popular pastime was lying nude in the sun [13]. At the end of the 19th century, Niels Finsen further used light to treat diseases. He discovered that smallpox can be treated using red light. He also employed UV light from the sun to cure cutaneous tuberculosis. This was considered the beginning of modern phototherapy, and in 1903, he was awarded a Nobel Prize in medicine for his discoveries [12, 13].

More than 100 years ago, scientists also found that a combination of certain chemicals and light could cause cell death. In 1900, Oscar Raab found the combination of light and acridine could elicit cytotoxic effects on infusoria. In 1903, Herman Von Tappeiner and A. Jesionek used a combination of eosin and white light to treat skin tumors. In 1907, they defined this phenomenon as ‘PHOTODYNAMIC ACTION’ [12, 13].

The most widely investigated PSs so far are porphyrins, which were discovered in the middle of the 19th century. In 1913, the German scientist Friedrich Meyer–Betz conducted the first study of PDT using porphyrins in humans. He injected 200 mg of hematoporphyrin on his own skin and noticed prolonged pain and swelling, specifically in light-exposed areas [12, 13]. The current era of PDT began with studies by Richard Lipson and co-workers at the Mayo Clinic in 1960 using 'hematoporphyrin derivative' (HPD) [14, 15]. One of the major milestones in PDT happened in 1975 when Thomas Dougherty and colleagues found eradication of tumor growth in mice [16]. In 1978, Dougherty reported the first controlled clinical study of PDT in humans, which was conducted at Roswell Park Cancer Institute, demonstrating that PDT could be used in the treatment of various malignant tumors [17]. Because of his great efforts on PDT, he is honored as the father of PDT [18].

In 1993, PDT was first approved in Canada using Photofrin as a PS for bladder cancer treatment [19]. Subsequent approvals for PDT with Photofrin for different kinds of cancer were obtained in the Netherlands, Japan, Germany, France, and USA [12]. With the successful application of hematoporphyrin for PDT, extensive efforts have been devoted to designing different PSs and exploring their application [20].

1.2.3. Mechanism of PDT

When a PS absorbs light of a suitable wavelength, the PS is excited from the singlet ground state to the singlet excited state. The excited PS is very unstable and loses energy by fluorescence and/or internal conversion to heat. Alternatively, the excited PS may undergo an intersystem crossing to form a more stable triplet excited state. The PS in the triplet state can either relax to the ground state by emitting phosphorescence or undergo energy transfer to molecular oxygen ($^3O_2$), which results in the formation of $^1O_2$, and the reaction is known as a Type II PDT. A Type

I process can also occur whereby the excited PS undergoes electron and/or proton transfer reaction with a substrate to produce radicals. The generated radicals then react with $^3O_2$ and produce different types of ROS [9, 10, 21]. A schematic Jablonski diagram is illustrated in Figure 1.4.

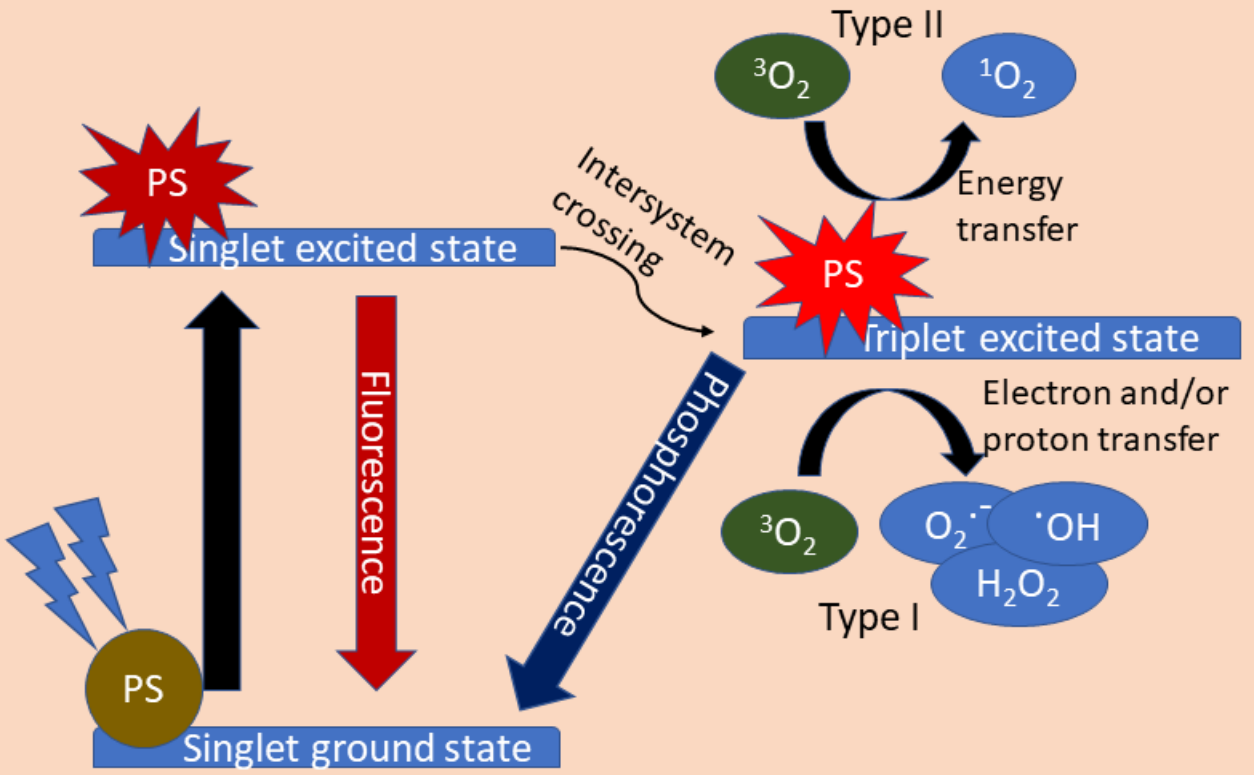

Figure 1.4. Jablonski diagram showing the principles of PDT.

1.2.4. ROS-manipulating strategies for cancer treatment

ROS are chemically reactive molecules that have vital roles in living organisms. However, ROS may function as a double-edged sword. A certain level of ROS is needed by both normal and cancer cells for immunity, cell proliferation, and differentiation, but ROS levels above or below lead to cytotoxicity [22, 23]. Increasing evidence indicates that most cancer cells exhibit an increased level of ROS when compared with their normal counterparts due to various reasons such

as increased metabolic activities, elevated cell signaling, and dysfunction of mitochondria. Recent studies have suggested that this biochemical property of cancer cells can be exploited to develop new drugs to target cancer cells preferentially and selectively. ROS-mediated cancer therapies, including ROS scavenging cancer therapy and ROS enhancing cancer therapy, have been suggested for cancer treatment [22, 23]. Even though both strategies can be utilized to destroy cancer cells, this dissertation is focused on the latter concept as accumulating evidence suggests that increasing ROS levels effectively kill cancerous cells.

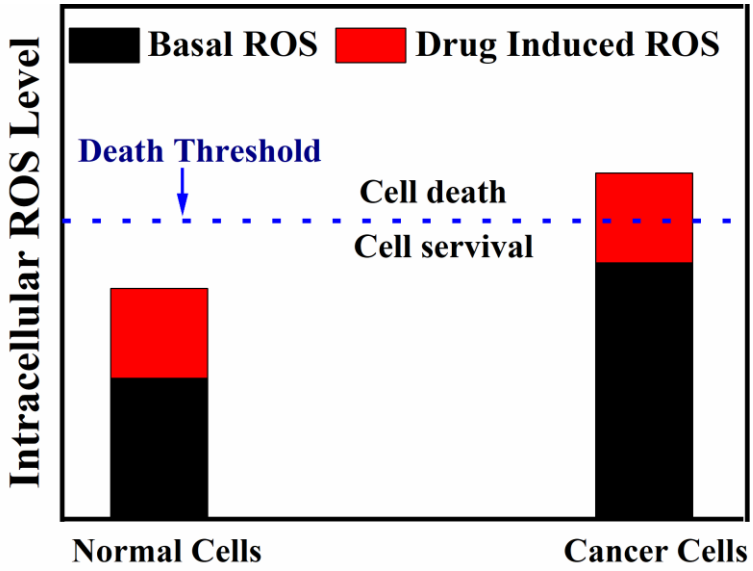

Figure 1.5. ROS threshold concept to explain the different susceptibility of normal versus cancer cells.

As depicted in Figure 1.5, when the levels of ROS are further increased therapeutically, ROS in cancer cells reach the death threshold earlier, and hence cancer cells are easier to destroy [22, 23]. Consequently, by taking the vulnerability of cancer cells from ROS attack, cancer cells can be selectively killed without causing remarkable cytotoxicity to the normal cells [22, 23]. ROS production is a common approach shared by most of the treatment modalities such as radiotherapy,

chemotherapy, chemodynamic therapy, sonodynamic therapy, and PDT [4, 20, 22, 23]. Among all therapeutic strategies, PDT-based cancer therapies have been extensively investigated [4, 20].

1.2.5. Effects of PDT on tumors

It is well accepted that there are three main inter-related pathways by which PDT mediates tumor destruction. Firstly, the ROS that is produced by PDT can destroy tumor cells. Secondly, the tumor vasculature can be shut down by PDT, leading to a tumor deprived of nutrients and oxygen supply. Thirdly, PDT can provoke an immune response against tumor cells. Although the relative contribution of each for the overall tumor destruction is not completely understood yet, the combination of these three mechanisms is needed for long-term tumor eradication [12].

1.2.6. Limitations of conventional PDT and possible solutions

Although the past 30 years have witnessed significant improvements in PDT and dozens of PSs have been approved for clinical trials, they are not considered first-line treatment options at the current time [24] due to some limitations of the existing PDT:

1.2.6.1. Penetration depth

Despite PDT's clinical promise, the limited penetration depth of light severely hinders PDT's practicality in clinical settings. Living tissues are highly complex and dynamic turbid media. In addition, various cells and tissues have their own unique optical properties. As different wavelengths penetrate skin and tissue differently, blue light penetrates less efficiently through tissue when compared with red and infrared light (Figure 1.6) [9].

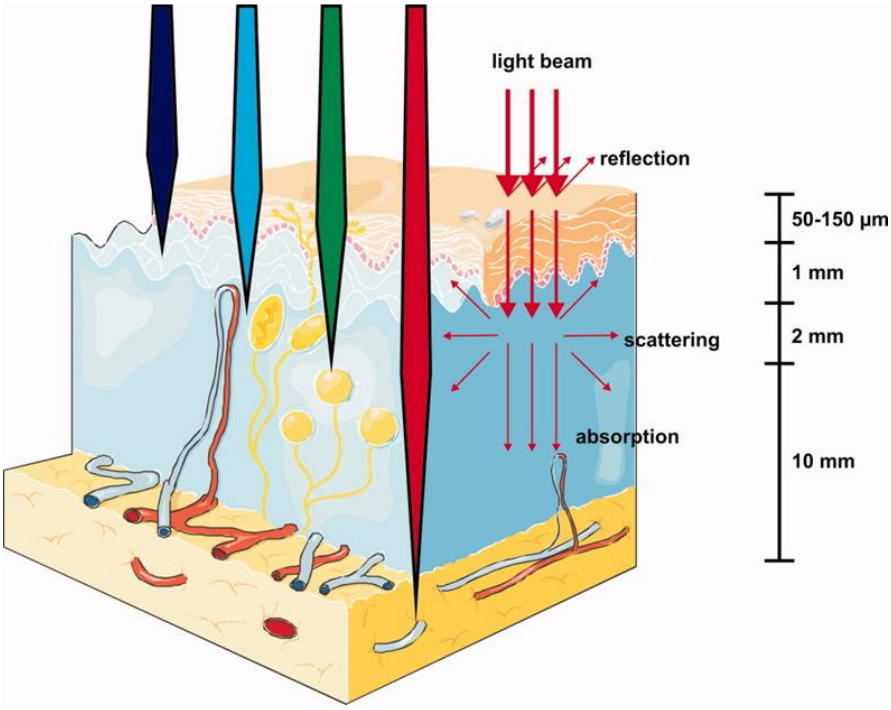

Figure 1.6. A schematic illustration of light penetration through tissues. Reproduced with permission [9].

Due to the strong light absorption of proteins and nucleic acids, a short wavelength of light such as UV light can only be used to treat superficial tumors [25]. With the increase in wavelength of light, the absorption of light by proteins and nucleic acids decreases significantly, but hemoglobin (a major absorber of visible light) has a strong light absorption in the visible region (<650 nm) [25, 26]. Furthermore, the absorption coefficient of water increases rapidly in the infrared region (primarily beyond 900 nm) because water is a major absorber of infrared light [25, 26]. Consequently, wavelengths in the range of 650-900 nm are called "NIR window" or "optical window" as hemoglobin and water molecules have their lowest absorption coefficient in this region (Figure 1.7) [25, 26]. However, light up to only ~800 nm can produce $^1O_2$ as longer wavelengths do not have sufficient energy to generate $^1O_2$ [9]. Although NIR light penetrates better than UV and visible light, NIR light cannot penetrate deeper than 1 cm in tissue while retaining

enough energy to generate $^1O_2$. To address the limited penetration depth of traditional PDT, several strategies have been employed. Recently, some groups, including we, have proposed the concept of using MWs with MW-responsive materials as MWs are able to penetrate deeper into tissues [27-35].

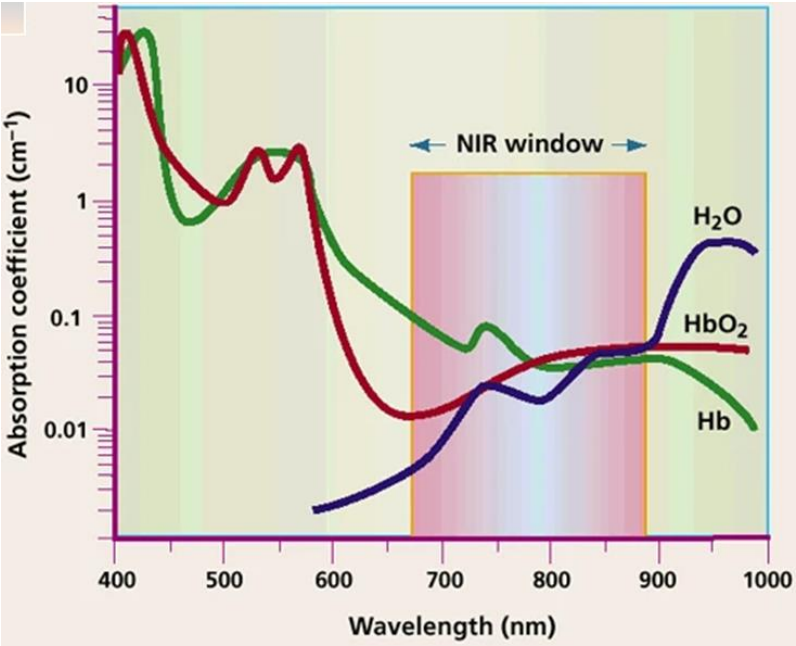

Figure 1.7. Absorption spectra of deoxyhemoglobin (Hb), oxyhemoglobin (HbO_2), and water molecules in the wavelength range of 400-1000 nm. Reproduced with permission [26].

1.2.6.2. Hypoxic nature of solid tumors

PDT efficacy is severely reduced in the context of a hypoxic environment because of the oxygen-dependent nature of PDT [20, 24, 36]. In recent years, a great effort has been devoted to overcoming tumor hypoxia during PDT. Among several strategies, thermal ablation has been recognized as one of the most effective cancer treatment approaches in synergistic therapy as it enhances the efficacy of chemotherapy, radiotherapy, immunotherapy, or PDT [24, 37, 38]. The effectiveness of the treatment can be improved if the blood supply to the tumor is enhanced through

mild heating [24, 37, 38]. Among various thermal therapies, MW ablation has gained considerable attention as a promising therapy in clinics due to its faster heat generation, broader heating zone, deeper penetration in tissues, maneuverability, less susceptibility to local heat tissues, and perfect capability of killing tumor cells [33, 39-41]. Additionally, MWs are capable of penetrating through the charged or desiccated tissues created during the ablative process. Moreover, MWs can propagate through many types of tissues, even those with high impedance tissues such as bone and lung that have been problematic for other ablation modalities [41].

1.2.6.3. Aggregation-caused quenching (ACQ) and reduction in ROS production

When chromophores aggregate, they generally exhibit two effects on their emissive behavior, aggregation-caused quenching (ACQ) and aggregation-induced emission (AIE). These photophysical phenomena are quite different from each other. DDPD (N,N-dicyclohexyl-1,7-dibromo-3,4,9,10-perylenetetracarboxylic diimide) is a typical example of ACQ luminophore (Figure 1.8a). It emits strong emission in a THF solution. However, its emission is quenched after adding water into THF (Figure 1.8a). When the water content is more than 60 vol%, the light emission from DDPD is completely quenched. Due to the hydrophobic nature of DDPD molecules, they aggregate in an aqueous solution. Their disk-like shapes favor the formation of excimeric species that usually decay via non-radiative relaxation channel (Figure 1.8b) [42, 43].

On the other hand, AIE luminogens (AIEgens) are a special type of molecules that are barely emissive in the molecularly dissolved state but emit strong emission in the aggregated state. HPS (hexaphenylsilole) is a typical example illustrating the AIE effect. It does not emit when its molecules are dissolved in a good organic solvent such as THF or a THF/water mixture with water content of less than 80 vol%. However, its emission is turned on when the water content is ~80 vol% (Figure 1.8c) due to the formation of aggregation of the HPS molecules in the aqueous

solution. Unlike ACQ luminophore, HPS adopts a twisted propeller-shaped structure (Figure 1.8d), which restricts the intermolecular π–π stacking interaction [42, 44].

Why can aggregate formation brighten the emission of AIEgens? According to fundamental knowledge of physics, any molecular movement (such as vibration and rotation) consumes energy. In a dilute solution, the six phenyl rings in HPS can dynamically rotate with respect to the central silole core (Figure 1.8d). As a result, the active intramolecular rotation consumes the excited-state energy via a non-radiative relaxation pathway, thereby quenching the fluorescence of HPS. However, such an intramolecular motion is restricted in the aggregate state, thus blocking the non-radiative relaxation pathway and opening the radiative decay pathway [42-44].

Conventional PSs such as methylene blue, Rose Bengal, and porphyrin derivatives generally aggregate in aqueous media, resulting in aggregation-caused fluorescence quenching and remarkable reduction in ROS generation [45-47]. Fortunately, the utilization of materials with AIE characteristics could provide a potential opportunity to surmount the aforementioned issue.

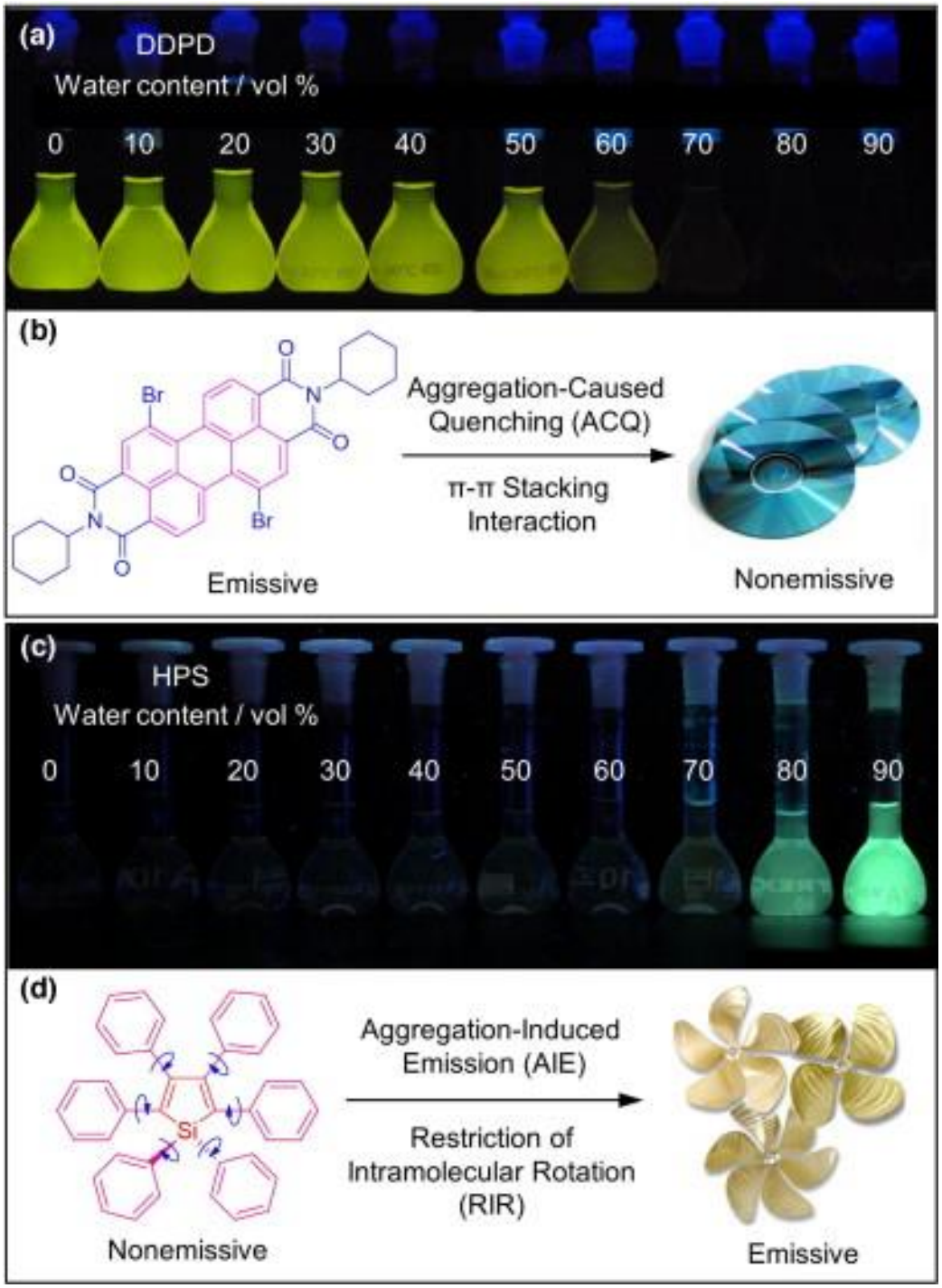

Figure 1.8. Photos of (a) DDPD with ACQ effect and (c) HPS with AIE effect in THF/water mixtures with various water contents. (b) The disk-shaped DDPD molecules are non-emissive in the aggregated state due to the strong intermolecular π-π stacking interaction. (d) The propeller-shaped HPS molecules are strongly emissive in the aggregate state due to the restriction of intramolecular rotation. Reproduced with permission [42].

1.2.7. Microwaves and ROS production

MW energy is a type of non-ionizing electromagnetic radiation with frequencies in the range of 0.3 GHz to 300 GHz. Since World War II, there have been significant developments in the use of MWs for heating materials. In contrast to conventional heating, MW dielectric heating is unique and offers several advantages, such as rapid heating, non-contact heating, volumetric heating, ease of control, and material selective heating [48, 49]. All domestic MW ovens and all dedicated MW reactors operate at a frequency of 2450 MHz (corresponding wavelength 12.24 cm and energy 1.02×10^{-5} eV). The energy of the MW photon is too low to break chemical bonds and is also lower than the energy of Brownian motion. As a result, MWs cannot cause chemical reactions [50]. However, MWs can enhance chemical reactions. The enhancement of chemical reactions by MW energy has gained considerable interest in organic chemistry in recent years. MW heating not only decreases reaction times but also diminishes side reactions, increases yields, and enhances reproducibility [50].

MWs have also been used in the medical and environmental fields [33, 35, 39, 40, 51]. Mounting evidence shows that MWs can produce ROS when MW-responsive materials are irradiated by MWs. Although there are many reports on MW-induced ROS, the exact mechanism of ROS production upon MW irradiation is not completely understood yet. Therefore, this dissertation extensively investigates MW-induced ROS production and attempts to propose possible mechanisms.

1.3. Wastewater treatment

With society's needs for a better life, environmental pollution has become one of the serious issues to be solved. Organic contaminants, such as organic dyes, phenols, pesticides, fertilizers,

hydrocarbons, oils, greases, and plasticizers, in wastewater have become one of the major environmental threats today [52, 53]. Once organic contaminants are discharged into the aquatic system, they cause a variety of environmental problems, including clogging sewage treatment plants and adversely affecting the aquatic biota [53, 54]. Additionally, these organic pollutants cannot be completely degraded using traditional wastewater treatment plants [55]. Accordingly, several persistent organic pollutants (POPs) have been detected in all types of aquatic systems, including drinking water, all over the world [55]. Therefore, effective and economical treatment technologies need to be developed to degrade organic contaminants before discharging the wastewater into the aquatic system.

Different methods have been investigated to deal with contaminated water, such as adsorption, flocculation, precipitation, advanced oxidation processes (AOPs), and biological methods [52, 53, 56]. Among them, AOPs have attracted increasing interest among researchers to degrade organic pollutants owing to their high efficiency, simplicity, easy handling, and good reproducibility [53, 56]. AOPs operate at near ambient conditions and produce highly oxidizing radical species (primarily •OH, one of the most powerful oxidants known) for complete degradation of organic contaminants into non-toxic products such as H_2O, CO_2, and inorganic salts [57]. Additionally, AOPs are promising technologies for decentralized systems [58]. Furthermore, AOPs facilitate easy integration with existing wastewater treatment technologies, such as filtration, coagulation, and biological treatment [57, 59].

Since the introduction of Fenton reactions by H. J. H. Fenton in 1894 [3], Fenton reagents (Fe^{2+} and H_2O_2; Eqs. (1.1) and (1.2)) have been extensively investigated to degrade organic pollutants during wastewater purification [57]. However, the practical applications have been hindered by a narrow pH window (~2.5-3.5) and the generation of ferric hydroxide sludge at

circumneutral pH [57, 60]. As both homogenous and heterogeneous iron-based catalysts suffer from severe practical disadvantages, continuous research efforts have concentrated on investigating alternative metal catalysts to replace iron [57].

$$Fe^{2+} + H_2O_2 \rightarrow Fe^{3+} + \bullet OH + OH^- \ (k = 63\text{—}76\ M^{-1}s^{-1}) \quad (1.1)$$

$$Fe^{3+} + H_2O_2 \rightarrow Fe^{2+} + \bullet HO_2 + H^+ \ (k = 0.001\text{—}0.01\ M^{-1}s^{-1}) \quad (1.2)$$

Recently, Cu-based Fenton-like catalysts have attracted great attention owing to their superior catalytic activity in a broader pH range when compared with Fe^{2+} [57, 61]. In addition, as can be seen in Eqs. (1.1) and (1.3), the reaction rate of Cu^+ with H_2O_2 ($10^4\ M^{-1}s^{-1}$) is remarkably higher than that of Fe^{2+} (63—76 $M^{-1}s^{-1}$).

$$Cu^+ + H_2O_2 \rightarrow Cu^{2+} + \bullet OH + OH^- \ (k = 1.0 \times 10^4\ M^{-1}s^{-1}) \quad (1.3)$$

$$Cu^{2+} + H_2O_2 \rightarrow Cu^+ + \bullet HO_2 + H^+ \ (k = 4.6 \times 10^2\ M^{-1}s^{-1}) \quad (1.4)$$

Consequently, if Cu-based heterogeneous catalysts are to be employed for wastewater treatment, we should use Cu with oxidation state +1 as the reaction rate of Cu^+ is ~22 times faster than that of Cu^{2+} (Eqs. (1.3) and (1.4)) [57]. Copper-cysteamine (Cu-Cy) having oxidation state +1 is a novel nanoparticle that was invented by our lab in 2014 [62], which can produce ROS upon different excitation sources, such as UV light [63], X-rays [64-67], microwaves [29, 34], and ultrasound [68]. Additionally, Cu-Cy nanoparticles can destroy bacteria upon UV irradiation [69]. Moreover, Cu-Cy nanoparticles can be used as a heterogeneous Fenton-like catalyst for cancer treatment [70]. Our recent study further reveals that Cu-Cy nanoparticles can enhance the anticancer effect of disulfiram [71]. However, Cu-Cy nanoparticles for oxidative degradation of recalcitrant organic pollutants have never been investigated before.

Considering that ROS plays a crucial role to degrade toxic organic contaminants contained in wastewater, we hypothesized that Cu-Cy nanoparticles could be used to degrade organic pollutants using the same ROS-mediated mechanism that we utilized to destroy cancer and bacteria cells. In the fourth chapter of this dissertation, oxidative degradation of two organic dyes, rhodamine B (RhB) and methylene blue (MB), and one nitroaromatic pollutant, 4-nitrophenol (4-NP), by using Cu-Cy nanoparticles with the assistance of H_2O_2 is presented. Also, the effect of MW on the rate of degradation of RhB and 4-NP is also investigated. Brief introductions and toxicities of RhB, MB, and 4-NP are discussed in the following paragraphs.

RhB ($C_{28}H_{31}N_2O_3Cl$) is a synthetic cationic dye (Figure 1.9a) widely utilized as a colorant in several industries such as textile, plastic, paper, leather, cosmetics, and food. The discharge of RhB into the aquatic system results in wastewater with high toxicity and low transparency. It can irritate the eyes, skin, and respiratory system [72, 73]. Furthermore, it is not only carcinogenic but also toxic to the nervous and reproductive systems. As it is harmful even at very low concentrations, RhB has to be treated from the wastewater before releasing it to any aquatic system [72, 73].

MB ($C_{16}H_{18}ClN_3S$) is a cationic dye (Figure 1.9b) extensively used in the textile, paper, leather, and printing industries. The main toxicity of MB includes fever, headache, vomiting, mental confusion, and high blood pressure [74]. It can also cause skin and severe eye irritation. Moreover, the mutagenic effect of MB has also been found [75].

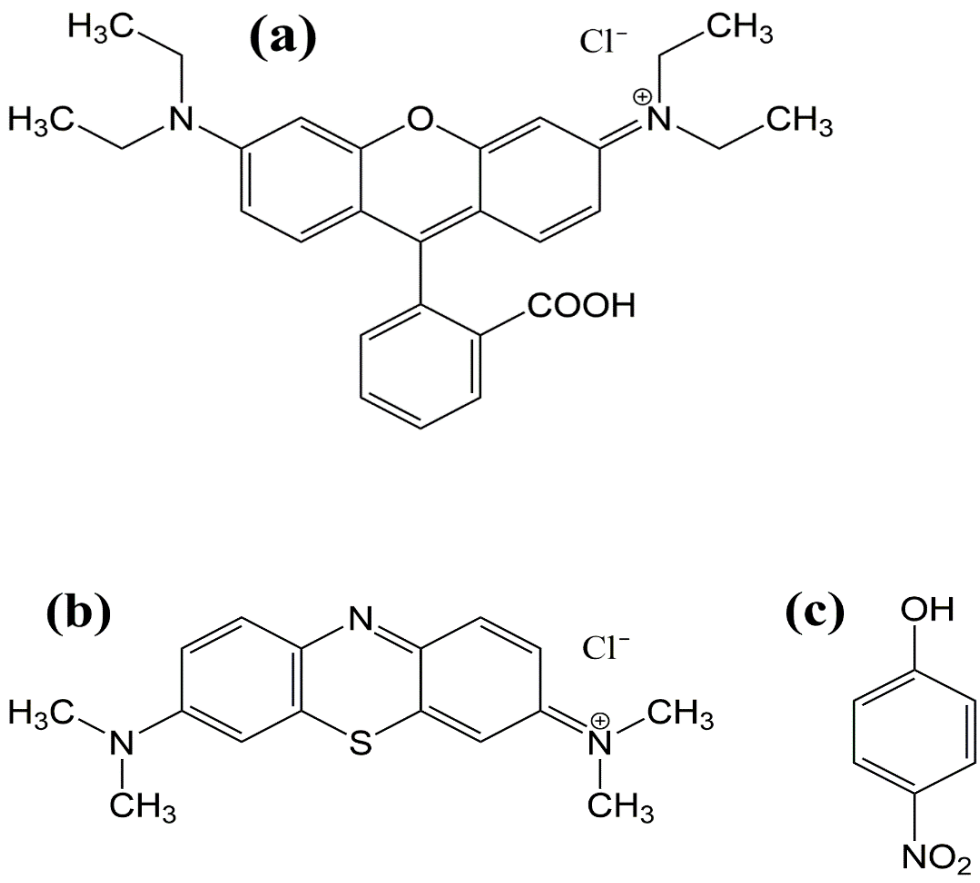

Figure 1.9. Molecular structures of (a) rhodamine B (RhB), (b) methylene blue (MB), and (c) 4-nitrophenol (4-NP).

4-NP ($C_6H_5NO_3$) is used in the manufacturing of several products such as pharmaceutical drugs, fungicides, insecticides, pesticides, explosives, dyes, and industrial solvents. As a result, 4-NP and its derivatives are common recalcitrant pollutants in various aquatic systems. Due to 4-NP's non-degradable, carcinogenic, and intensive toxic effects, 4-NP has been identified as the priority pollutant by the U.S. Environmental Protection Agency [76, 77].

Chapter 2

(Published in Journal of Materials Chemistry B)

A Facile Method for the Synthesis of Copper-Cysteamine Nanoparticles and Study of ROS Production for Cancer Treatment

Nil Kanatha Pandey,[a] Lalit Chudal,[a] Jonathan Phan,[a] Liangwu Lin,[b] Omar Johnson,[a] Meiying Xing,[a] J. Ping Liu,[a] , Haibin Li,[a,c] Xuejing Huang,[a] Yang Shu*[d] and Wei Chen*[a]

[a]Department of Physics, University of Texas at Arlington, Arlington, Texas 76019, USA

[b]Laboratory on High-Strength Structural Materials, Central South University, Changsha 410083, P. R. China

[c]School of Materials Science and Engineering, Changsha University of Science and Technology, Changsha 410114, People's Republic of China

[d]Research Center for Analytical Sciences, Department of Chemistry, College of Sciences, Northeastern University, Shenyang 110819, China

*Corresponding authors

Email: weichen@uta.edu; shuyang@mail.neu.edu.cn

Reproduced from Ref. Pandey, N. K., Chudal, L., Phan, J., Lin, L., Johnson, O., Xing, M., ... & Chen, W. (2019). A facile method for the synthesis of copper–cysteamine nanoparticles and study of ROS production for cancer treatment. Journal of Materials Chemistry B, 7(42), 6630-6642, with permission from the Royal Society of Chemistry. All the authors have permission to use in the dissertation.

Abstract

Copper-cysteamine (Cu-Cy) is a novel sensitizer that can be excited by ultraviolet (UV) light, microwave (MW), ultrasound, and X-rays to generate highly toxic reactive oxygen species (ROS) for cancer cell destruction. The purpose of this study is to present a facile method of the synthesis of Cu-Cy nanoparticles. Interestingly, we were able to decrease both the stirring and heating time by about 24 and 6 times, respectively, thus making Cu-Cy nanoparticles more economical than what was reported before. DABCO, a well-known singlet oxygen quencher, showed that the majority of ROS produced by Cu-Cy nanoparticles under UV and MW exposures were singlet oxygen. Moreover, ROS generated by Cu-Cy nanoparticles under UV and MW exposures were confirmed by a known ROS tracking agent, dihydrorhodamine 123, further serving as an additional piece of evidence that Cu-Cy is a promising ROS generating agent to destroy cancer cells as well as bacteria or viruses by a radical therapeutic approach. Additionally, for the first time, the hydroxyl radical ($^{\bullet}OH$) produced by Cu-Cy nanoparticles under MW activation was proved by a photoluminescence (PL) technique using coumarin as a probe molecule. Remarkably, newly synthesized nanoparticles were found to be much more effective for producing ROS and killing cancer cells, suggesting that the new method may have increased the reactivity of the Cu-Cy nanoparticles due to an overall size reduction. Overall, the new method not only reduced synthesis time but also enhanced the effectiveness of the Cu-Cy nanoparticles.

Keywords: Copper-Cysteamine; Photodynamic Therapy; Coumarin; Dihyrorhodamine 123; Microwave; CytoViva; Reactive Oxygen Species; Singlet Oxygen; Hydroxyl radical; DABCO

2.1. Introduction

Transition metal complexes have been extensively studied since the last few decades and have received increasing interest in modern science and industry because of their diverse applications, such as light emitting devices, solar cells, cosmetics, biological imaging, and therapeutic agents [78-84]. Among these transition metal complexes, Cu(I) metal has attracted considerable attention among researchers due to its low cost, low toxicity, and abundance [85-87]. Although some copper(I) complexes using cysteamine as a ligand have been published [88-90], our Cu-Cy [62], $Cu_3Cl(SR)_2$ (R= $CH_2CH_2NH_2$), is different from previously reported copper cysteamine complexes. Specifically, these Cu-Cy particles have strong photoluminescence and X-ray luminescence, whereas no luminescence has been reported for previous copper cysteamine complexes [88-90].

It has been found that the Cu-Cy nanoparticles can be activated by UV light [62, 63, 91], X-rays [62, 65, 91, 92], MW [34], and ultrasound [68] and produce highly cytotoxic ROS for cancer treatment. In addition to treating superficial and deep cancers, a more recent study has demonstrated that Cu-Cy nanoparticles are very effective for destroying gram-positive bacteria [93]. Moreover, Cu-Cy has been used to produce a white emitting phosphor under a single excitation wavelength (365 nm) from the composite of a graphitic-phase nitrogen carbon (g-C_3N_4) and Cu-Cy as discussed in the literature [94]. Furthermore, in the work published in a study of Dai *et al.*, 2017 [95], the authors reported a composite made of light emitting graphene quantum dots and Cu-Cy phosphors for enhanced white light emitting diodes under a single excitation wavelength.

These preliminary results demonstrate that Cu-Cy nanoparticles have tremendous potential for cancer theranostics and other important applications across various fields, thus motivating us to work further on Cu-Cy. Here, as a continuation of our study on Cu-Cy to develop cheaper and increasingly efficient products for various applications, we report a simpler and faster method for synthesizing Cu-Cy nanoparticles than previously reported [62].

A certain level of ROS is required by both cancer and normal cells for immunity, cell proliferation, and differentiation, while ROS are toxic to both cancer and normal cells at high concentration. When both cancer and normal cells are exposed to the same amount of exogenous ROS, the intra-cellular ROS level in cancer cells reach the cell-death threshold earlier to induce cell death than that in healthy cells owing to a higher basal ROS level in cancer cells [23, 96, 97]. Therefore, by taking the vulnerability of cancer cells from ROS attack using ROS-mediated therapeutic strategies, cancer cells can be selectively destroyed without causing significant toxicity to healthy cells [23, 96, 97]. The same approach could be extended to infectious diseases caused by bacteria [97]. Cu-Cy nanoparticles could be a promising agent to target cancer and bacteria cells through ROS-mediated mechanisms. However, as a new sensitizer, the exact mechanism and types of ROS produced by Cu-Cy nanoparticles under different excitation sources are not fully understood yet, and more research is still needed in this area to make it clear. In the present study, we have also attempted to understand the ability, mechanism, and types of ROS produced by Cu-Cy nanoparticles under UV and MW irradiations.

2.2. Experimental section

2.2.1. Materials

Copper chloride dihydrate ($CuCl_2.2H_2O$), cysteamine hydrochloride, sodium hydroxide (NaOH), polyethylene glycol 4000 (PEG-4000), p-nitrosodimethylaniline (RNO), imidazole (ID), 1,4-diazabicyclo[2.2.2]octane (DABCO), coumarin (COU), dihydrorhodamine 123 (DHR), and titanium dioxide (TiO_2, 21 nm primary particle size) were received from Sigma-Aldrich, USA. Likewise, paraformaldehyde (PFA) (4% in PBS) was purchased from Alfa Aesar. Zinc oxide (ZnO, 30±10 nm) was obtained from the Aladdin Industrial Corporation, China.

2.2.2. Synthesis of Cu-Cy nanoparticles

In a 250 mL 3-necked round bottom flask, 273 mg of $CuCl_2.2H_20$ was dissolved in 50 mL of DI water under vigorous magnetic stirring at room temperature. After dissolving $CuCl_2.2H_20$, 381 mg of cysteamine hydrochloride was introduced into the solution followed by the addition of 40 mg of PEG-4000 under a nitrogen (N_2) environment. After that, the pH value was adjusted to 7 by drop-wise addition of a 1 M solution of NaOH under the nitrogen environment. Once the pH was adjusted, the inert environment was removed. The solution was stirred at room temperature for about 5 min until the color turned to deep violet as a result of oxidation. Afterward, the solution was heated at the boiling point of water for 5 min under the inert environment with vigorous magnetic stirring. The solution was then allowed to cool to room temperature. The Cu-Cy particles were obtained by centrifuging at 12,000 rpm for 10 min and washing with DI water and ethanol 3 times. The obtained product was then dried completely in a vacuum oven at 40 ^{0}C overnight. The obtained powder was re-dispersed in DI water using a bath sonicator for 1 h. Large sized particles

were discarded by centrifugation and Cu-Cy nanoparticles were collected from the supernatant. The synthesis sketch of the Cu-Cy nanoparticles is shown in Scheme 2.1.

2.2.3. UV-Vis absorption and fluorescence spectroscopy

The optical absorption spectrum of Cu-Cy nanoparticles dispersed in DI water was measured using a Shimadzu UV-2450 UV-Vis spectrophotometer. The photoluminescence spectra of as-synthesized Cu-Cy nanoparticles suspended in DI water were taken by a Shimadzu RF-5301PC spectrofluorophotometer. The emission spectrum of the sample dispersed in DI water was performed by exciting the sample at 365 nm, whereas the excitation spectra were obtained using wavelengths of emission at 607 nm and 633 nm.

2.2.4. X-ray luminescence measurement

A light-proof X-ray cabinet equipped with an optic fiber connection to an outside detector was used to record X-ray luminescence. The X-ray irradiation (90 kV and 5 mA) was performed using a Faxitron RX-650 (Faxitron X-ray Corp, IL, USA). The X-ray luminescence spectrum was measured using a QE65000 spectrometer (Ocean Optics Inc, Dunedin, FL, USA), connected to the X-ray chamber using a 0.6 mm core diameter, P600-2-UV-Vis fiber optic (Ocean Optics Inc, Dunedin, FL, USA).

2.2.5. X-ray powder diffraction (XRD)

X-ray powder diffraction with a 2θ angle ranging from 5^0 to 80^0 was performed via a Rigaku Ultima IV diffractometer with Cu K_α radiation (λ = 0.15406 nm) operated at 40 kV and 40 mA at a step size of 0.02 degree/sec. The sample for the XRD was prepared by depositing the sample solution on a glass substrate and allowed to dry at room temperature.

2.2.6. Transmission electron microscopy (TEM)

For TEM observations, one drop of the solution containing as-synthesized Cu-Cy nanoparticles were dropped onto the amorphous carbon film supported on a copper grid and allowed to dry overnight at room temperature and the TEM images of the nanoparticles were recorded by a JEM-2100 HR transmission electron microscope (TEM, JEOL Ltd., Japan).

2.2.7. ROS measurement in aqueous solution using RNO-ID method

The imidazole plus RNO (RNO-ID) method [98], a simple but sensitive spectrophotometric method, was employed to probe ROS production under UV (360 nm) and MW exposures. RNO's absorption was monitored at 440 nm by using the UV-Vis spectrophotometer after particular time intervals of exposure of UV light and three different powers of MW (2, 5, and 10 W). MW was applied through a radiator probe using a microwave therapy apparatus (WB-3100AI, BXING, China). Briefly, the RNO-ID stock solution was prepared as follows: 0.45 mg of RNO and 16.34 mg of ID were separately dissolved into 30 mL DI water, which were air saturated by sufficient air bubbling for 20 min. The RNO-ID solution was subsequently prepared by taking 1 mL of RNO, 1 mL of ID, and 1 mL of the testing solution (Cu-Cy, Cu-Cy + DABCO, DABCO, $CuCl_2.2H_2O$, TiO_2 or ZnO). For the control, 1 mL of DI water was taken instead of the testing solution.

2.2.8. Detection of ROS using dihydrorhodamine 123 (DHR)

ROS produced by Cu-Cy nanoparticles under UV (360 nm) and different doses of MW (2, 5, and 10 W) in DI water was also measured by fluorescence method using DHR as a ROS tracking agent [99, 100]. A stock solution of 1.16 mM DHR was prepared in dimethylformamide (DMF). The reaction solution with DHR (10 µM) with and without Cu-Cy nanoparticles (311 µM) were prepared in a 10 mm path length cuvette at room temperature in the dark. The sample (final volume

3 mL) was then irradiated by UV light and various powers of MW (2, 5, and 10 W) for different periods. The fluorescence signal was recorded by the spectrofluorophotometer at 524 nm with the excitation at 495 nm, using 3 nm slits.

2.2.9. Detection of hydroxyl radical (•OH) in aqueous solution under MW activation

The •OH generated by Cu-Cy nanoparticles under MW activation was verified using the method described by Zhang *et al.*, 2013 [101] and Kurzyp *et al.*, 2017 [102] with some modifications. The required amount of Cu-Cy aqueous solution was added into a centrifuge tube that contained COU solution (final concentration of COU 0.1 mM). The total volume of the solution in the centrifuge tube was made to be 6 mL. Afterward, the different powers of MW (2, 5, and 10 W) were applied using the microwave therapy apparatus every 5 min into the solution in the presence of Cu-Cy nanoparticles (35 µg/mL). Before each PL measurement, nanoparticles were removed from the sample by centrifugation to confirm that the PL intensity of 7-hydroxycoumarin (7OHC) was not disturbed by the nanoparticles. Then, 3 mL of supernatant was used for each PL spectrum measurement. The PL intensity was monitored at 452 nm with the excitation wavelength of 332 nm. The excitation and emission slit widths were both 5 nm during the measurements. For the control, all the experimental conditions were the same, except the Cu-Cy nanoparticles were not used and were not centrifuged.

2.2.10. CytoViva dark field hyperspectral imaging

100,000 human esophageal squamous cell carcinoma (KYSE-30) cancer cells were cultured on a coverslip in a 35 mm TC petri dish and incubated for 24 h to allow cell attachment. After that, old media was replaced with new media containing 20 µM of Cu-Cy nanoparticles and incubated

for 24 h while wrapped in aluminum foil to prevent unwanted sources of light. Afterward, the old media was removed, and the dish was washed three times using 1 mL of 1x PBS in order to remove unbound nanoparticles. Then, 1 mL of PFA was added into the dish for 30 min to allow the fixing of the cells. PFA was then removed, and the coverslip was carefully placed onto a glass slide supplemented with a drop of DAPI dye, as a wet mount. The edges of the coverslip were finally sealed using white fingernail polish. The product was then analyzed using the CytoViva hyperspectral imaging in combination with enhanced dark field optical microscope (CytoViva Inc., Auburn, AL, USA). The control cell sample was prepared following the same procedure, except the Cu-Cy nanoparticles were not used.

2.2.11. Live/dead cell viability assay

KYSE-30 cancer cells were seeded at a density of 1×10^5 cells/well and allowed to grow for 24 h at 37 °C in a humidified atmosphere of 5 % CO_2 in a cell incubator. There were six groups: control, Cu-Cy, 2 min MW, 3 min MW, Cu-Cy + 2 min MW, and Cu-Cy + 3 min MW. Following the incubation, the cultured media was removed. 2 mL of new media with or without Cu-Cy nanoparticles (5 µg/mL) was added to each well. After 6 h of incubation, the MW and Cu-Cy + MW groups were delivered 2 and 3 min of MW (5 W) through the radiator probe. After that, the cells were placed in the incubator and allowed to incubate for another 20 h. On the day of the experiment, the old media was removed and 500 µL of dye mixture of calcein AM (Invitrogen, USA) and ethidium homodimer-1 (EthD-1) (Invitrogen, USA) was added to each group and incubated for 45 min under standard conditions of cell culture in the dark. Finally, the cells were observed under an OLYMPUS IX71 fluorescence microscope.

2.2.12. Statistical analysis

The data presented as the mean ± standard deviation was performed at least three times independently. The statistical significance between control and experimental groups of the live/dead assay was determined using one-way analysis of variance (ANOVA) followed by the Tukey test. p values less than 0.05 were considered statistically significant.

2.3. Results and discussion

2.3.1. Effects of stirring time, heating temperature, and pH

The Cu-Cy particles can be readily synthesized simply via a wet chemistry process in aqueous solution by reacting $CuCl_2.2H_2O$ and cysteamine hydrochloride. As discussed in the synthesis section, the solution is stirred for approximately 5 min after the pH adjustment. When the color of the mixture becomes the deep violet, it should be heated immediately under the nitrogen atmosphere. It should be noted that if heating is not performed immediately when the mixture takes on its deep violet color, the particles will likely be of lower quality or not be synthesized at all. Therefore, the color of the solution is the main indication for when to begin immediate heating to ensure proper synthesis, rather than a precise stirring time after the pH adjustment. As a primary confirmation of the formation of Cu-Cy particles during the synthesis process, the luminescence of the solution can be checked under a commercial UV light (wavelength about 365 nm). If the luminescence is seen, it confirms the formation of Cu-Cy particles.

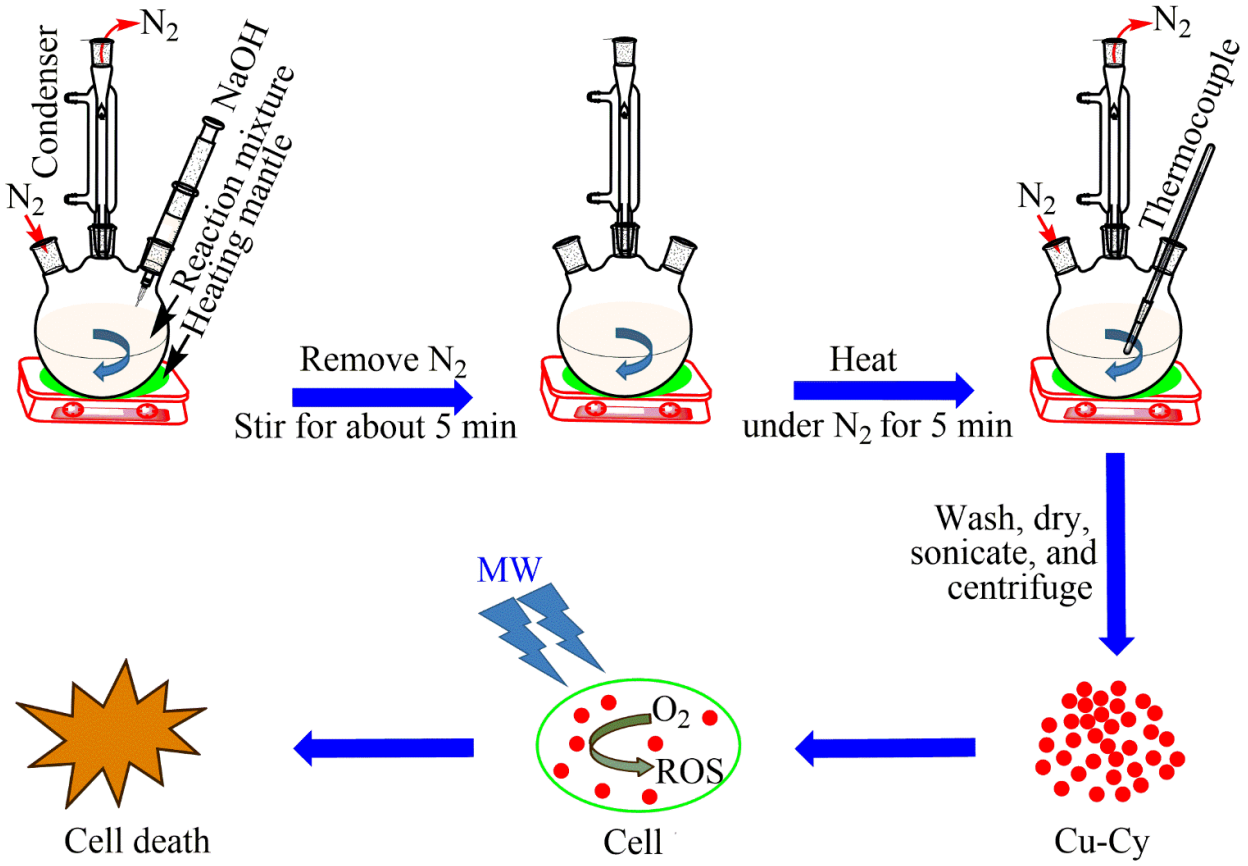

Scheme 2.1. Schematic illustration of the synthesis of the Cu-Cy nanoparticles and the Cu-Cy nanoparticles mediated MW induced radical therapy.

Furthermore, we observed that the Cu-Cy particles can be synthesized at temperatures ranging from about 80 °C to the boiling point of water by varying reaction conditions. Likewise, we noticed that the Cu-Cy particles can be synthesized at different pH values, ranging from around 6.3 to 9 by changing some reaction parameters. We have not yet determined the particle yield, luminescence quantum yield, particle size, surface charge, cell uptake, toxicity, and dispersion stability at different reaction temperatures and pH, which is a part of our ongoing project and will be described in future works.

2.3.2. Characterization of as-synthesized particles

In order to verify that the as-prepared particles were Cu-Cy, different characterization techniques were performed as discussed below. The optical properties of the as-obtained Cu-Cy nanoparticles were investigated using the UV-Vis absorption and fluorescence spectroscopy. Figure 2.1a displays the absorption curve of Cu-Cy nanoparticles dispersed in DI water, with the absorbance maximum at about 365 nm. Figure 2.1b shows the photoluminescence excitation (PLE) and emission (PL) spectra of the Cu-Cy nanoparticles suspended in DI water, which match well with the prior published result [62], confirming that the as-prepared material is Cu-Cy. Two emission peaks at about 607 nm and 633 nm were seen because of the two different types of copper ions, Cu(I) and Cu(II), but they are both Cu^{+} ions, as pointed out by previously reported literature [62]. Figure 2.1c depicts photos of the Cu-Cy nanoparticles in DI water under UV light (left) and room light (right). To further explore the optical luminescence properties of the as-synthesized Cu-Cy particles, X-ray luminescence of the sample was also measured, and the result is shown in Figure S2.1 (ESI†), suggesting that Cu-Cy could be a promising scintillator for radiation detection and dosimetry. Also, the strong photoluminescence and X-ray luminescence in the red region as illustrated in Figures 2.1b-c and Figure S2.1 (ESI†), indicate that it is a potential candidate in various fields, such as cell imaging, lighting, radiation detection, sensing, and dosimetry. It is noteworthy to mention that Cu-Cy has intense X-ray excited luminescence centered at about 633 nm, which is different from that of its photoluminescence peak at about 607 nm. This implies that the X-ray luminescence of Cu-Cy is associated with different coordination of copper ions.

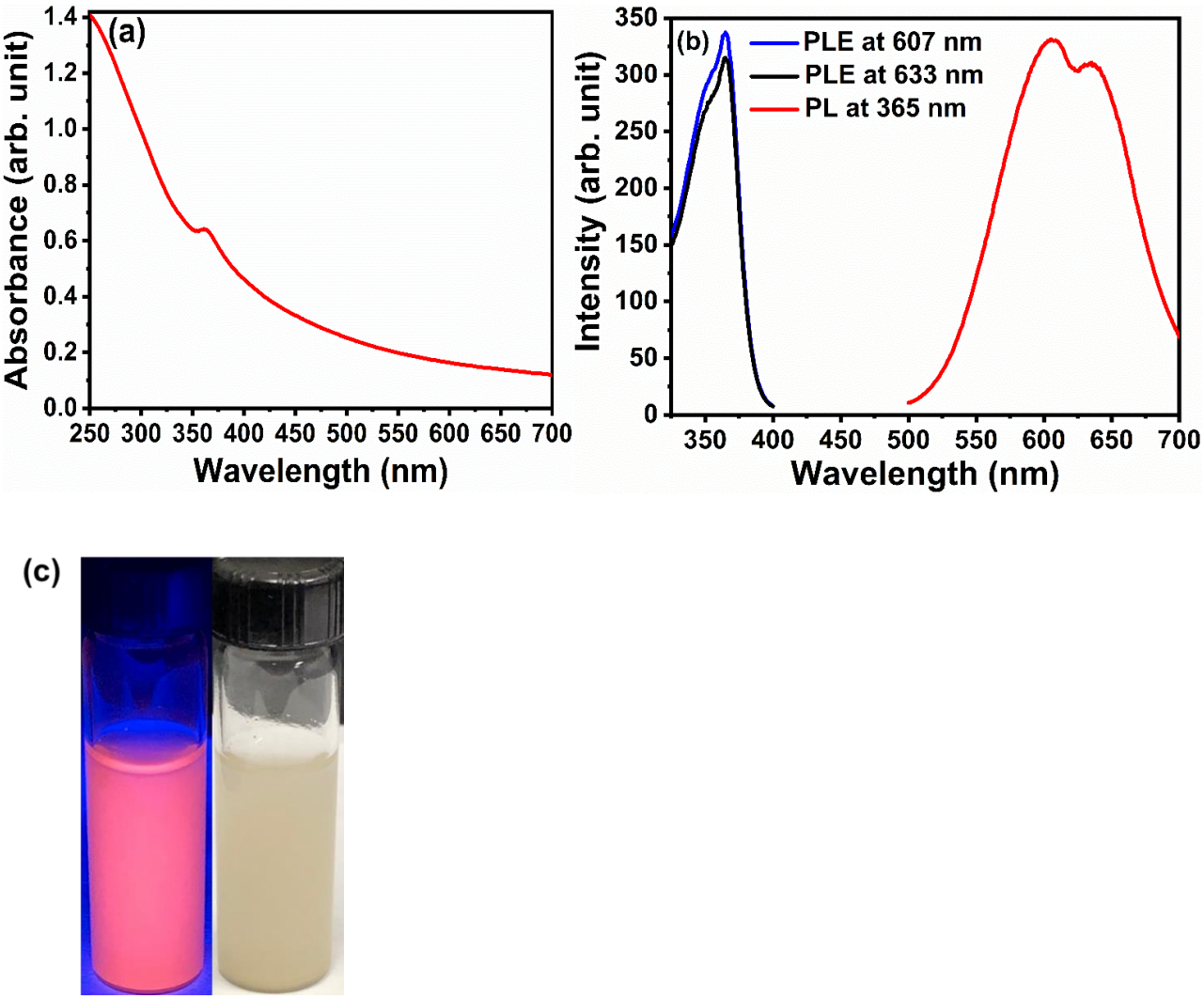

Figure 2.1. (a) UV visible absorption spectrum of the as-prepared Cu-Cy nanoparticles dispersed in DI water. (b) The photoluminescence excitation (PLE, left) at 607 nm (blue curve) and 633 nm (black curve), and emission (PL, right) at 365 nm of the as-obtained Cu-Cy nanoparticles suspended in DI water, and (c) pictures of the newly synthesized Cu-Cy nanoparticles suspended in DI water under room light (right) and UV light (left).

XRD was performed to investigate the crystal structure of the particles. Figure 2.2 shows the XRD pattern of the newly synthesized Cu-Cy particles, which is consistent with that reported in the literature [62], proving that the material synthesized by this method is Cu-Cy. Also, no additional peaks of impurities were seen, which means that the particles are pure.

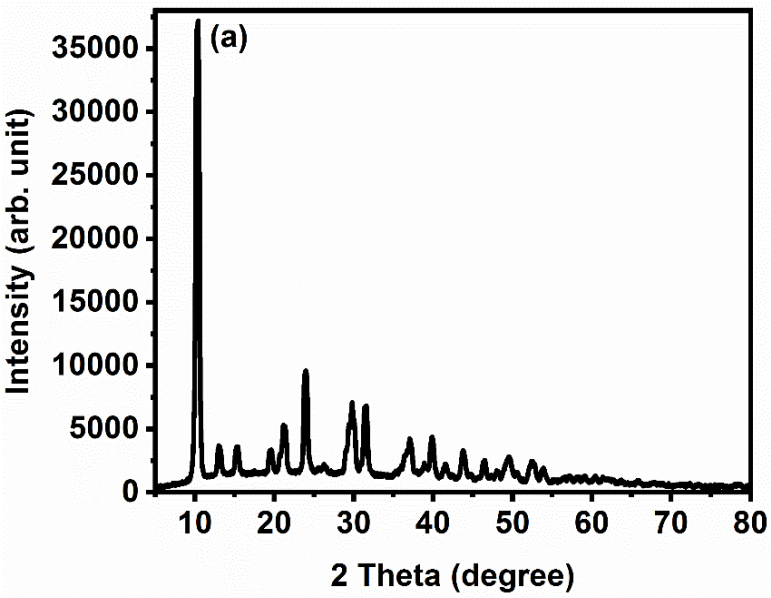

Figure 2.2. XRD pattern of the as-prepared Cu-Cy particles.

Figures 2.3a and b exhibit the representative TEM images of the Cu-Cy nanoparticles. The sizes are about 10-100 nm as observed from their TEM images. Figure 2.3c shows a histogram of the particle size distribution of Cu-Cy nanoparticles fitted by the Gaussian curve with the mean diameter 40 ± 14 nm. The HRTEM image of the Cu-Cy nanoparticles shown in Figure 2.3d demonstrates their continuous uniform lattice fringes. The lattice spacing (d) is estimated to be approximately 0.2409 nm from the HRTEM image (Figure 2.3d), which was determined using ImageJ software. The d value calculated from HRTEM matched with the lattice spacing calculated from the XRD line at 37.041^0 (d=0.2425 nm).

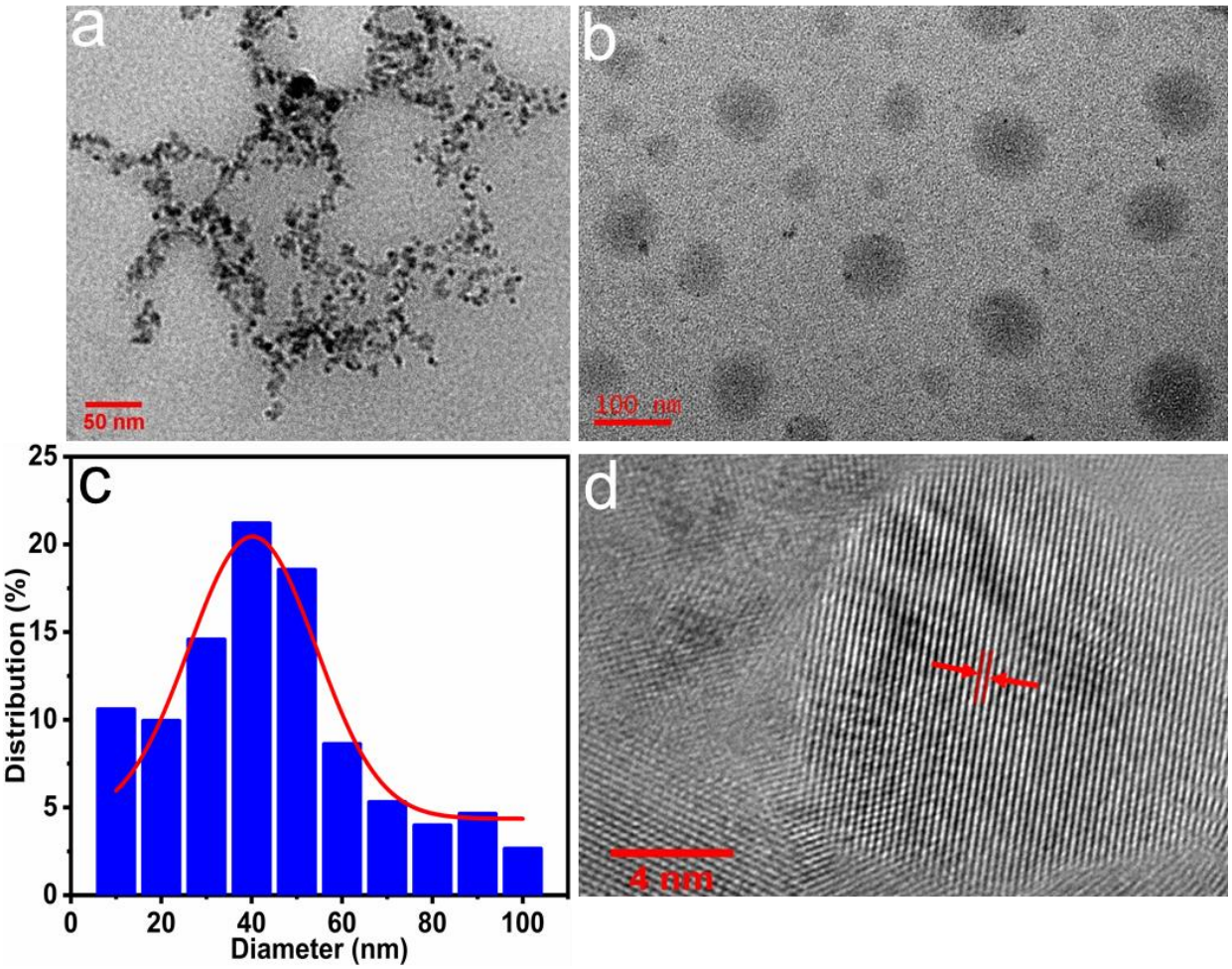

Figure 2.3. (a and b) Representative TEM images of the Cu-Cy nanoparticles. Scale bars, 50 nm and 100 nm, respectively. (c) Histogram of the particle size distribution of Cu-Cy nanoparticles. (d) HRTEM of Cu-Cy nanoparticles. Scale bar, 4 nm.

2.3.3. ROS detection under UV and MW activation using RNO-ID method

To ensure ROS production from the as-prepared Cu-Cy nanoparticles, the RNO-ID method was employed using UV light (360 nm) and different MW powers (2, 5, and 10 W) for various time durations. In this spectrophotometric method, $^1O_2$ produced by a photosensitizer react with imidazole (ID), producing transannular peroxide (IDO_2), which then react with RNO, causing RNO absorption to decrease at 440 nm (–RNO) [98], as depicted below:

$$ID + {}^1O_2 \rightarrow IDO_2,$$

$$IDO_2 + RNO \rightarrow -RNO + products$$

Firstly, to determine ROS production under UV light, RNO's absorption was monitored at 440 nm by the UV-Vis spectrophotometer as a function of illumination time. After using Cu-Cy nanoparticles (311 μM), the RNO absorbance was seen decreasing as shown in Figure 2.4a, indicating $^1O_2$ production by Cu-Cy nanoparticles under UV light. Meanwhile, as a reference, the same measurement was carried out in the absence of Cu-Cy nanoparticles to see if UV light had any effect on RNO absorbance. Little to no decrease in RNO absorbance was observed in the control (DI water) as shown in Figure 2.4a, confirming that UV light alone could not produce ROS. This result proves that newly synthesized Cu-Cy nanoparticles can produce ROS upon photostimulation.

For MW, the same RNO-ID method was used to detect ROS produced by Cu-Cy nanoparticles when irradiated at three different doses of MW at different time periods. As depicted in Figures 2.4b-d, in the control (DI water), the MW irradiation did not produce any ROS. However, after using Cu-Cy nanoparticles (311 μM) (see Figures 2.4b-d), the absorbance of RNO was continuously reduced as a function of MW power and time, providing evidence of a continuous generation of ROS and that more ROS was generated as the MW irradiation power and time increased. Even though the exact path of ROS generation under MW in the presence of materials is not completely understood yet, it is pertinent to mention that similar type of ROS enhancing property has been reported by using other materials under MW activation, such as activated carbon particles [51], gold nanoparticles [103], g-C_3N_4 quantum dots [27], and colloidal TiO_2 nanoparticles [28]. In order to compare the ROS produced by Cu-Cy nanoparticles under three different MW powers, Figure 2.4e was plotted. These results demonstrate that the as-

synthesized Cu-Cy nanoparticles are effective in generating ROS, even under low power MW activation. Surprisingly, the ROS production ability of the newly synthesized Cu-Cy nanoparticles (311 µM) is comparable even under 5 W (4 min) with the published result [34]: Cu-Cy (1.3214 mM) under 20 W MW radiation for 30 min. One possible reason could be the overall particle size reduction. As the size of the nanoparticles can play a vital role in ROS generation, further studies regarding size dependent ROS generation are required to correlate the radical production with the size of the nanoparticles.

In order to determine whether the ROS detected from the RNO-ID method under UV and MW activations were singlet oxygen ($^1O_2$), DABCO, a quencher of $^1O_2$ [104], was employed. As expected, after using DABCO (20 mM), the bleaching of RNO was significantly inhibited (Figures 2.4a-d), which strongly supports that the ROS produced by Cu-Cy nanoparticles were mainly $^1O_2$. This study provided additional evidence for the production of $^1O_2$ during photosensitization and Cu-Cy nanoparticles could be an efficient agent for antimicrobial and anticancer therapies. A charge transfer-induced physical deactivation mechanism is suggested to account for the quenching of $^1O_2$ by DABCO as described in the literature [105]. Moreover, it was confirmed that DABCO alone had no effect on RNO absorbance (Figure S2.2, ESI†).

To ascertain that the RNO-ID method cannot detect the ROS produced by $CuCl_2.2H_2O$ under our experimental conditions, experiments were conducted in the presence of $CuCl_2.2H_2O$ (933 µM). As shown in Figure S2.2 (ESI†), it is evident that $CuCl_2.2H_2O$ could not quench the RNO absorbance under UV and MW exposures under our experimental conditions. These results strongly support the claim that Cu-Cy is an effective material to produce ROS and is a promising candidate in photodynamic therapy (PDT), a type of phototherapy with minimal invasion and less

toxicity [106]. For in-vivo application, the efficacy of Cu-Cy nanoparticles could be further improved by conjugating with oxygen generating agent as discussed in our recent publication [11].

For the purpose of comparison, the ROS production ability of commercially available ZnO nanoparticles (311 µM) was also explored under the same experimental conditions. As can be seen in Figures 2.4a-d, we could not measure much ROS from ZnO nanoparticles under UV and MW activations, indicating that Cu-Cy is superior to commercial ZnO under these excitation sources. This encouraging result further motivated us to compare with commercial TiO_2 nanoparticles (P25). Even though TiO_2 nanoparticles (311 µM) produced ROS to a much greater extent than Cu-Cy nanoparticles (311 µM) under UV light as depicted in Figure 2.4a, TiO_2 nanoparticles could not produce much ROS under MW activation (see Figures 2.4b-d), further supporting that Cu-Cy is a promising sensitizer for MW induced radical therapy. All these findings suggest that Cu-Cy nanoparticles could be an effective material for treating cancers and bacteria or viruses or/and related diseases. It has been reported that ROS production and antimicrobial activities of gold and silver nanoparticles could be enhanced by reducing their size to a value comparable to the Fermi wavelength of electrons (~1 nm) [107-110]. In a similar way, it is reasonable to expect that the anticancer and antimicrobial effects of Cu-Cy nanoparticles may further be increased by reducing the size of the Cu-Cy nanoparticles to the nanocluster range.

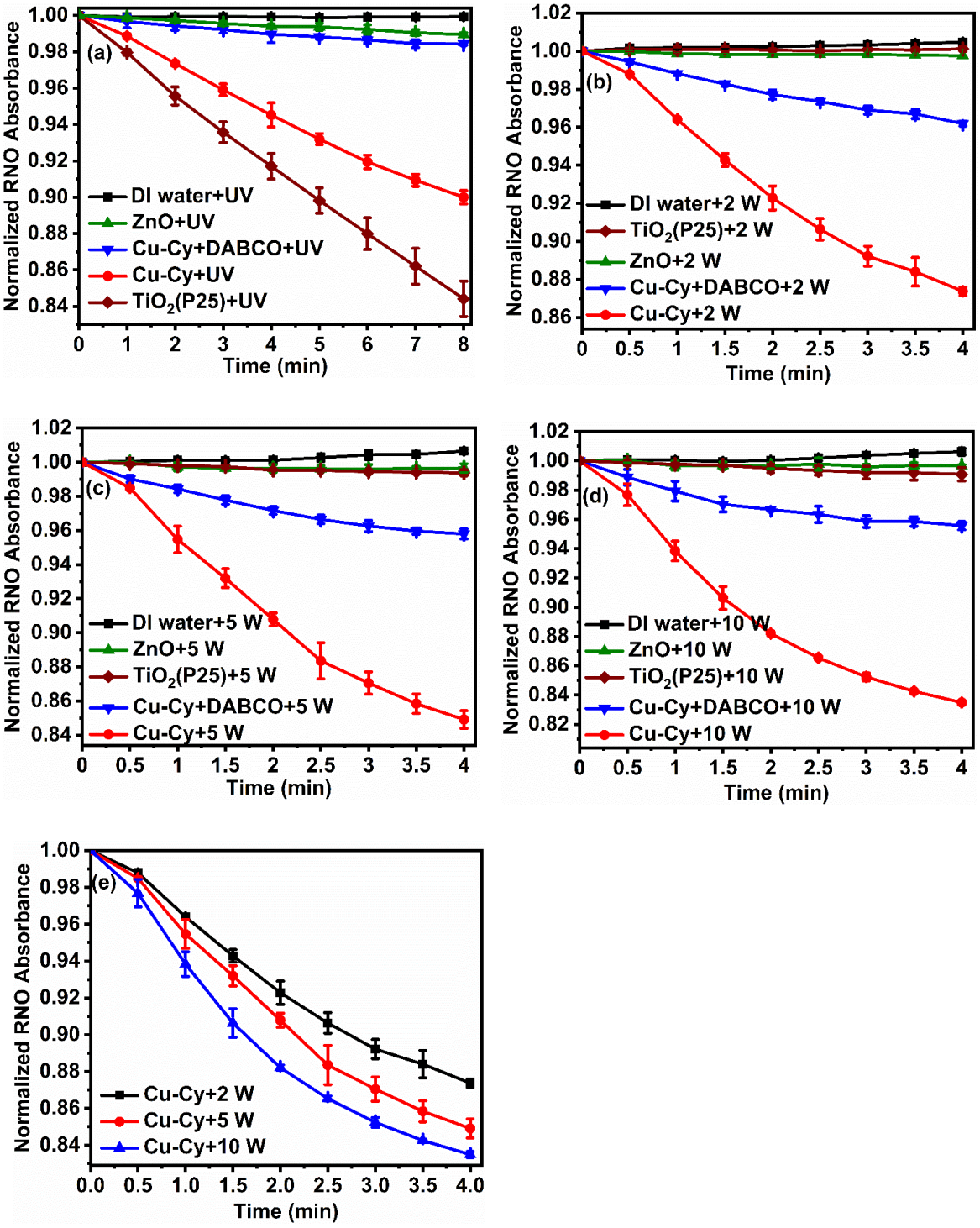

Figure 2.4. Normalized RNO absorbance curves of DI water (control), ZnO (30±10 nm), TiO_2 (P25), Cu-Cy + DABCO, and Cu-Cy aqueous solutions at 440 nm under (a) UV light irradiation in the interval of 1 min, (b) 2 W of MW irradiation in the interval of 30 seconds, (c) 5 W of MW irradiation in the interval of 30 seconds, and (d) 10 W of MW irradiation in the interval of 30 seconds. (e) Comparison of decrease in RNO absorbance in the presence of Cu-Cy nanoparticles at 2, 5, and 10 W of MW exposures.

2.3.4. Study of ROS generation using dihydrorhodamine 123 (DHR)

The detection of ROS was also investigated in a cell-free system using a nonfluorescent probe DHR, which upon oxidation, yields rhodamine 123, a fluorescent molecule [99, 100]. As depicted in Figure 2.5, the relative PL intensity at 524 nm increased to a greater extent after using Cu-Cy nanoparticle (311 µM) under UV and different powers of MW as compared to the blank sample (without Cu-Cy nanoparticles), reflecting the ROS production. The results presented in Figure 2.5b also reveal that more ROS were generated while increasing the MW dose. Although these results were achieved in aqueous solutions, these results further help to explore the ROS production ability of Cu-Cy nanoparticles and support the claim that Cu-Cy is a suitable material for ROS based therapy. It is pertinent to mention that there is also a slight increase in the relative PL intensity at 524 nm without using Cu-Cy nanoparticles, indicating that UV and MW alone cause some oxidation of DHR even in the absence of Cu-Cy nanoparticles.

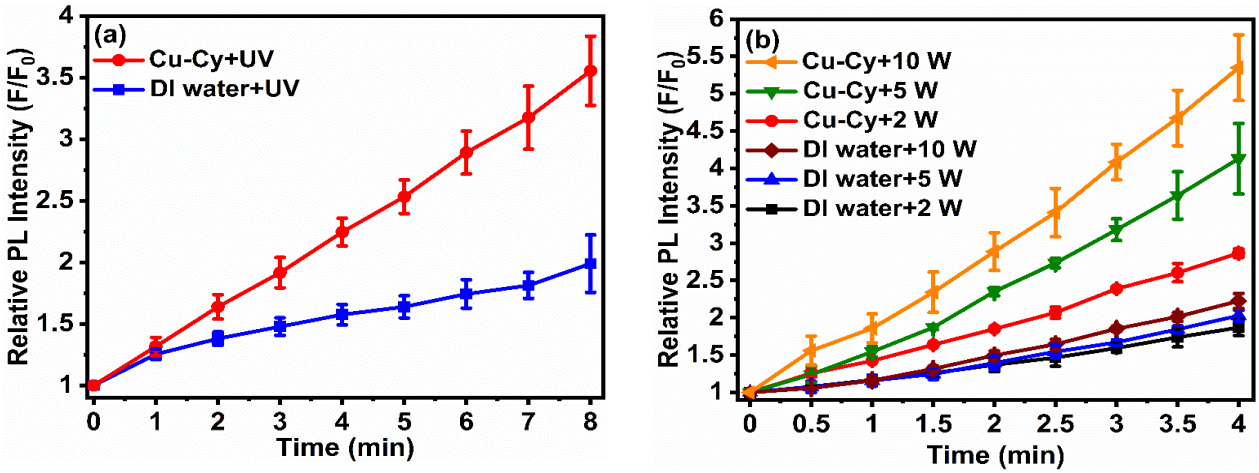

Figure 2.5. The relative fluorescence intensity as a function of irradiation time under (a) UV radiation up to 8 min in the interval of 1 min and (b) MW irradiation (2, 5, and 10 W) up to 4 min in the interval of 30 seconds. F_0 and F are the PL intensities measured at 0 min and after t minutes of UV and MW irradiations at 524 nm, respectively.

2.3.5. Detection of hydroxyl radical under MW activation

It is well known that MW produces different types of ROS. The production of $^1O_2$ under MW exposure was verified by the above experiments (see section 2.3.3). We were then particularly interested in detecting $^{\bullet}OH$ as it is one of the most reactive oxygen radicals and combines very rapidly with almost all types of molecules found in living cells [111]. However, due to its high reactivity and relatively short lifetime under cellular conditions (usually 10^{-9} second in a cell), the direct detection of this radical is difficult [112]. Therefore, in the present work, for the first time, we confirmed the creation of $^{\bullet}OH$ from the Cu-Cy nanoparticles under MW activation by using COU as a probe molecule. It has been reported that COU is a poorly fluorescent molecule that forms the highly fluorescent 7OHC by reacting with $^{\bullet}OH$ as illustrated in Scheme 2.2 [112].

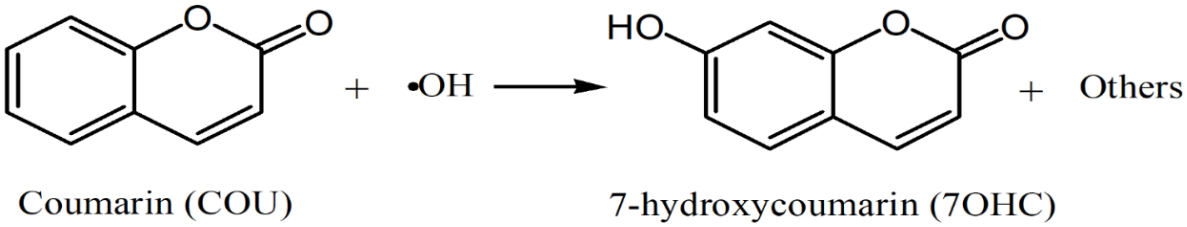

Scheme 2.2. Formation of 7-hydroxycoumarin (7OHC) as a result of the reaction of coumarin (COU) with hydroxyl radical (•OH).

As presented in Figures 2.6a-c, in the presence of Cu-Cy nanoparticles, the PL intensity at about 452 nm increased with the MW exposure in both time and dose-dependent manner, justifying the production of $^{\bullet}OH$. For comparison purpose, Figure 2.6d was plotted, which depicts $^{\bullet}OH$ produced by the Cu-Cy varies with MW dose and exposure time. The PL intensity, however, had almost no change in the absence of Cu-Cy nanoparticles (see Figures 2.6a-c), suggesting that MW

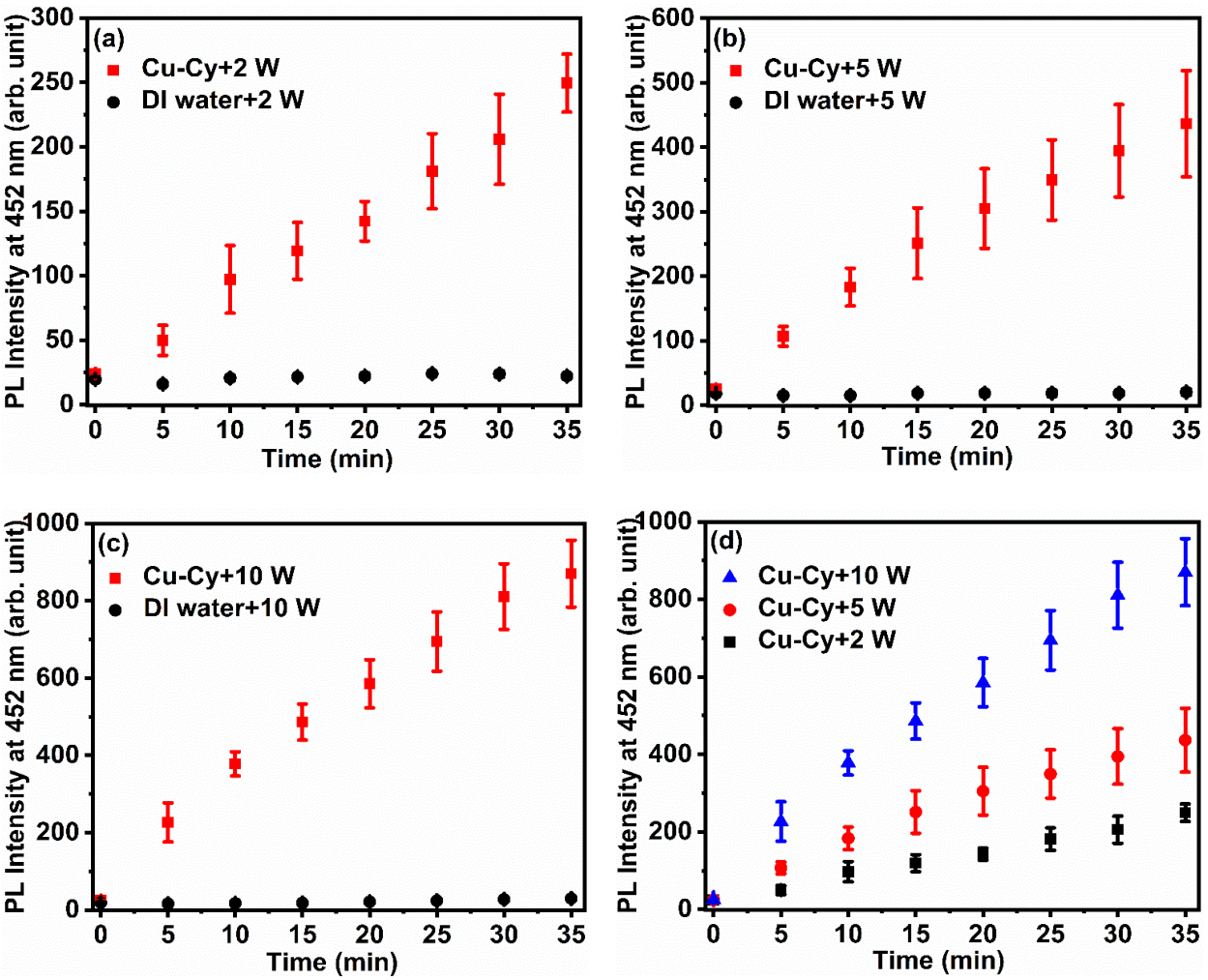

Figure 2.6. The PL spectra of generated 7OHC at 452 nm as a function of irradiation time after exposing MW with (a) 2 W, (b) 5 W, and (c) 10 W for 0-35 min. Each PL spectrum was measured every 5 min of MW irradiation followed by centrifugation. The increase of the PL intensity at 452 nm reveals the formation of •OH. (d) Relation of the PL intensity at 452 nm with MW exposure time at each power.

alone cannot produce any noticeable amount of ˙OH under our experimental conditions. The confirmation of the generation of ˙OH under MW exposure further support to prove that Cu-Cy nanoparticles can be stimulated by MW and can be a powerful weapon to destroy cancer cells by ROS-based therapy (radical therapy). One possible cause of the production of ˙OH by Cu-Cy nanoparticles under MW irradiation in the aqueous solution might be due to catalytic effect of Cu-

Cy nanoparticles, similar to that of other materials, such as activated carbon particles [51] and gold nanoparticles [103] observed under MW energy. Alternatively, the generation of $^{\bullet}OH$ under MW activation in the presence of Cu-Cy nanoparticles could be attributed to chemical enhancement similar to what has been reported by Guo *et al.* [113, 114]. Of course, to identify other types of ROS and to get quantitative results, further experiments are needed. Our future work will also focus on quantification and detection of all the possible types of ROS.

2.3.6. ROS generation and MW heating

Our above experiments prove that Cu-Cy nanoparticles can produce ROS under MW activation, but the exact mechanism of ROS generation induced by MW irradiation largely remains unknown. We believe the most likely mechanism of ROS production of Cu-Cy under MW irradiation in aqueous solution could be similar to that of other particles, such as g-C_3N_4 quantum dots [27] and colloidal TiO_2 nanoparticles [28]. It is well-known that MW radiation is a non-ionizing low energy electromagnetic radiation and does not have enough energy to break the water molecules into radicals or to cause chemical changes. Nevertheless, MW radiation causes polar molecules to continuously realign with the oscillating electric field, thereby increasing their kinetic energy and hence the temperature [41]. Also, MW may mediate for ROS generation. Bruskov *et al.* reported that heat could generate ROS and 8-oxoguanine [115]. They have discussed that heat activates dissolved oxygen and leads to the ROS formation.

In order to understand the heating effect of MW and the ROS production mechanism of Cu-Cy nanoparticles upon MW exposure, temperatures of MW heating with and without Cu-Cy nanoparticles were measured under various MW powers (2, 5, and 10 W). As can be seen in Figure 2.7, the addition of Cu-Cy nanoparticles (311 μM) did not increase the temperatures of the solutions as much as DI water alone, implying that hyperthermia by heating is not a major effect

for tumor destruction and ruling out the possibility that the Cu-Cy nanoparticles may enhance the temperature of MW heating. As depicted in Figure 2.7, the temperatures in Cu-Cy solutions were slightly lower in comparison with the temperatures in DI water. Hence, based on these observations, it is reasonable to claim that for the Cu-Cy solution, the MW was used not only for heating but also for ROS production, whereas for the DI water, the MW was used only for heating. These findings suggest that the dissipated heat could be a potential source of the continued generation of ROS upon MW activation.

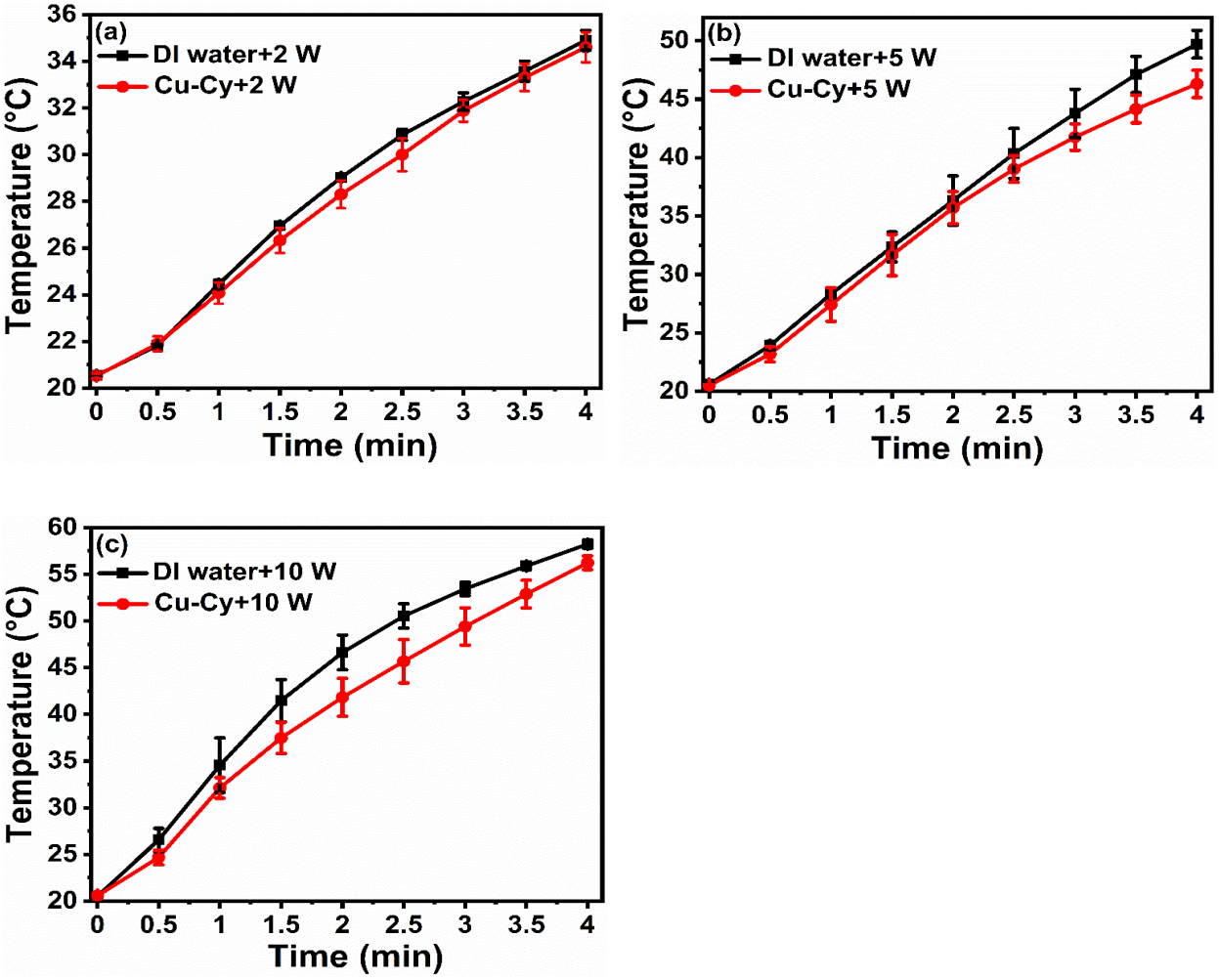

Figure 2.7. Temperature measurements for Cu-Cy (311 µM) solutions and DI water during MW irradiation every 30 seconds intervals up to 4 min under (a) 2 W, (b) 5 W, and (c) 10 W.

2.3.7. Hyperspectral imaging of Cu-Cy nanoparticles internalized in KYSE-30 cancer cells

We used a fast and label-free imaging method, the CytoViva's enhanced darkfield hyperspectral imaging (HSI) technology, to examine the uptake of the Cu-Cy nanoparticles in KYSE-30 cancer cells. This technology is a novel technique that can be used for optical observation and spectral confirmation of a wide range of samples, from nanoparticles to macro in scale. This system uses an oblique angle illumination, which results in high signal-to-noise ratio dark-field images [116, 117]. This technique is used to obtain the complete reflectance spectra corresponding to each pixel's spatial area within the visible near-infrared (VNIR) or the short-wave infrared (SWIR) spectral range. With the CytoViva system, samples can be imaged in seconds or a few minutes with no special sample preparation and without extensive post-processing of the sample.

Figures 2.8a and b depict enhanced darkfield hyperspectral images of control cells (KYSE-30 cancer cells) at 60x magnification and 4x digital zoom, respectively, indicated by the red box. Figure 2.8c illustrates a mean (average) spectral profile per a region of interest (ROI) taken from the cell structure in the zoom area. Figure 2.8d is a hyperspectral image of KYSE-30 cancer cells that have been incubated with Cu-Cy nanoparticles. The magnified window (Figure 2.8e) is from the section ringed in red in Figure 2.8d. Although the uptake of Cu-Cy nanoparticles by the cells is optically apparent, spectral analysis is needed to verify it. In order to justify that the visible nanomaterials were Cu-Cy and not cellular debris or other sample elements, a spectral library was created using the Hyperspectral Image Analysis Software, which consisted of spectra encompassing all of the visible nanomaterials. This spectral library was then filtered against the control sample to eliminate any false positive data. The spectral library shown in Figure 2.8f

illustrates the filtered spectra unique to this sample and not present in the control, indicating the presence of the Cu-Cy nanoparticles within the cells. Each different color in the filtered spectra represents a different point (pixel) of the Cu-Cy nanoparticles in the cells. The filtered spectral library was then mapped against the exposed sample and all pixels matching were pseudo colored yellow, which is presented in Figure 2.8g. Figure 2.8h represents 4x magnification of the red box shown in Figure 2.8g. The spectral plot shown in Figure 2.8i is the mean for all mapped pixels. The comparison of the spectral ROI of the exposed sample to the control sample is shown in Figure S2.6 (ESI†). For the comparison purpose, the data has been normalized to unity. As displayed in Figure S2.6 (ESI†), the ROI for the Cu-Cy nanoparticles is significantly different as compared to the control.

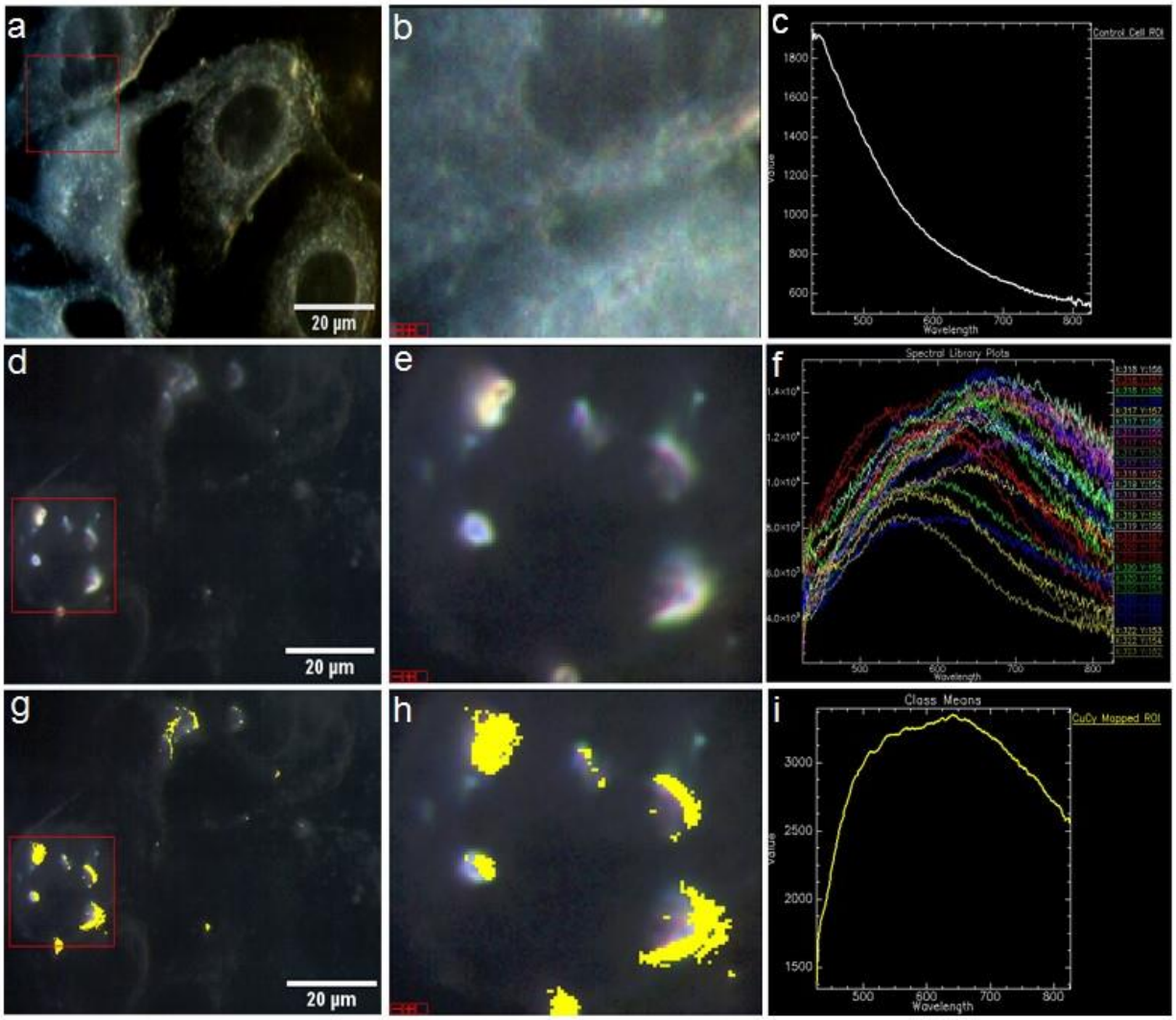

Figure 2.8. CytoViva Hyperspectral Imaging of Cu-Cy nanoparticles localized within the cells. (a) Enhanced dark-field hyperspectral image of the control (cells only) at 60x magnification. (b) Magnified image zoomed 4x. (c) Mean reflectance spectrum taken from the control in the zoom area. (d) A dark-field image of Cu-Cy nanoparticles in the cells. (e) 4x digital zoom of the section ringed in red in Figure 2.8d. (f) Filtered spectral library against the control sample. (g) Mapped image based on the filtered spectral library shown in Figure 2.8f. (h) Magnification of the red box shown in Figure 2.8g, and (i) mean reflectance spectrum profile for all mapped pixels.

2.3.8. Study of in vitro cell destruction using the live/dead assay

In order to further justify that the as-synthesized Cu-Cy nanoparticles are effective for killing cancer cells, even under low concentration of Cu-Cy and low MW power in a relatively

short time, KYSE-30 cancer cells were stained with calcein AM for live cells (green) and ethidium homodimer-1 for dead cells (red). The representative images of three independent experiments are presented in Figure 2.9. The result showed that Cu-Cy nanoparticles alone and 2 min of MW (5 W) alone caused the killing of a few of the cancer cells, while 3 min of MW (5 W) had some degree of toxicity. On the contrary, when Cu-Cy nanoparticles (5 μg/mL) were stimulated by 2 min or 3 min of MW (5 W), the toxicity on the cells was significantly increased as compared to its corresponding controls. The results presented in Figure 2.9 reveal that with the increasing of the MW irradiation time (from 2 min to 3 min), more cells were destroyed. For quantification, the green cells (viable) and red cells (nonviable) were counted using ImageJ software from three independent experiments taking four images from each experiment and the results are shown in Figure 2.10. Comparing this result to our previously reported result [34], we can conclude that the nanoparticles synthesized this way are more effective, even under low MW powers and less MW exposure time, which could be attributed to enhanced reactivity of the as-synthesized nanoparticles. Additionally, in order to explore whether apoptosis is one of the causes of cell death upon MW exposure, Hoechst 33342 staining was adopted and result of this study is presented in Figure S2.7 (ESI†).

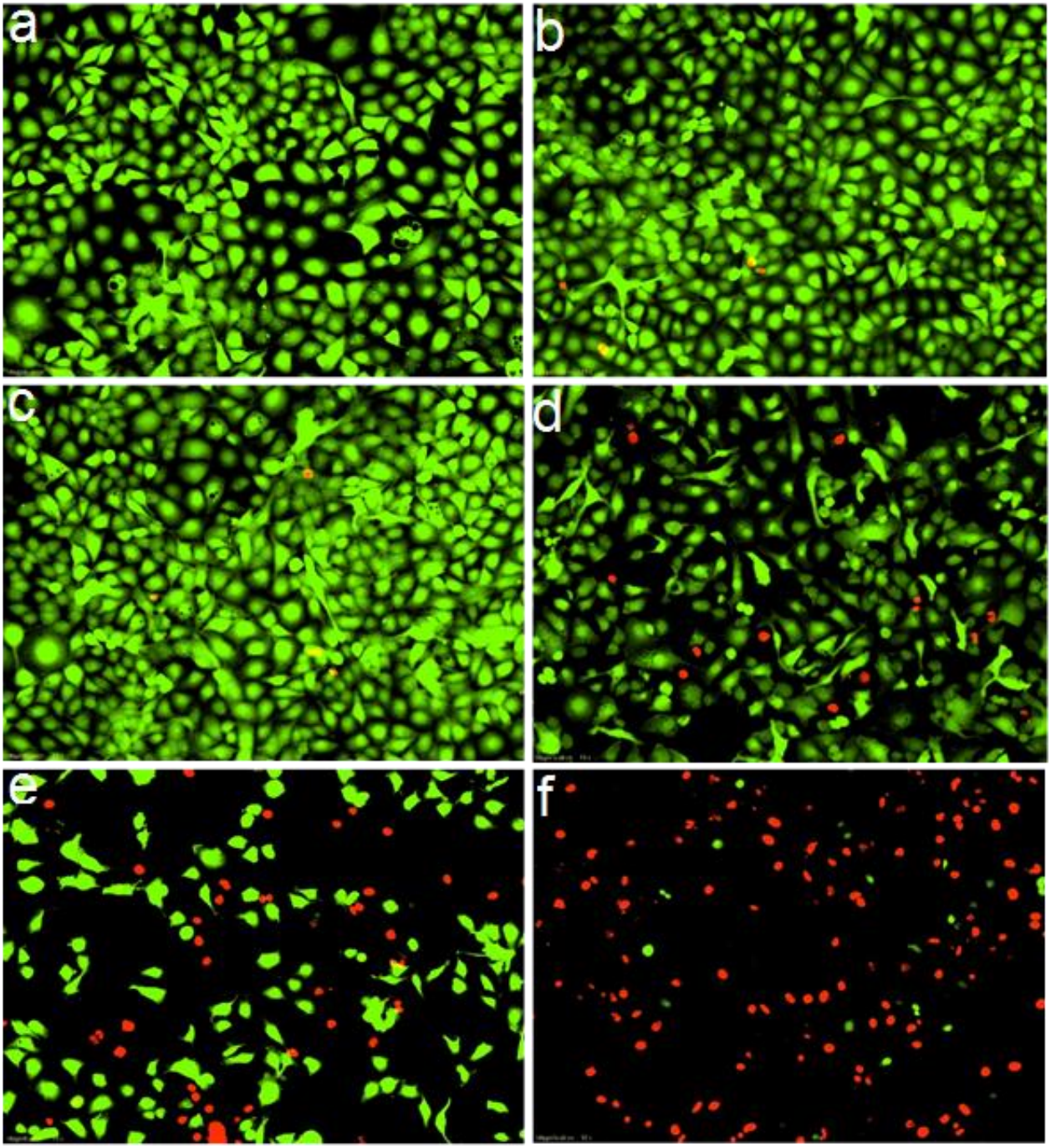

Figure 2.9. The Effect of Cu-Cy nanoparticles under MW irradiation in KYSE-30 cancer cells. (a) Cells without any treatment. (b) Cells treated with Cu-Cy nanoparticles (5 µg/mL). (c) Cells treated with MW (5 W) for 2 min. (d) Cells treated with MW (5 W) for 3 min. (e) Cells treated with Cu-Cy nanoparticles (5 µg/mL) under MW (5 W) for 2 min, and (f) cells treated with Cu-Cy nanoparticles (5 µg/mL) under MW (5 W) for 3 min. Green fluorescence shows the live cells, while red fluorescence shows the dead cells. Magnification: 10x

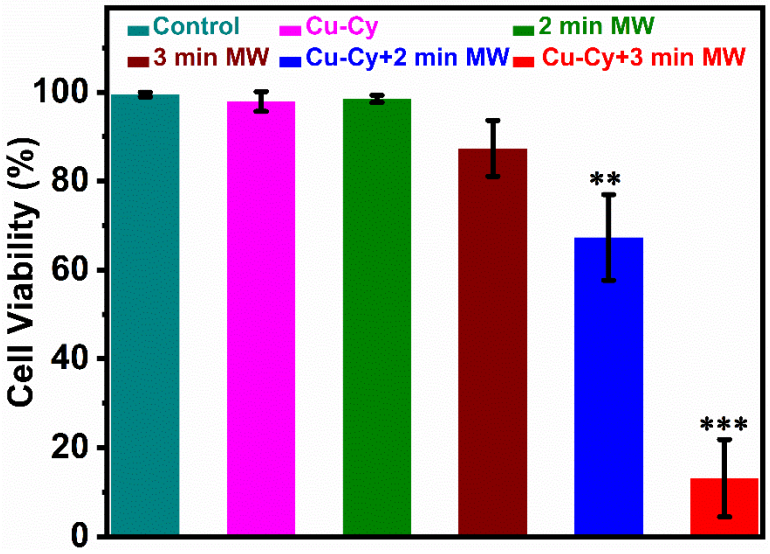

Figure 2.10. The quantitative analysis of the live/dead assay. **p < 0.01 compared with Cu-Cy nanoparticles (5 µg/mL) and 2 min MW (5 W) groups; ***p < 0.01 compared with Cu-Cy nanoparticles (5 µg/mL) and 3 min MW (5 W) groups.

2.4. Conclusions

In this work, we have presented a fast and straightforward method to synthesize Cu-Cy nanoparticles. This synthetic strategy is easy and more economical as compared to the previously reported method. We used different characterization techniques to affirm that the as-synthesized material is Cu-Cy. Using the RNO-ID method, we proved that newly synthesized Cu-Cy nanoparticles can produce ROS under UV and low-dose MW excitations. Inhibition of RNO quenching by DABCO provided additional evidence of the generation of $^1O_2$ in the reaction system. For the first time, the use of DHR as a ROS probe further demonstrated that Cu-Cy nanoparticles can be stimulated by UV and low dose of MW. Additionally, the production of $^{\bullet}OH$ in the presence of the Cu-Cy nanoparticles upon the activation of MW was confirmed by the fluorescent diagnosis method using COU as a trapping agent. Moreover, the underlying internal mechanism for the generation of ROS under MW might be attributed to the dissipated heat. Our

findings also demonstrate that the newly synthesized Cu-Cy is more effective for producing ROS and killing cancer cells, even at the lower concentration of Cu-Cy and lower powers of MW in a relatively lesser time than previously reported Cu-Cy. Indeed, more investigation is still required as Cu-Cy is a new material, some are in progress, for a better understanding of its different properties along with possible novel applications and anticipated that the nanoparticles could be a promising candidate for cancer treatment, antibacterial application, bio-imaging, sensing, radiation detection, dosimetry, and lighting.

Conflicts of interest

There are no conflicts to declare.

Acknowledgments

We would like to acknowledge the support from the U.S. Army Medical Research Acquisition Activity (USAMRAA) under Contracts of W81XWH-10-1-0279 and W81XWH-10-1-0234 as well as the partial support from NIH/NCI 1R15CA199020-01A1. We are thankful to CytoViva Inc., Auburn, AL, USA, for hyperspectral imaging.

Supporting Information

A Facile Method for the Synthesis of Copper-Cysteamine Nanoparticles and Study of ROS Production for Cancer Treatment

Nil Kanatha Pandey,[a] Lalit Chudal,[a] Jonathan Phan,[a] Liangwu Lin,[b] Omar Johnson,[a] Meiying Xing,[a] J. Ping Liu,[a] , Haibin Li,[a,c] Xuejing Huang,[a] Yang Shu*[d] and Wei Chen*[a]

[a]Department of Physics, University of Texas at Arlington, Arlington, Texas 76019, USA

[b]Laboratory on High-Strength Structural Materials, Central South University, Changsha 410083, P. R. China

[c]School of Materials Science and Engineering, Changsha University of Science and Technology, Changsha 410114, People's Republic of China

[d]Research Center for Analytical Sciences, Department of Chemistry, College of Sciences, Northeastern University, Shenyang 110819, China

*Corresponding authors

Email: weichen@uta.edu; shuyang@mail.neu.edu.cn

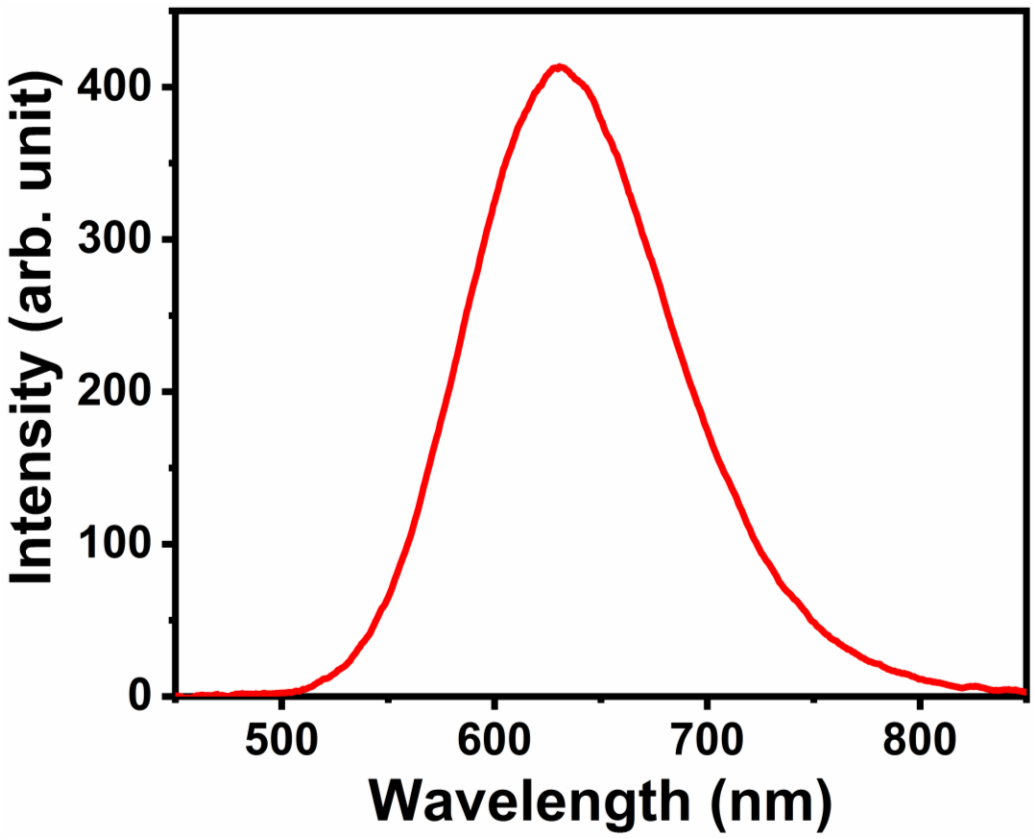

Figure S2.1. X-ray excited luminescence spectrum of the newly synthesized Cu-Cy powders.

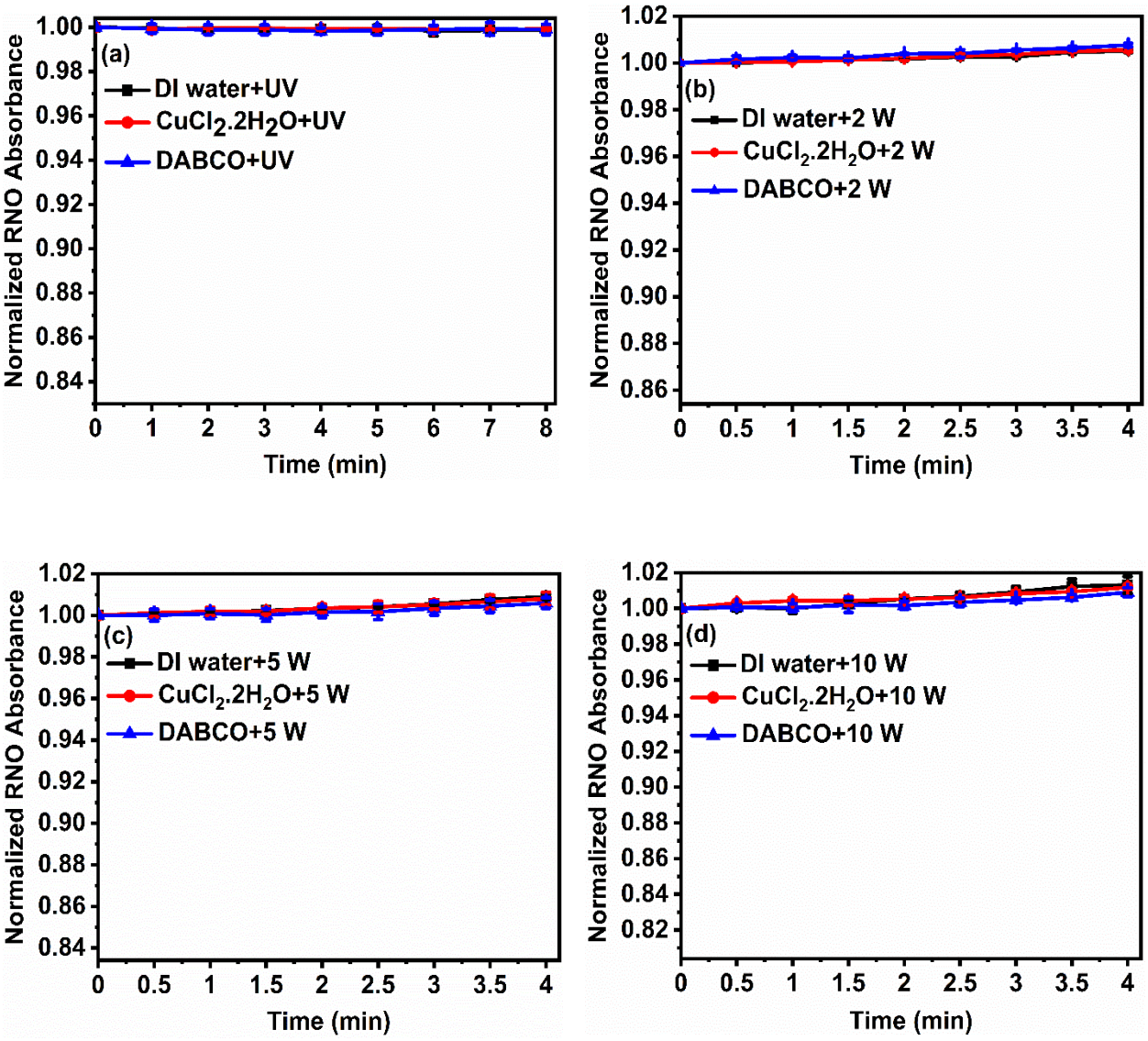

Figure S2.2. Normalized RNO absorbance curves of DI water (control), $CuCl_2.2H_2O$ (933 µM), and DABCO (20 mM) at 440 nm under (a) UV light irradiation for 0-8 min in the interval of 1 min, (b) 2 W of MW irradiation for 0-4 min in the interval of 30 seconds, (c) 5 W of MW irradiation for 0-4 min in the interval of 30 seconds, and (d) 10 W of MW irradiation for 0-4 min in the interval of 30 seconds. These data show that ROS generated by $CuCl_2.2H_2O$ under our experimental conditions cannot be measured by RNO-ID method. Also, the above results display that DABCO alone does not have any effect on RNO absorbance. The data are expressed as the mean ± standard deviation of three independent experiments.

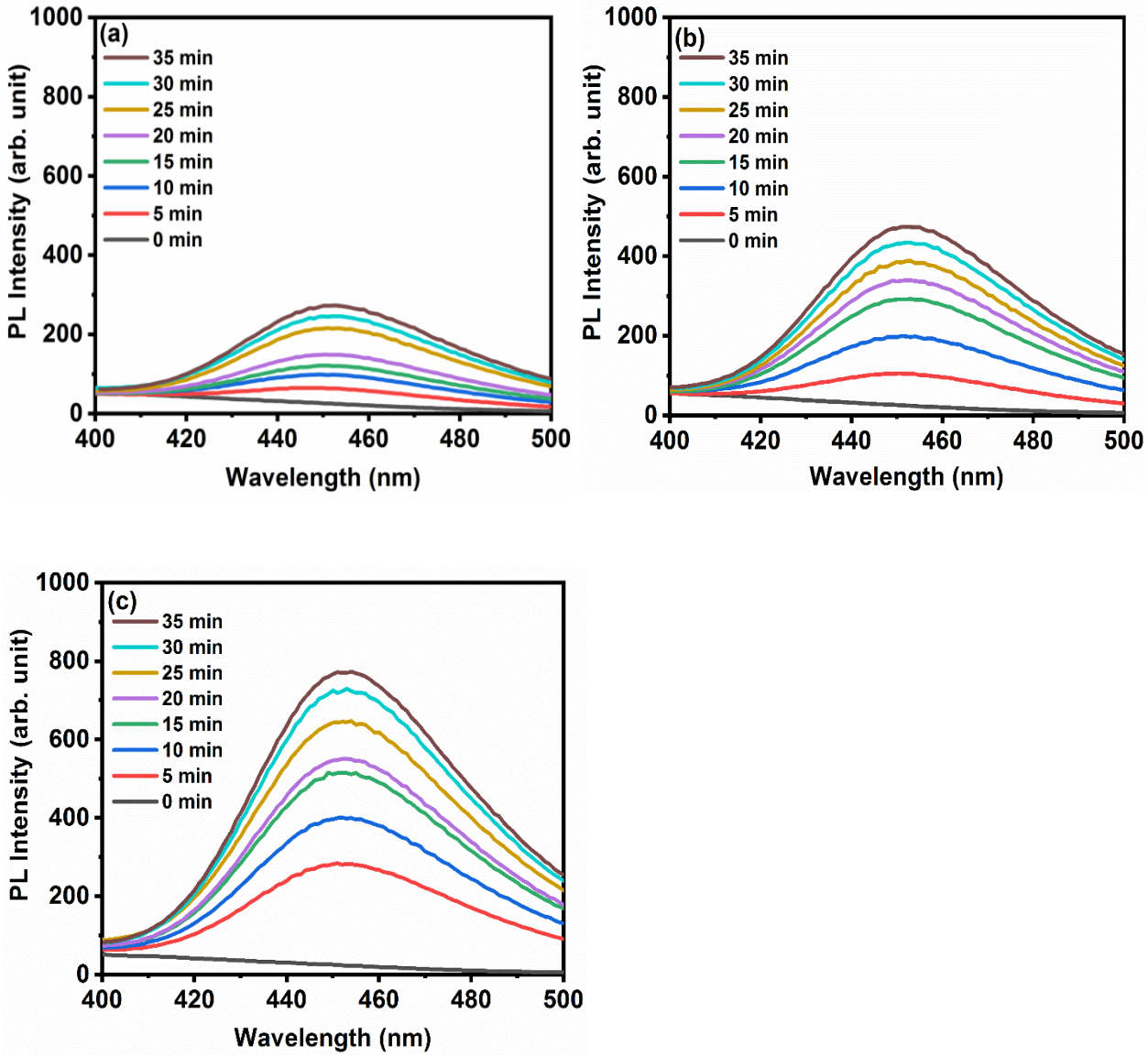

Figure S2.3. Fluorescence spectra of 0.1 mM coumarin solutions of the first trial after exposing MW with (a) 2 W, (b) 5 W, and (c) 10 W for 0-35 min in the presence of Cu-Cy nanoparticles (35 µg/mL). The excitation wavelength was at 332 nm. Increase of the intensity while increasing MW power and time reflects the formation of 7-hydroxycoumarin.

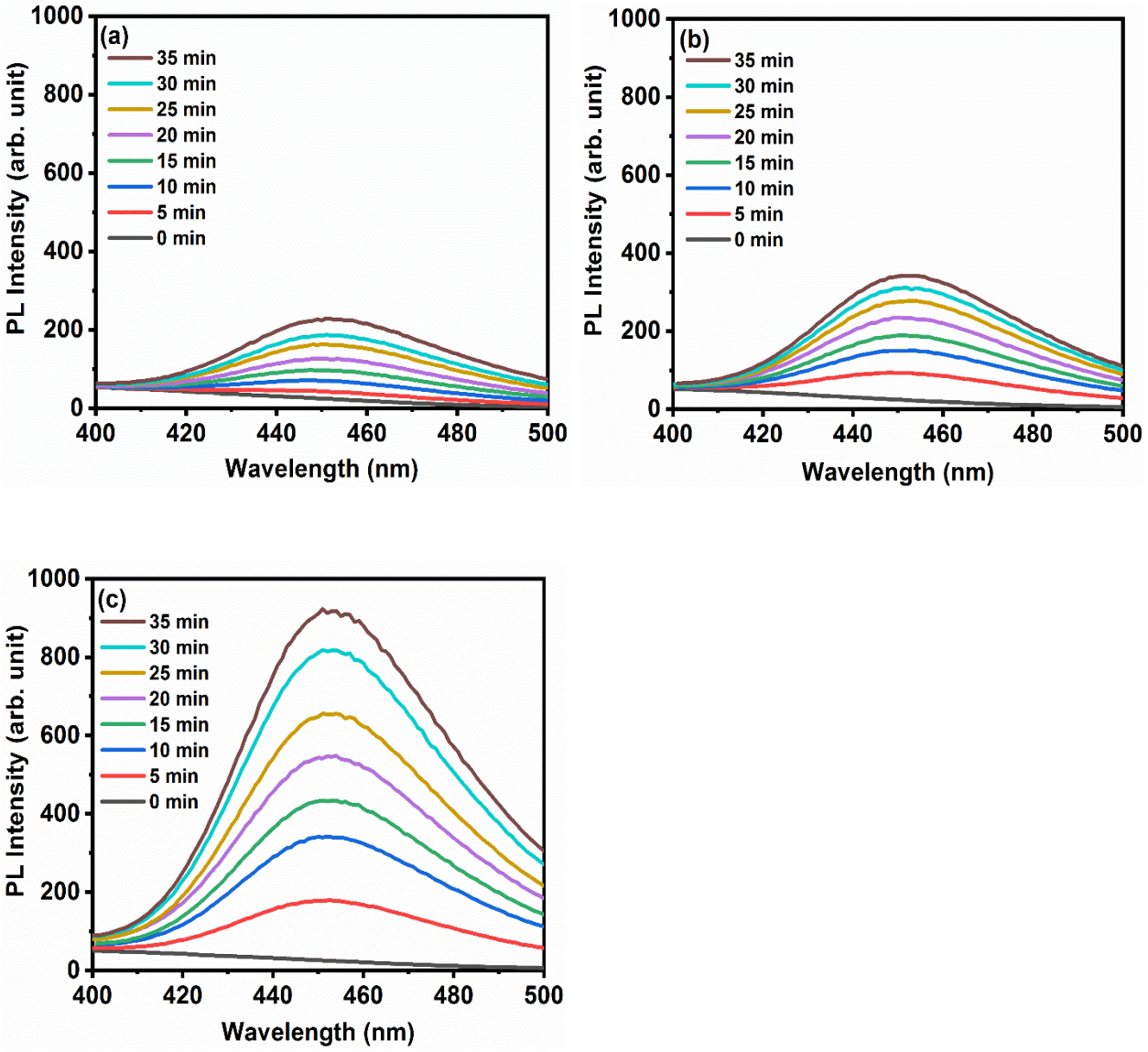

Figure S2.4. Fluorescence spectra of 0.1 mM coumarin solutions of the second trial after exposing MW with (a) 2 W, (b) 5 W, and (c) 10 W for 0-35 min in the presence of Cu-Cy nanoparticles (35 µg/mL). The excitation wavelength was at 332 nm.

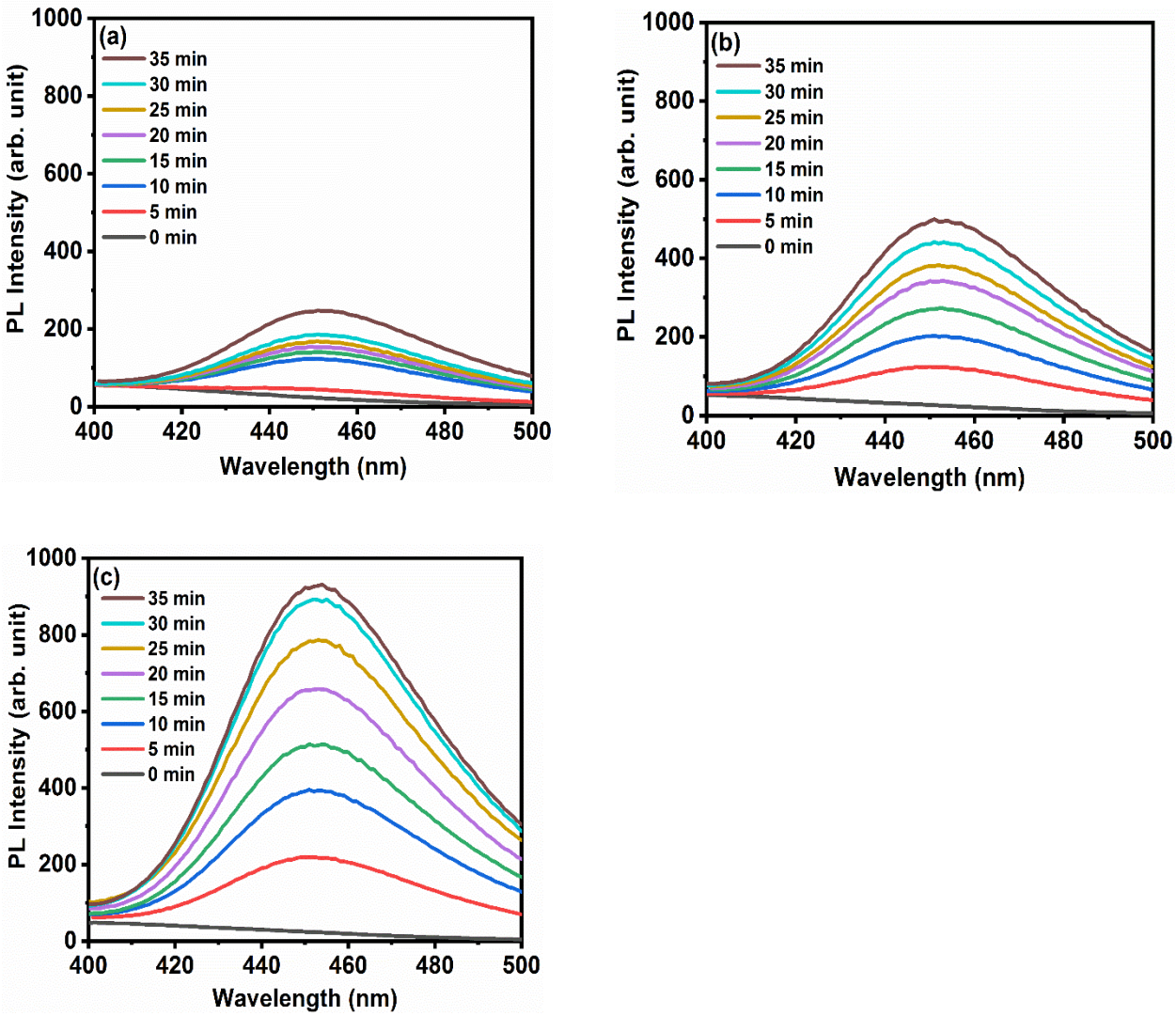

Figure S2.5. Fluorescence spectra of 0.1 mM coumarin solutions of the third trial after exposing MW with (a) 2 W, (b) 5 W, and (c) 10 W for 0-35 min in the presence of Cu-Cy nanoparticles (35 µg/mL). The excitation wavelength was at 332 nm.

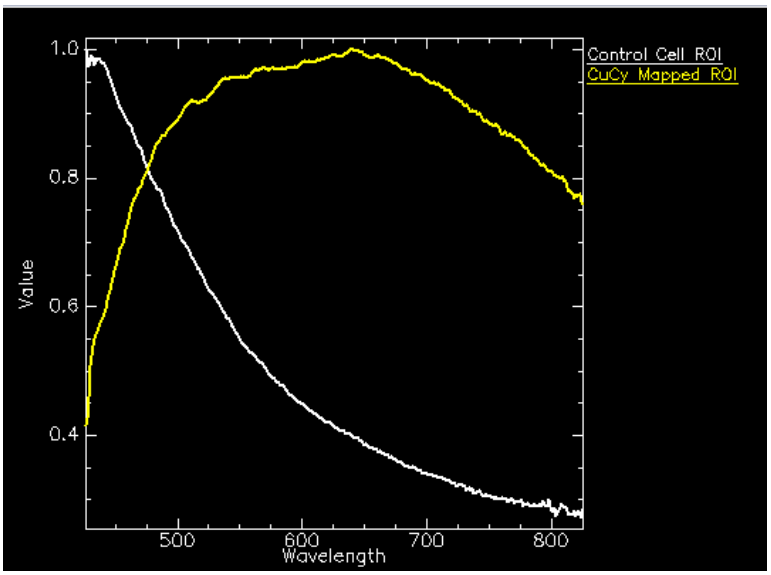

Figure S2.6. Comparison of reflectance spectra of the cells with and without the Cu-Cy nanoparticles.

Cell apoptosis study by Hoechst 33342 staining

Apoptosis and necrosis are two major pathways of cell death [118]. Changes in nuclear morphology, chromatin condensation, and nuclei fragmentation are the main indicators of cellular apoptosis [118-122].

For this study, KYSE-30 cells were seeded into a 6-well plate (1×10^5 cells/well) for 24 h at 37 °C in a humidified atmosphere of 5 % CO_2 in a cell incubator. The cells were divided into four groups: control, MW, Cu-Cy, and Cu-Cy + MW. After 24 h of seeding, the old media was removed. 2 mL fresh media was separately added to the control and MW groups, and 2 mL media containing 7.5 µg Cu-Cy nanoparticles (3.75 µg/mL) was added to the Cu-Cy and Cu-Cy + MW groups. After 6 h, 30 seconds of MW (5 W) was applied to the MW and Cu-Cy + MW groups. The cells were further incubated for 20 h. Following the incubation, the old media was removed, the cells were washed 3 times with PBS and fixed with PFA for 15 min. Then, Hoechst 33342 dye

was added to stain nucleus for 15 min at room temperature. The cells were subsequently observed under an OLYMPUS IX71 fluorescence microscope to study the cellular apoptosis.

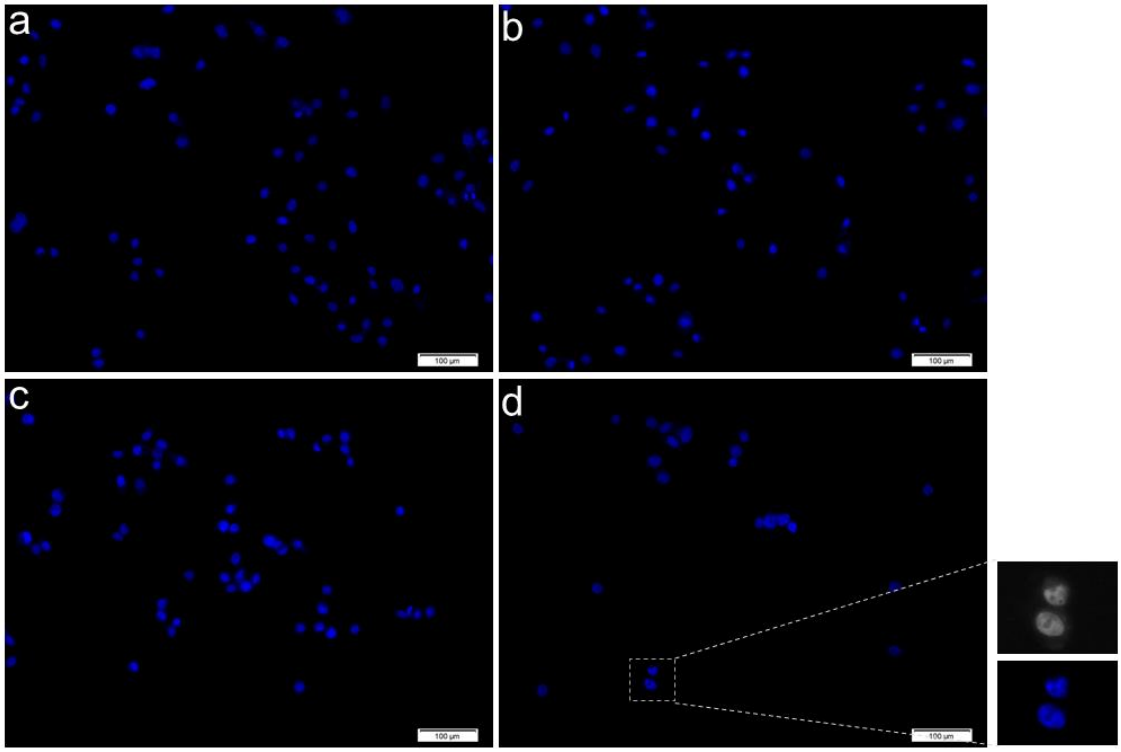

Figure S2.7. The Effect of Cu-Cy nanoparticles with MW treatment on the induction of apoptosis in KYSE-30 cancer cells. (a) Control group, (b) MW (30 seconds, 5 W), (c) Cu-Cy nanoparticles (3.75 µg/mL), and (d) Cu-Cy nanoparticles (3.75 µg/mL) + MW (30 seconds, 5 W). Scale bar: 100 µm.

The result showed in Figure S2.7 shows that MW or Cu-Cy nanoparticles alone could not induce apoptosis. However, when Cu-Cy was stimulated by MW, we could observe the cell shrinkage. Also, the nucleus became smaller and split into smaller apoptotic bodies. It indicates that one of the causes of cell death under MW stimulation is apoptosis.

Chapter 3

(Published in Bioactive Materials)

Aggregation-Induced Emission Luminogens for Highly Effective Microwave Dynamic Therapy

Nil Kanatha Pandey[1], Wei Xiong[2], Lingyun Wang[1, 2*], Wei Chen[1]*, Brian Bui[1], Jian Yang[3], Eric Amador[1], Mingli Chen[4], Christina Xing[1], Aseem Atul Athavale[5], Yaowu Hao,[5] Wirya Feizi[6], and Lloyd Lumata[6]

[1] Department of Physics, The University of Texas at Arlington, Arlington, TX 76019, USA.

[2] Key Laboratory of Functional Molecular Engineering of Guangdong Province, School of Chemistry and Chemical Engineering, South China University of Technology, Guangzhou, China, 510640.

[3] Department of Biomedical Engineering, The Pennsylvania State University, University Park, PA, 16802, USA.

[4] Department of Chemistry, College of Sciences, Northeastern University, Box 332, Shenyang 110819, China.

[5] Department of Materials Science and Engineering, The University of Texas at Arlington, Arlington, TX 76019, USA.

[6] Department of Physics, The University of Texas at Dallas, 800 West Campbell Road, Richardson, TX 75080, USA.

*Corresponding authors:

lingyun@scut.edu.cn; weichen@uta.edu

Reproduced from Ref. Pandey, N. K., Xiong, W., Wang, L., Chen, W., Bui, B., Yang, J., ... & Lumata, L. (2021). Aggregation-induced emission luminogens for highly effective microwave dynamic therapy. Bioactive Materials, https://doi.org/10.1016/j.bioactmat.2021.05.031 (in press), with permission from the KeAi Publishing Ltd. All the authors have permission to use in the dissertation.

Abstract

Aggregation-induced emission luminogens (AIEgens) exhibit efficient cytotoxic reactive oxygen species (ROS) generation capability and unique light-up features in the aggregated state, which have been well explored in image-guided photodynamic therapy (PDT). However, the limited penetration depth of light in tissue severely hinders AIEgens as a candidate for primary or adjunctive therapy for clinical applications. Coincidentally, microwaves (MWs) show a distinct advantage for deeper penetration depth in tissues than light. Herein, for the first time, we report AIEgen-mediated microwave dynamic therapy (MWDT) for cancer treatment. We found that two AIEgens (**TPEPy-I** and **TPEPy-PF6**) served as a new type of microwave (MW) sensitizers to produce ROS, including singlet oxygen ($^1O_2$), resulting in efficient destructions of cancer cells. The results of 3-(4,5-dimethylthiazol-2-yl)-2,5-diphenyltetrazolium bromide (MTT) and live/dead assays reveal that the two AIEgens when activated by MW irradiation can effectively kill cancer cells with average IC-50 values of 2.73 and 3.22 μM, respectively. Overall, the ability of the two AIEgens to be activated by MW not only overcomes the limitations of conventional PDT, but also helps to improve existing MW ablation therapy by reducing the MW dose required to achieve the same therapeutic outcome, thus reducing the occurrence of side-effects of MW radiation.

Keywords: AIEgens; microwaves; photodynamic therapy; reactive oxygen species; microwave ablation; cancer treatment; singlet oxygen

3.1. Introduction

Photodynamic therapy (PDT), a promising cancer treatment modality with minimal invasiveness, negligible drug resistance and low side effects, employs a photosensitizer (PS) that can be excited by light of suitable wavelength to form ROS, which can induce apoptosis and/or

necrosis in treated cells. Also, PDT can be used either on its own or in combination with other therapeutic modalities, such as surgery, chemotherapy, radiotherapy, or immunotherapy [10, 11, 123]. Even though PDT has great potential for clinical use, conventional PSs generally suffer from aggregation-caused fluorescence quenching and a significant reduction in ROS production in aqueous media [45, 124-126]. Fortunately, aggregation-induced emission luminogens (AIEgens) offer a potential opportunity to overcome this limitation. AIEgens refer to special types of molecules that are barely emissive in the molecularly dissolved state but emit intense fluorescence in the aggregation state due to the restriction of intramolecular motion [124]. Intriguingly, several AIEgens show efficient photosensitizing ability and unique light-up features in the aggregated state, which are beneficial to develop image-guided PDT for cancer treatment [45, 46, 125, 126]. However, the poor penetration depth of light still hinders AIE PSs as primary or adjunctive therapy for clinical application. Furthermore, due to the oxygen-dependent nature of PDT [36], it is noted that both types of PSs (conventional and AIE) are less effective in treating hypoxic tumors, further limiting their practicality in clinical settings.

As an alternative modality of tumor destruction, thermal ablation has been extensively explored in the clinical setting. It is considered as one of the most effective treatments in combined oncotherapy as it leads to improved tumor sensitization to PDT, chemotherapy, immunotherapy, or radiotherapy [37, 38, 127-129] because the blood flow to the tumor is enhanced through heating. When the tissues are heated, the blood vessels dilate, which increases blood flow. As hemoglobin in blood contains oxygen, tissue heating boosts the amount of oxygen, thereby enhancing the efficacy of the treatments [37, 38]. Compared with other thermal therapies, MW technology has many advantages, such as maneuverability, faster ablation time, deeper penetration in tissues, larger tumor ablation volumes, less procedural pain, consistently higher intratumoral temperature,

and negligible side effects [38, 39, 41, 130]. Notably, MWs are readily capable of propagating through many types of tissues and nonmetallic materials, including charred or desiccated tissues created during the process of ablation [41]. Despite these advantages, the lack of selectivity of MWs on tumors may cause severe damage to the surrounding normal tissues during the course of treatment [123]. Consequently, further study and continued development of a more robust system are still needed to minimize nonspecific heating of healthy tissues.

Recently, microwave dynamic therapy (MWDT) has attracted broad attention, in which MW sensitizers can produce ROS under MW irradiation to destroy tumor cells. Various MW-responsive agents such as copper-cysteamine (Cu-Cy) nanoparticles [29, 34], g-C_3N_4 quantum dots [27], TiO_2 nanoparticles [28], Fe-metal organic framework nanoparticles [30], liquid metal supernanoparticles [31], Cu_2ZnSnS_4 nanocrystals [32], Mn-doped zirconium metal-organic framework nanocubes [33], and gold nanoparticles [103] have been reported to produce ROS upon MW radiation. All of these sensitizers are sensitive to MWs and attractive for applications with MWs; however, the toxic nature of some of these metal ions and/or high concentration of sensitizers could result in severe side effects. Therefore, the exploration of more efficient sensitizers that are capable of avoiding the above limitations is of great importance to improve the therapeutic effect of MWDT.

In our previous work, pyridinium-substituted tetraphenylethylene salt-based AIEgens (**TPEPy-I** and **TPEPy-PF6**, Scheme 3.1) exhibited PDT effect for cancer cell destruction and bacterial inactivation under white light irradiation [131]. However, to the best of our knowledge, there is no report on AIEgen-mediated ROS production under MW irradiation. The reason may be that MW has an energy of only 10^{-3} eV, which is too low to cleave chemical bonds and induce ROS generation [31, 50]. Considering these two AIEgens comprise of a TPE segment (donor), a

thiophene vinyl fragment (π bridge), and a cationic pyridinium moiety (acceptor) with a strong charge-transfer feature and effective ISC channels with a small ΔE_{S-T} ($S_1 \rightarrow T_3$: -0.22 eV), it is possible for them to be activated by MW irradiation to generate ROS.

In this contribution, for the first time, the two AIEgens (**TPEPy-I** and **TPEPy-PF6**) are reported as MW sensitizers with efficient ROS generation and cancer cell killing capabilities under MW irradiation. Overall, this work opens the door to treat tumors using AIEgens under MW irradiation and makes conventional PDT possible for deep cancer treatment, even in the context of hypoxic environments.

3.2. Experimental section

3.2.1. Materials

p-Nitrosodimethylaniline (RNO), imidazole, 1,4-benzoquinone (BQ), sodium azide (NaN_3), 2′,7′-dichlorodihydrofluorescein diacetate (DCFH-DA), 9,10-anthracenediyl-bis(methylene)dimalonic acid (ABDA), 2,2,6,6-tetramethylpiperidine (TEMP), and 1,4-diazabicyclo[2.2.2]octane (DABCO) were obtained from Sigma-Aldrich, USA. 3-(4,5-dimethylthiazol-2-yl)-2,5-diphenyltetrazolium bromide (MTT) was purchased from Thermo Fisher Scientific, USA. All the chemicals were used as received without further purification.

3.2.2. UV-vis absorption and fluorescence spectroscopy

TPEPy-I and **TPEPy-PF6** (stock solution in DMF) were dispersed in DI water, and the UV-vis optical absorption and photoluminescence spectra were measured by using a Shimadzu UV-Vis spectrophotometer (UV-2450) and a Shimadzu spectrofluorophotometer (RF-5301PC), respectively.

3.2.3. Scanning electron microscopy (SEM) and fluorescence microscopy imaging

The SEM images were taken by using a Hitachi S-4800 FE-SEM. For SEM measurements, samples were dropped on the surface of the silicon substrate and then dried to obtain dried samples. In order to obtain fluorescence microscopy images, **TPEPy-I** or **TPEPy-PF6** was dropped into an imaging plate and then observed using an OLYMPUS IX71 fluorescence microscope.

3.2.4. ROS detection in cell-free system using RNO bleaching method

We employed the RNO bleaching method [98] to probe the extracellular ROS production upon MW excitation. The intensity of RNO absorption was recorded spectrophotometrically at different time points of MW exposure (2450 MHz). The MW was delivered in a dark condition through a radiator probe employing a microwave therapy apparatus (WB-3100AI, BXING, China). Briefly, 0.45 mg of RNO and 32.68 mg of imidazole were dissolved separately into 30 mL of DI water, which were subsequently air saturated by air bubbling for 15 min. Afterward, the RNO-imidazole solution (final volume 3mL) was prepared under the dark condition in a cuvette (10 mm path length) by mixing 1 mL of RNO, 1 mL of imidazole, and 1 mL of the testing sample. Meanwhile, as a reference, the control experiment was carried out following the same procedure, except the testing sample was replaced by DI water to see the effect of MW irradiation on RNO's absorption.

3.2.5. Singlet oxygen ($^1O_2$) detection in aqueous solution using ABDA probe and electron spin resonance (ESR) spectroscopy

In order to further support the $^1O_2$ production under MW activation, $^1O_2$ produced by the **TPEPy-I** and **TPEPy-PF6** nanoaggregates were also measured by employing the commercially

available probe ABDA as a $^1O_2$ indicator [132]. Briefly, the stock solution of ABDA (1.5 mM) was made in DMF. The working solution (final volume 3 mL) was prepared in DI water by taking 30 μM of ABDA and 15 μM of **TPEPy-I** or **TPEPy-PF6** in a 10 mm path length cuvette under dark condition. The solution was then exposed to MW (2450 MHz) in the dark for various periods, and the absorbance of ABDA was monitored at 379 nm by the spectrophotometer. The control experiment was performed by taking DI water alone instead of the testing sample under the same conditions to compare the effect of MW on the absorbance of ABDA.

The ESR measurements were conducted at the Nanotech Institute at the University of Texas at Dallas by using a Bruker EMX X-band ESR spectrometer (Bruker Biospin, Billerica, MA). A small aliquot of each sample was placed in 0.5-mm ID heparinized hematocrit capillary tubes, which were subsequently placed in 4-mm thin wall quartz ESR tubes (Wilmad Lab-Glass, Vineland, NJ). Field-swept continuous wave ESR spectra were recorded at room temperature.

3.2.6. Extracellular ROS detection using DCFH-DA probe

The ROS produced by the **TPEPy-I** and **TPEPy-PF6** nanoaggregates in aqueous solution upon MW excitation was further investigated by the photoluminescence (PL) method using DCFH-DA as a ROS probing agent [31, 46]. The stock solution of DCFH-DA (1.8 mM) was made in DMF. After that, the working solution (final volume 3 mL) containing DCFH-DA (30 μM) and **TPEPy-I** or **TPEPy-PF6** (10 μM) was prepared in a cuvette (10 mm path length) under the dark condition. The solution was then exposed to MW (2450 MHz) in the dark for various periods, and the PL intensity was subsequently recorded at 523 nm by the spectrofluorophotometer with the excitation wavelength of 505 nm. The control experiment was performed by taking DI water instead of **TPEPy-I** and **TPEPy-PF6** under the same conditions.

3.2.7. Detection of intracellular ROS production

We studied the intracellular generation of ROS using DCFH-DA as a fluorescence detection probe [133]. 1×10^5 HeLa cells per imaging plate were seeded into nine different imaging plates and incubated in a humidified cell incubator containing 5% CO_2 at 37 °C for 24 h. Afterward, the cells were incubated with or without **TPEPy-I** and **TPEPy-PF6** (5 μM) for 4 h in the fresh culture medium (3 mL). Cells were then washed with PBS twice and incubated with 20 μM of DCFH-DA in DMEM (500 μL) for another 45 min at 37 °C in the dark. The cells were subsequently washed three times with PBS in order to remove the unloaded probe. The indicated cells were then exposed to 10 W (2450 MHz) of MW irradiation (inserting the MW probe into the medium without touching the cells) in the dark condition for 1 or 1.5 min after adding 3 mL of DMEM. Finally, the cells were resuspended in PBS (500 μL) and immediately observed using the OLYMPUS IX71 fluorescence microscope under the same instrumental conditions.

3.2.8. Microwave dynamic therapy (MWDT) study using MTT assay

The cytotoxicity of **TPEPy-I** and **TPEPy-PF6** nanoaggregates under MW irradiation was investigated using MTT assay. HeLa cells were seeded in 24-well plates at a density of 2×10^4 cells/well. After allowing to attach and grow for 24 h, the old medium was removed from each well, and 2.4 mL of fresh culture medium (DMF-culture medium with 99.92% culture medium content) containing various concentrations of **TPEPy-I** or **TPEPy-PF6** (0-10 μM) were added to each well. After 4 h of additional incubation, the cells were treated with or without 10 W of MW radiation (2450 MHz) in the dark condition for 1.5 min (inserting the probe of MW into the culture medium without touching the surface of the plate) and further incubated for 20 h. The old medium was then removed, and 400 μL of fresh culture medium containing 40 μL of MTT solution (5

mg/mL MTT reagent in PBS) was added to each well and incubated for another 4 h in the dark. Then, the formazan product was solubilized by adding DMSO, and the absorption of the formazan crystal was recorded at 540 nm using a microplate reader (Multiskan FC). Finally, cell viability was determined using the following equation:

$$\text{Cell viability} = \frac{\text{The absorbance of the treated group}}{\text{The absorbance of the untreated group}} \times 100\%$$

3.2.9. Investigation of MWDT effect using live/dead assay

We further explored the cell viability under MW irradiation by using a live/dead assay. HeLa cells were cultured at a density of 1×10^5 cells/well and then incubated at 37 °C in a humidified 5% v/v CO_2 atmosphere in a cell incubator for 24 h. Following the incubation, the old medium was removed, and 3 mL of fresh medium (DMF-culture medium with 99.92% culture medium content) with or without 10 μM of **TPEPy-I** and **TPEPy-PF6** was then added to each well. There were nine groups: control, **TPEPy-I**, **TPEPy-PF6**, 1.5 min MW, 2 min MW, **TPEPy-I** + 1.5 min MW, **TPEPy-I** + 2 min MW, **TPEPy-PF6** + 1.5 min MW, and **TPEPy-PF6** + 2 min MW. After incubating for 4 h, the MW, **TPEPy-I** + MW, and **TPEPy-PF6** + MW groups were irradiated with 1.5 or 2 min of MW (10 W; 2450 MHz) through the radiator probe (inserting the probe into the medium without touching the plate surface) in the dark condition. Afterward, the cells were incubated in the incubator for 20 h. On the day of the experiment, the old medium was replaced with 500 μL of fresh medium containing a mixture of calcein-AM and propidium iodide (PI) and incubated for another 45 min at 37 °C under the dark condition. Finally, the stained cells were visualized by the OLYMPUS IX71 fluorescence microscope.

3.2.10. Bright-field imaging

In order to observe the changes in the morphology of the cells after MW treatments, bright-field images of the HeLa cells were collected with the help of the OLYMPUS IX71 fluorescence microscope.

3.2.11. Statistical analysis

The data represented as mean ± standard deviation was performed at least three times. One-way analysis of variance (ANOVA) followed by the Tukey test was employed to determine the statistical significance between the control and the experimental groups. A p-value < 0.05 was considered statistically significant.

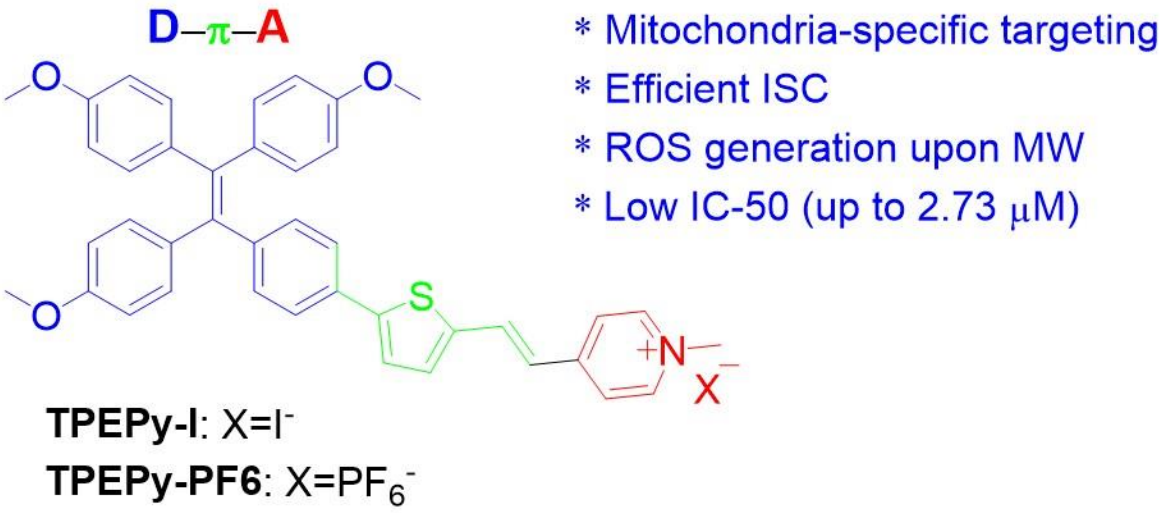

Scheme 3.1. The chemical structures of two MW sensitizers (**TPEPy-I** and **TPEPy-PF6**).

3.3. Results and discussion

3.3.1. Synthesis and characterization of TPEPy-I and TPEPy-PF6

The synthesis and detailed characterizations of the two AIEgens **TPEPy-I** and **TPEPy-PF6** (Scheme 3.1) have been described in our recent publication [131]. Figure 3.1a illustrates the absorption spectra of the **TPEPy-I** and **TPEPy-PF6** nanoaggregates in DMF-water mixture (99.75% water), with the absorption maxima at about 440 and 450 nm, respectively. Figure 3.1b depicts the PLE and PL spectra of the **TPEPy-I** and **TPEPy-PF6** nanoaggregates in DMF-water mixture (99.75% water), with the emission maxima at about 652 and 663 nm, respectively, when excited at 467 nm. Moreover, their PL spectra were found to be almost the same even after 4 months of storage (Figure S3.1), demonstrating their good stability. Dynamic light scattering (DLS) measurements revealed that the mean hydrodynamic diameters of the nanoaggregates that formed in the DMF-water mixture (99.67% water) were (119 ± 32) and (152 ± 48) nm for **TPEPy-I** and **TPEPy-PF6** nanoaggregates (Figures 3.1c and d), respectively.

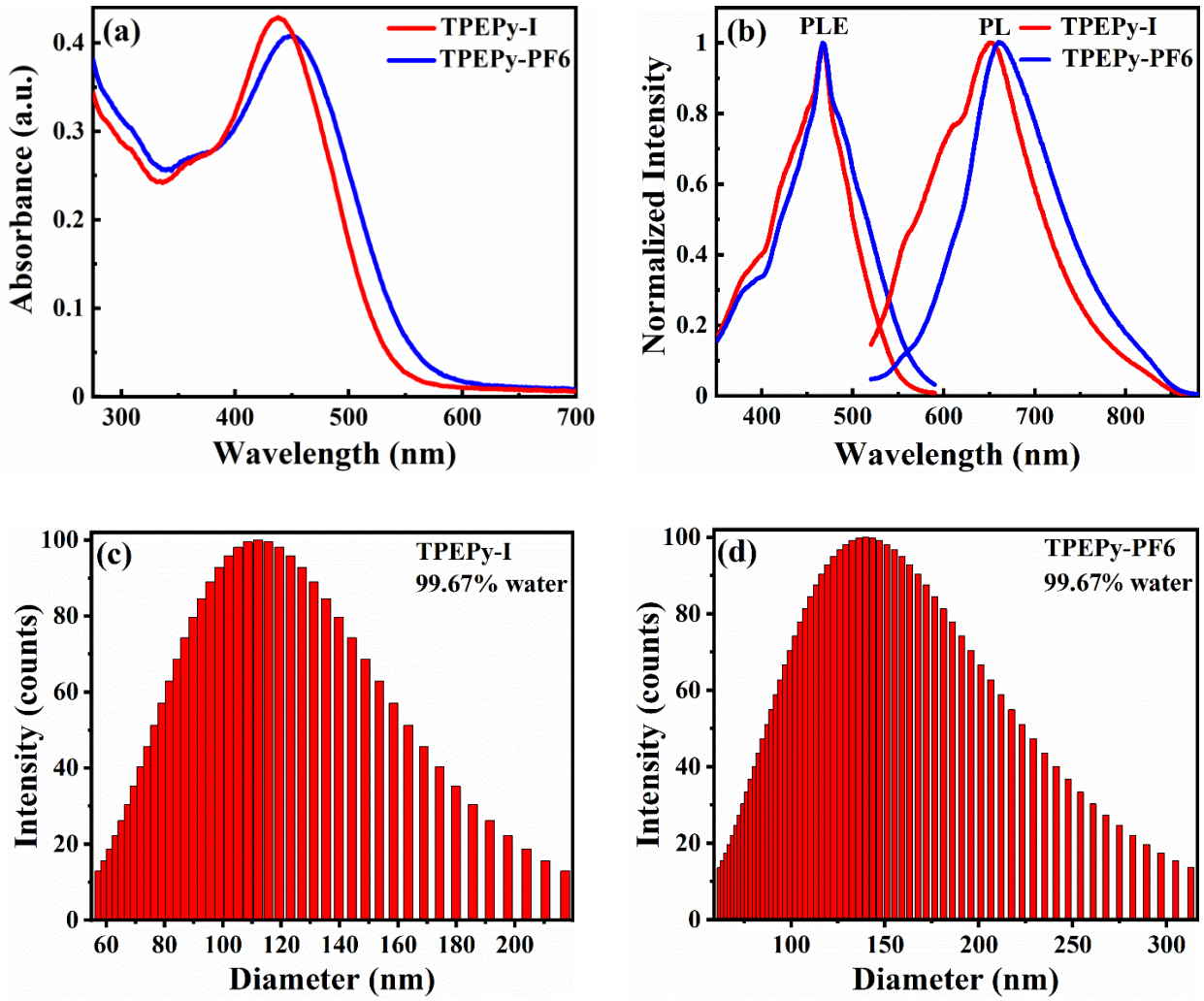

Figure 3.1. (a) UV-vis absorption spectra of **TPEPy-I** and **TPEPy-PF6** nanoaggregates in the DMF-water mixture with 99.75% water content. (b) Normalized photoluminescence excitation (PLE) spectra at 467 nm (left) and PL emission spectra at 652 and 663 nm (right) of the **TPEPy-I** and **TPEPy-PF6** nanoaggregates, respectively, in DMF-water mixture with 99.75% water content. Emission wavelengths of **TPEPy-I** and **TPEPy-PF6** nanoaggregates were 652 and 663 nm, respectively. The excitation wavelength was 467 nm for both cases. (c and d) Particle size distribution of (c) **TPEPy-I** and (d) **TPEPy-PF6** nanoaggregates in DMF-water mixture with 99.67% water content measured by DLS.

3.3.2. Scanning electron microscopy (SEM) and fluorescence microscopy images

We used SEM to investigate the morphology and self-assembly behaviors of both AIEgens. Figures 3.2a-f show that both AIEgens self-assembled into nano/micro-architectures when no water was used. We further carried out SEM measurements when water contents on both AIEgens were 90% and 99.67%. As depicted in Figures 3.2g-o, molecules self-assembled into micro-/nanostructures after the evaporation of water. As solvent needs to be evaporated before performing SEM measurements, only slight difference was observed under different conditions. Since the properties of these AIEgens strongly depend upon water content and all water contents were evaporated before SEM observations, SEM results showed a broader range of sizes than that of DLS measurements. The results of SEM observations suggest that both AIEgens were assembled into different shapes, as it is not easy for AIEgens to self-assemble into well-defined structures due to the nonpolar topology of AIEgens [134]. The aggregation behavior of AIEgens, in essence, is a self-assembly process primarily driven by the solvophobic effect of the molecules [135]. Figure S3.2 shows one of the morphologies of **TPEPy-I** nanoaggregates when molecules of **TPEPy-I** assembled into nanoaggregates.

Additionally, the fluorescence microscopy images clearly showed bright red luminescence in the solid-state (powder samples), and the intensity of red luminescence increased with the size of aggregates (Figure S3.3), further indicating that these are AIE-active molecules.

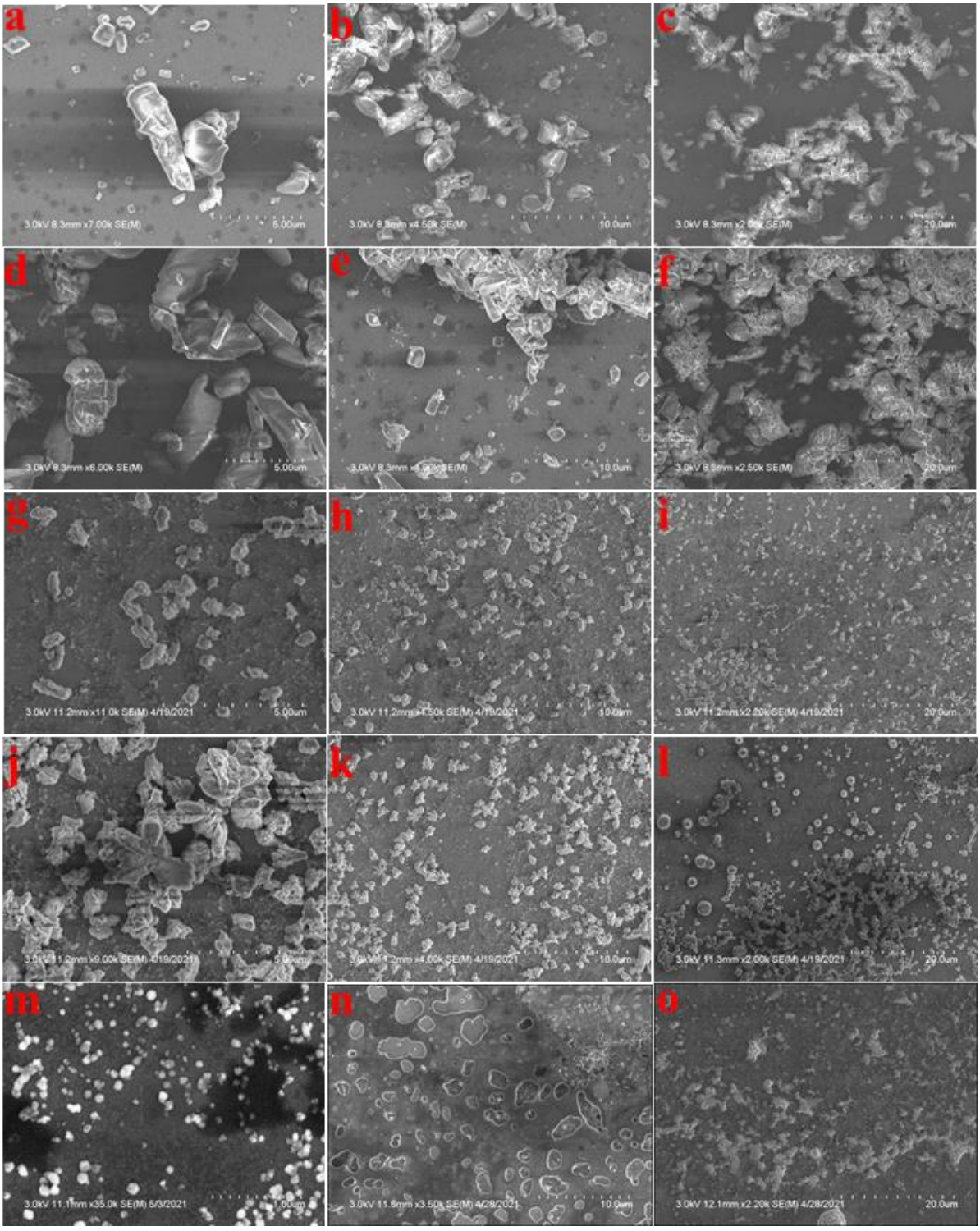

Figure 3.2. Representative SEM images of (a-c) **TPEPy-I** with no water (powder sample), (d-f) **TPEPy-PF6** with no water (powder sample), (g-i) **TPEPy-I** with 90% water content, (j-l) **TPEPy-PF6** with 90% water content, (m-n) **TPEPy-I** with 99.67% water content, and (o) **TPEPy-PF6** with 99.67% water content.

3.3.3. ROS detection in aqueous solution using RNO bleaching assay

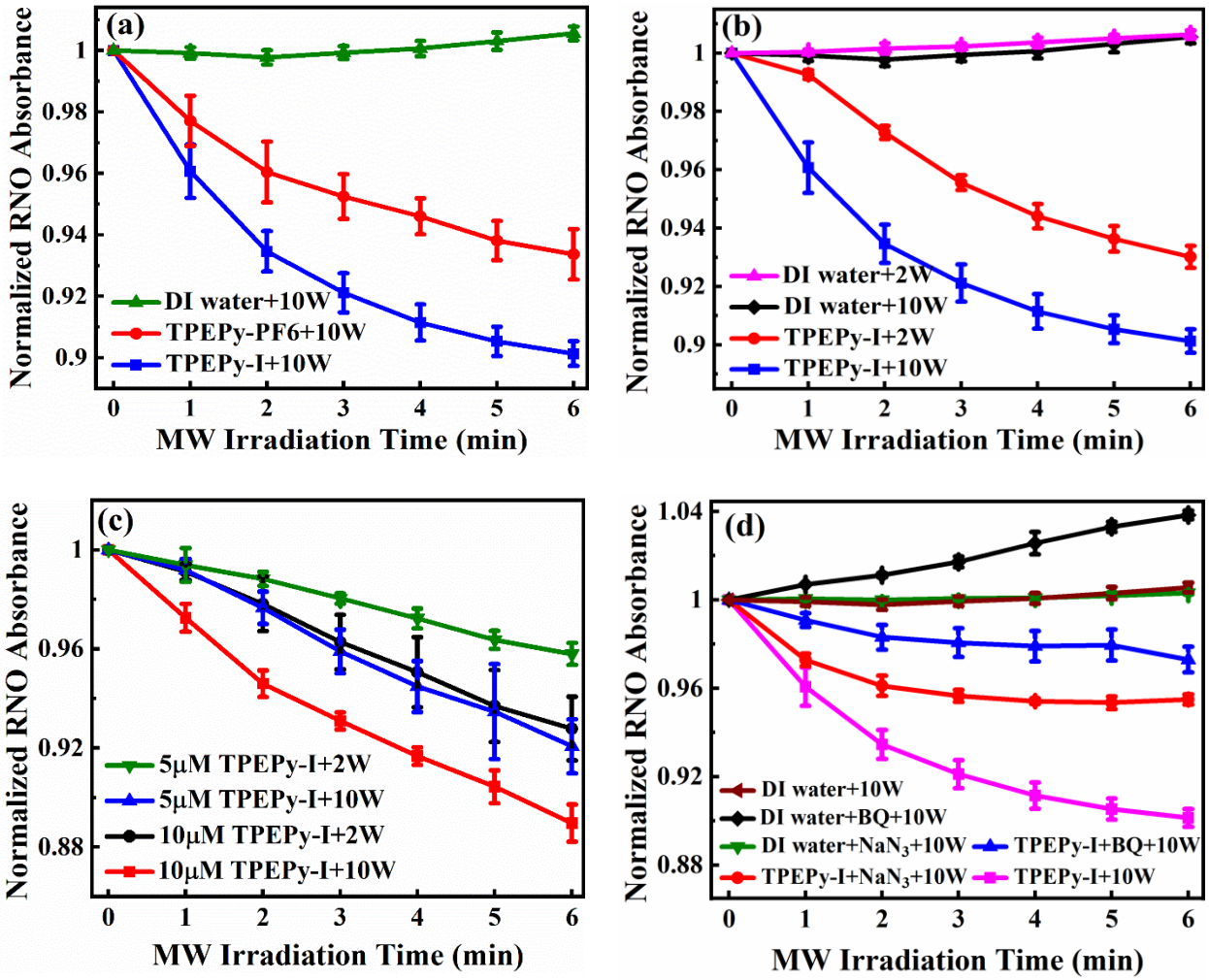

Figure 3.3. Investigation of ROS detection using the RNO bleaching (RNO-imidazole) method. Normalized absorption curves of RNO at 440 nm in the presence of (a) DI water, **TPEPy-I**, or **TPEPy-PF6** under 10 W of MW irradiation, (b) DI water or **TPEPy-I** under 2 and 10 W of MW irradiation, (c) **TPEPy-I** (5 and 10 μM) under 2 and 10 W of MW irradiation, and (d) DI water, BQ, NaN_3, **TPEPy-I**, **TPEPy-I** + NaN_3, or **TPEPy-I** + BQ under 10 W of MW irradiation.

ROS produced by the two AIEgens under MW irradiation was investigated by the RNO bleaching (RNO-imidazole) method [98]. In this spectrophotometric method, the reaction of $^1O_2$ with imidazole yields a transannular peroxide, which then reacts with RNO and causes bleaching of RNO that can be measured at 440 nm [98]. Firstly, we compared the ROS production ability of

TPEPy-I and **TPEPy-PF6** nanoaggregates (10 μM) under 10 W of MW exposure by monitoring the absorbance of RNO at 440 nm as a function of MW exposure time. As presented in Figure 3.3a, the absorbance of RNO was markedly reduced as compared to DI water alone, indicating that the two nanoaggregates could produce ROS when excited by MW. To ascertain that the decrease in the absorption of RNO was due to ROS generation, time-dependent UV-vis absorption spectra of both nanoaggregates (without MW activation) were recorded. As depicted in Figure S3.4, the absorption intensity of both nanoaggregates at 440 nm did not vary noticeably over time, showing that the decrease in RNO absorbance was actually ascribed to the generated ROS from the two nanoaggregates.

It is interesting that **TPEPy-I** induced more ROS, which could be attributed to the positive effect of iodide anions as described in our recent work [69]. An alternative explanation might be due to the smaller size of **TPEPy-I** nanoaggregates (Figures 3.1c and d) as smaller particles have larger surface areas, which are helpful to regulate the number of reactive sites on the particles' surface [136]. However, the exact cause of the difference in ROS generation capacity of the two samples is currently not known.

As discussed above, the ROS production performance of **TPEPy-I** nanoaggregates is better than that of **TPEPy-PF6**, motivating us to carry out further experiments on **TPEPy-I** nanoaggregates. Figure 3.3b shows the comparison of ROS induced by **TPEPy-I** nanoaggregates (10 μM) at 2 and 10 W of MW irradiation. The result indicates that a higher MW dose produces more ROS. Furthermore, ROS production is also dependent on the concentration of the sample (Figure 3.3c). Interestingly, 5 μM of **TPEPy-I** nanoaggregates under 10 W of MW produced the approximately same amount of ROS as that of 10 μM under 2 W of MW (Figure 3.3c). Taken

together, irradiation time, MW dose, and sample concentration proved to be key factors influencing ROS generation.

To test whether the ROS detected from the RNO bleaching assay was $^1O_2$, we added sodium azide (NaN_3), a physical quencher of $^1O_2$ [137], to **TPEPy-I** nanoaggregates under the same conditions. As displayed in Figure 3.3d, the bleaching of RNO was noticeably reduced in the presence of NaN_3 (40 mM) because of the capture of $^1O_2$ by NaN_3, supporting that $^1O_2$ was the main component of the generated ROS.

We all know that $^1O_2$ is usually generated by the energy transfer from the excited state of PSs to molecular oxygen ($^3O_2$). However, some groups revealed that $^1O_2$ may be produced through the oxidation of superoxide radical ($\bullet O_2^-$) under appropriate conditions [7, 138-141]. To verify this hypothesis, we added 1,4-benzoquinone (BQ), a well-known quencher of $\bullet O_2^-$ [142, 143], into the solution of **TPEPy-I** nanoaggregates. Interestingly, the introduction of BQ (340 μM) into the solution of **TPEPy-I** nanoaggregates inhibited bleaching of RNO remarkably (Figure 3.3d), indicating $\bullet O_2^-$ was simultaneously produced in the reaction system. Based on this observation, it is reasonable to expect that $^1O_2$ might be possibly generated by the oxidation of $\bullet O_2^-$ as illustrated in Figure 3.4. From the molecular orbital diagram (Figure 3.4), it is evident that the loss of an electron of appropriate spin could generate either $^1O_2$ or $^3O_2$. The probabilities of $^1O_2$ and $^3O_2$ production through the oxidation of $\bullet O_2^-$ are found to be 2/5 and 3/5, respectively [7]. The confirmation of the production of $\bullet O_2^-$ also indicates the possibility of the generation of other types of ROS as well because $\bullet O_2^-$ is the precursor of most of the ROS and is a mediator of oxidative chain reactions [144]. It is worthwhile to mention that the increase in RNO absorbance at 440 nm of DI water + BQ +10 W group (black curve in Figure 3.3d) is due to the interaction of imidazole with BQ [145]. As can be seen in Figure S3.5a, the absorption of RNO at 440 nm did not change

in the presence of BQ, indicating that RNO does not interact with BQ. However, the absorption of RNO at 440 nm slightly increased in the presence of imidazole and BQ (Figure S3.5c), which suggests that imidazole interacts with BQ as discussed in the literature [145]. Figure S3.5d further shows that the interaction becomes more prominent upon MW irradiation.

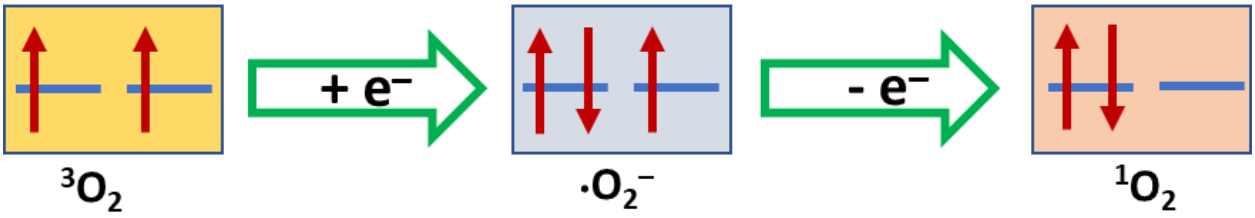

Figure 3.4. The schematic molecular π* orbitals of molecular oxygen ($^3O_2$), superoxide radical ($\bullet O_2^-$), and singlet oxygen ($^1O_2$).

We also used another scavenger of $\bullet O_2^-$, chloroform [143, 146, 147], to further strengthen our claim that the nanoaggregates can generate $\bullet O_2^-$ upon MW radiation. After adding chloroform (4.2 or 21 mM) to **TPEPy-I** solution, the bleaching of RNO was noticeably reduced (Figure S3.6a), indicating that the nanoaggregates could produce $\bullet O_2^-$ under MW irradiation.

Additionally, the absorbance of RNO was also monitored without using imidazole to further affirm the production of $^1O_2$ (Figure S3.6b). If the system generates $^1O_2$, the bleaching of RNO should reduce in the absence of imidazole. As expected, the bleaching of RNO was significantly inhibited in the absence of imidazole as compared to the sample with imidazole (Figure S3.6b), further demonstrating that the sample can generate $^1O_2$ upon MW exposure.

For the purpose of comparison, we synthesized copper-cysteamine (Cu-Cy) nanoparticles using the recently published method [29] and compared the ROS production performance of **TPEPy-I** nanoaggregates (10 μM) with Cu-Cy nanoparticles (10 μM) under the same experimental conditions. As depicted in Figure S3.7, **TPEPy-I** nanoaggregates produced a significantly higher amount of ROS than that of Cu-Cy nanoparticles, justifying that **TPEPy-I** nanoaggregates are better ROS producing agent than Cu-Cy nanoparticles upon MW irradiation.

3.3.4. Study of $^1O_2$ measurements using ABDA probe and electron spin resonance (ESR) spectroscopy

The generation of $^1O_2$ from the two nanoaggregates upon MW irradiation was also assessed by using ABDA, a commercially available $^1O_2$ indicator [132]. ABDA can react with $^1O_2$ to form an endoperoxide, resulting in a decrease in the absorbance of ABDA. As indicated in Figure 3.5a, a slight reduction in the absorbance of ABDA was observed even in the absence of the samples, signifying that MW alone caused some oxidation of ABDA. In contrast, after adding **TPEPy-I** or **TPEPy-PF6** (15 μM) to the ABDA solution, a rapid decrease in the intensity of ABDA absorbance was noticed with increasing the MW exposure time (Figure 3.5a), which is an indication of $^1O_2$ generation and provided compelling evidence of $^1O_2$ production. As expected, **TPEPy-I** nanoaggregates exhibited a much more effective $^1O_2$ generation, consistent with what was observed during the RNO bleaching assay.

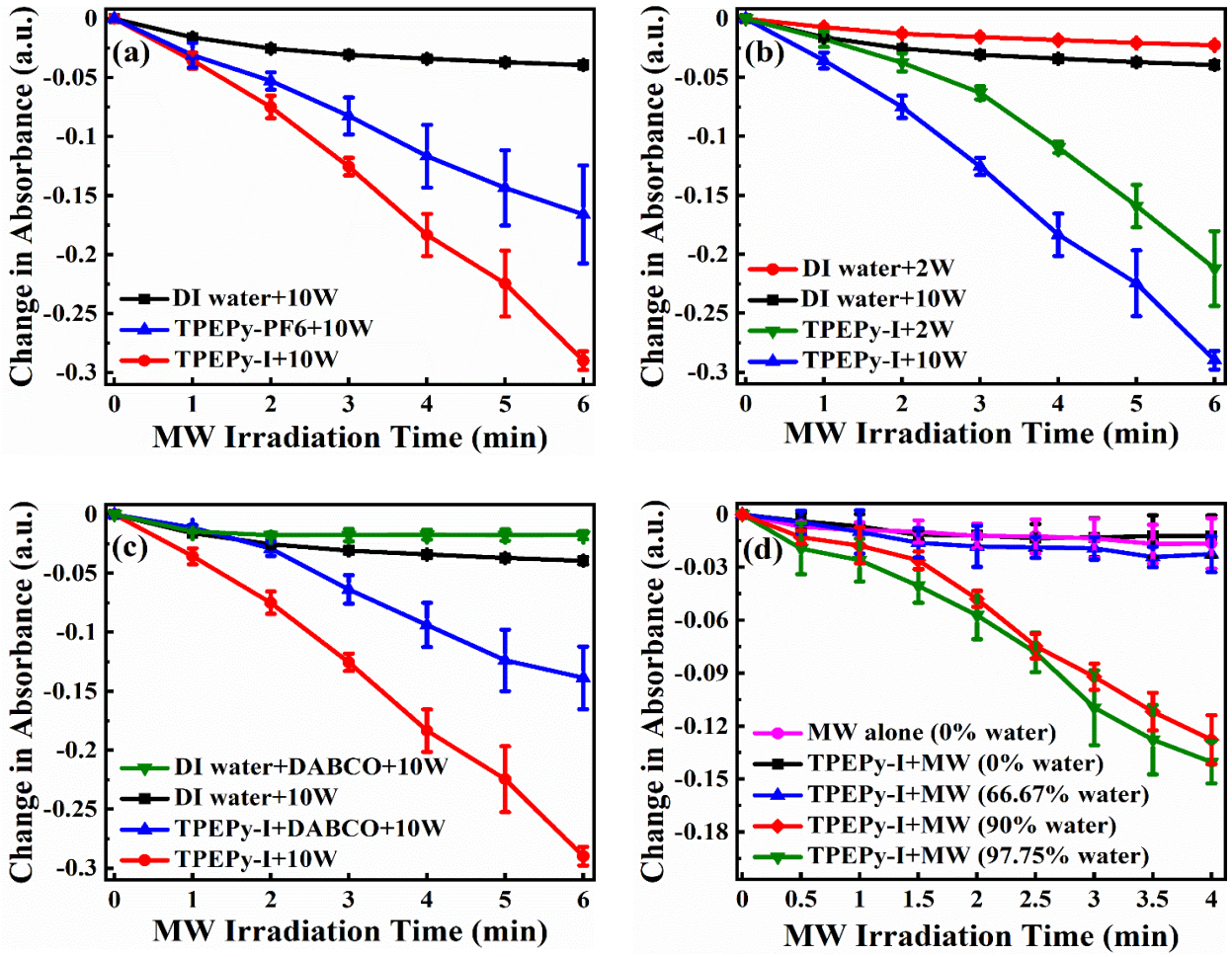

Figure 3.5. Exploration of singlet oxygen ($^1O_2$) detection using the ABDA probe. Change in ABDA absorbance at 379 nm as a function of MW exposure time with (a) **TPEPy-I** or **TPEPy-PF6** nanoaggregates under 10 W of MW irradiation, (b) **TPEPy-I** nanoaggregates under 2 and 10 W of MW irradiation, (c) DABCO, **TPEPy-I** + DABCO, or **TPEPy-I** under 10 W of MW irradiation, and (d) **TPEPy-I** in the presence of different water contents in DMF under 10 W of MW irradiation. The decrease in absorbance at 379 nm shows $^1O_2$ production.

As **TPEPy-I** generated more $^1O_2$, we further measured $^1O_2$ produced by **TPEPy-I** (15 μM) upon 2 W of MW radiation. The results presented in Figure 3.5b reveal that $^1O_2$ produced by **TPEPy-I** varies with MW power. To validate that decrease in ABDA absorbance was due to the generation of $^1O_2$, we mixed DABCO, a well-known scavenger of $^1O_2$ [137], to the solution of **TPEPy-I** (15 μM). As displayed in Figure 3.5c, the decrease in ABDA absorbance was markedly

inhibited in the presence of the DABCO (20 mM), further testifying that the **TPEPy-I** nanoaggregates could generate $^1O_2$ upon MW exposure.

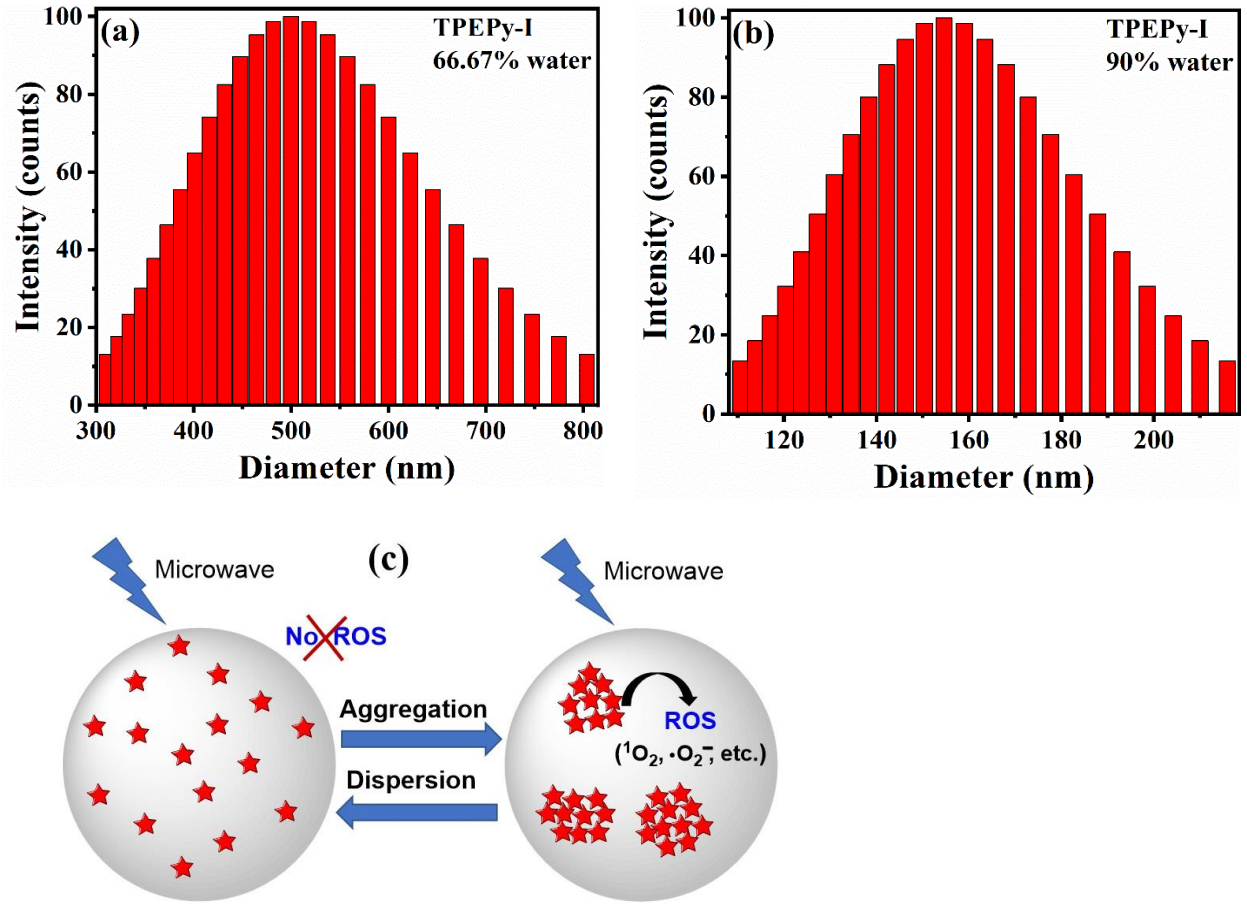

Figure 3.6. The particle size distribution of nanoaggregates of **TPEPy-I** formed in DMF-water mixture with (a) 66.67% and (b) 90% water content measured by DLS. The average hydrodynamic diameters were found to be (517 ± 108) and (157 ± 24) nm, respectively. (c) Schematic diagram of the AIEgen-mediated microwave dynamic therapy (MWDT).

To examine whether the molecularly dissolved state can produce $^1O_2$ upon MW excitation, we chose **TPEPy-I** as an example for further investigation. Figure 3.5d reveals that **TPEPy-I** solution could not induce $^1O_2$ in the molecular form (0% water). Surprisingly, no obvious $^1O_2$ generation was observed even when the water content was 66.67%. However, further increasing

water content (90% or 97.75%), **TPEPy-I** generated a large amount of $^1O_2$. All of these findings indicate that MW can generate $^1O_2$ only when compact nanoaggregates are formed, as demonstrated by DLS measurements (Figures 3.6a and b). The AIEgen-mediated MWDT is schematically illustrated in Figure 3.6c.

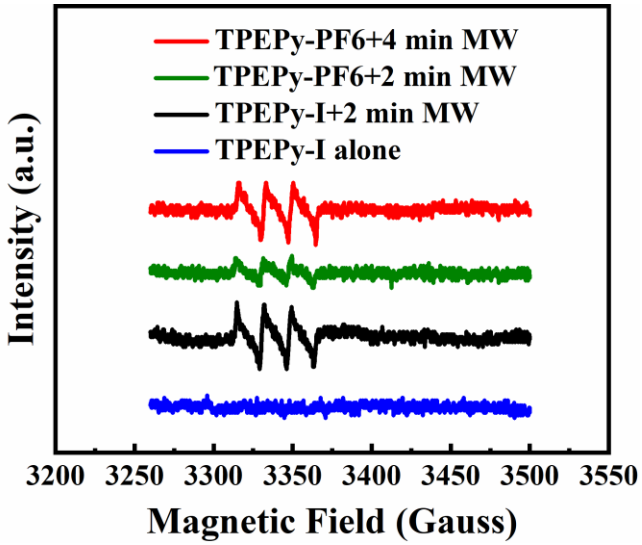

Figure 3.7. ESR spectra of $^1O_2$ trapped by TEMP in the presence of **TPEPy-I** and **TPEPy-PF6** nanoaggregates (10 μM) under 10 W of MW irradiation. Concentration of TEMP was 20 mM.

ESR technique was used to further verify the production of $^1O_2$ using 2,2,6,6-tetramethylpiperidine (TEMP), a well-known probe molecule for trapping $^1O_2$. The oxidation of TEMP by $^1O_2$ yields the stable free radical 2,2,6,6-tetramethyl-1-piperidinyloxy (TEMPO), which can be easily detected by ESR [148, 149]. As shown in Figure 3.7, the distinguishable and typical 1:1:1 triplet signal (i.e., three lines with equal intensities) of the TEMPO was detected after applying MW irradiation on **TPEPy-I** nanoaggregates (10 μM), thereby providing direct evidence of the generation of $^1O_2$ [148, 149]. However, such a noticeable characteristic signal of the TEMPO was not observed without MW irradiation. Similarly, we conducted experiments on **TPEPy-PF6** nanoaggregates to see if **TPEPy-PF6** nanoaggregates (10 μM) could produce $^1O_2$, and results

showed that **TPEPy-PF6** nanoaggregates could generate $^1O_2$ when excited by MW (Figure 3.7). Additionally, $^1O_2$ produced by **TPEPy-I** nanoaggregates was more than that of **TPEPy-PF6**, consistent with all our studies.

3.3.5. Detection of extracellular ROS production using DCFH-DA probe

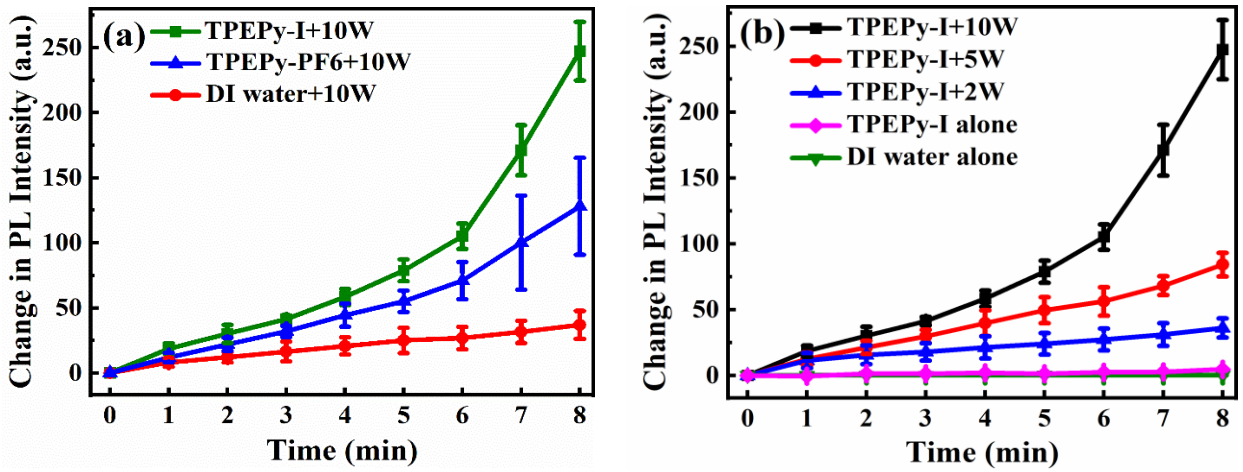

Figure 3.8. Extracellular ROS detection using the DCFH-DA probe. (a) Change in photoluminescence (PL) intensities of DCF at 523 nm as a function of MW exposure time with or without **TPEPy-I** and **TPEPy-PF6** nanoaggregates (10 µM) under 10 W of MW irradiation. (b) Comparison of change in PL intensities of DCF at 523 nm in the presence of **TPEPy-I** nanoaggregates (10 µM) at 2, 5, and 10 W of MW irradiation. The increase in PL intensity at 523 nm indicates the ROS generation.

The evaluation of ROS generation was also explored by the PL technique using DCFH-DA, which yields DCF, a fluorescent molecule, in the presence of ROS [31, 46]. As shown in Figure 3.8a, it is evident that the PL intensity at 523 nm enhanced to a greater extent after using **TPEPy-I** or **TPEPy-PF6** nanoaggregates when compared to the DI water alone, demonstrating that the **TPEPy-I** and **TPEPy-PF6** nanoaggregates can produce ROS upon MW exposure. Taking **TPEPy-I** as an example, we further evaluated the ROS produced by the **TPEPy-I** nanoaggregates at 2 and 5 W of MW irradiation. The results presented in Figure S3.8 demonstrate that the

nanoaggregates could produce ROS even at 2 W of MW irradiation. For comparison, Figure 3.8b was plotted, which shows that ROS production ability enhanced with the increase of MW power.

3.3.6. Intracellular ROS detection

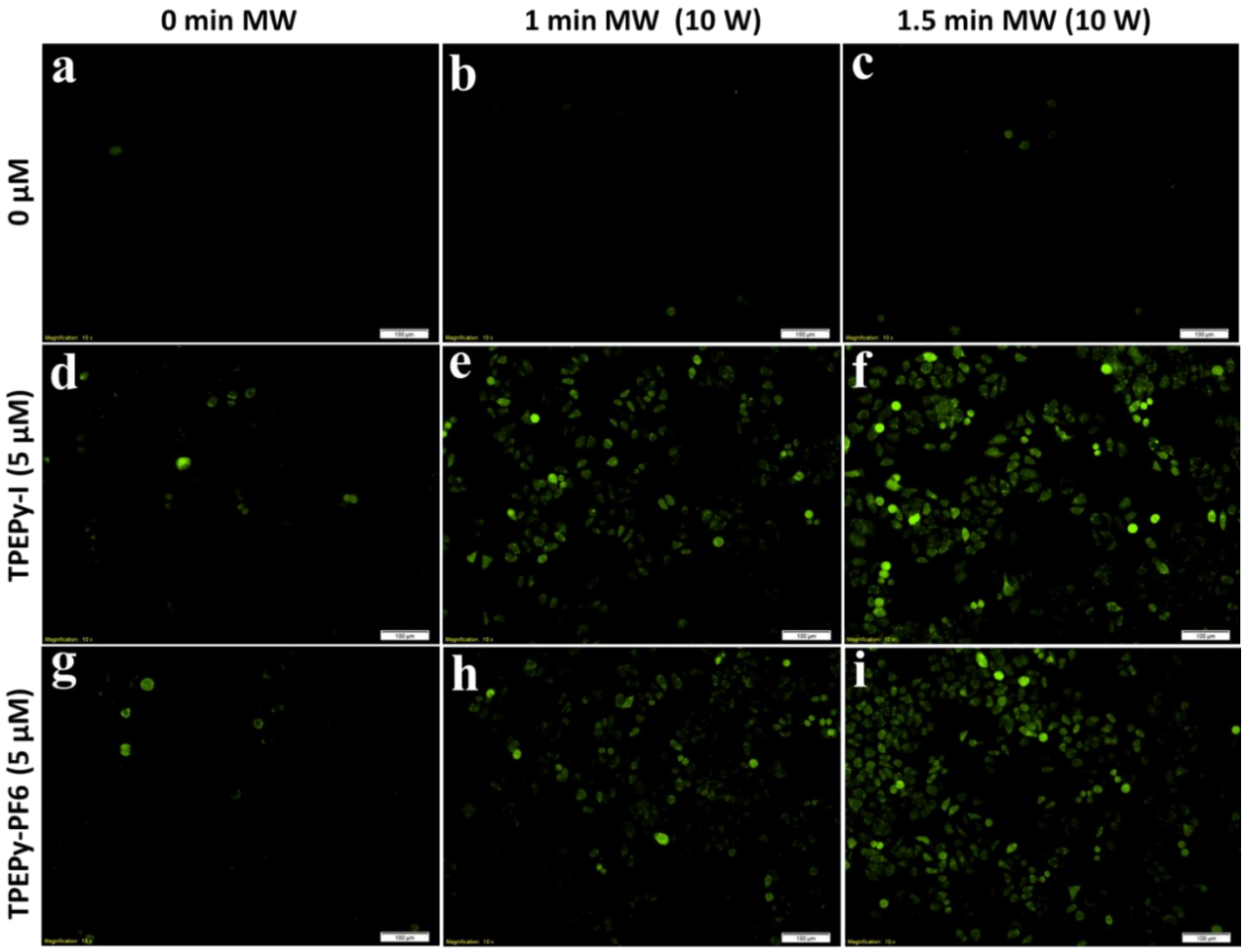

Figure 3.9. Intracellular ROS detection in HeLa cells using DCFH-DA staining dye upon 10 W of MW irradiation. (a) Cells without any treatments. (b) Cells treated with MW for 1 min. (c) Cells treated with MW for 1.5 min. (d) Cells treated with **TPEPy-I**. (e) Cells treated with **TPEPy-I** upon MW for 1 min. (f) Cells treated with **TPEPy-I** upon MW for 1.5 min. (g) Cells treated with **TPEPy-PF6**. (h) Cells treated with **TPEPy-PF6** upon MW for 1 min, and (i) cells treated with **TPEPy-PF6** upon MW for 1.5 min. The increase in green fluorescence intensity shows ROS production. Scale bar = 100 µm; magnification = 10×.

The results of ROS production in cell-free system motivated us to explore ROS detection in cells. DCFH-DA, an oxidation-sensitive probe, was used to examine the intracellular ROS generation. DCFH-DA is a nonpolar and cell-permeant compound, which switches to DCFH by intracellular esterases and then converts to the intensely fluorescent DCF upon oxidation with intracellular ROS [133]. The representative images presented in Figure 3.9 demonstrate that negligible green fluorescence was seen in the MW (1 or 1.5 min, 10 W) treated cells, whereas the cells treated with **TPEPy-I** or **TPEPy-PF6** nanoaggregates (5 μM) displayed weakly green fluorescence. Meanwhile, the intensity of green fluorescence was dramatically increased in the cells treated with the **TPEPy-I** or **TPEPy-PF6** nanoaggregates in combination with MW, proving that the two nanoaggregates can remarkably produce ROS when stimulated by MW. Additionally, the intensity of green fluorescence was further enhanced after increasing the MW exposure time from 1 to 1.5 min. These findings also support that the two AIEgens can produce ROS under MW exposure and are promising sensitizers for MWDT.

3.3.7. Exploration of MWDT effect using MTT assay

We evaluated the MWDT effect of the two AIEgens using MTT assay. It is a quantitative colorimetric assay in which yellow tetrazolium salt MTT converts into purple formazan crystals by mitochondrial dehydrogenase of the metabolically active cells [150]. The results presented in Figure 3.10 shows that MW-treated nanoaggregates killed significantly more cells than their corresponding controls (MW alone and nanoaggregates alone). Furthermore, our results depict that the lethality increased with the increase of concentration of **TPEPy-I** and **TPEPy-PF6** nanoaggregates, demonstrating a dose-dependent cytotoxic effect. These results confirmed that the combination of MW and **TPEPy-I** or **TPEPy-PF6** nanoaggregates had a fatal effect on HeLa cells. For example, the average HeLa cell viabilities were found to be 58.4% vs. 62.5%, 31.1% vs.

36.7%, and 9.3% vs. 14.2% at 2.5, 5, and 10 µM of **TPEPy-I** and **TPEPy-PF6** nanoaggregates, respectively, under 10 W of MW irradiation for 1.5 min. Even though it may not be fully reasonable to compare our findings with the reported results due to some differences in the experimental methods, the high MWDT effect of the two AIEgens even at low concentration indicates that the present AIEgen system is better than most MW sensitizers reported thus far, which require high concentrations to achieve the desired cytotoxicity [27-34].

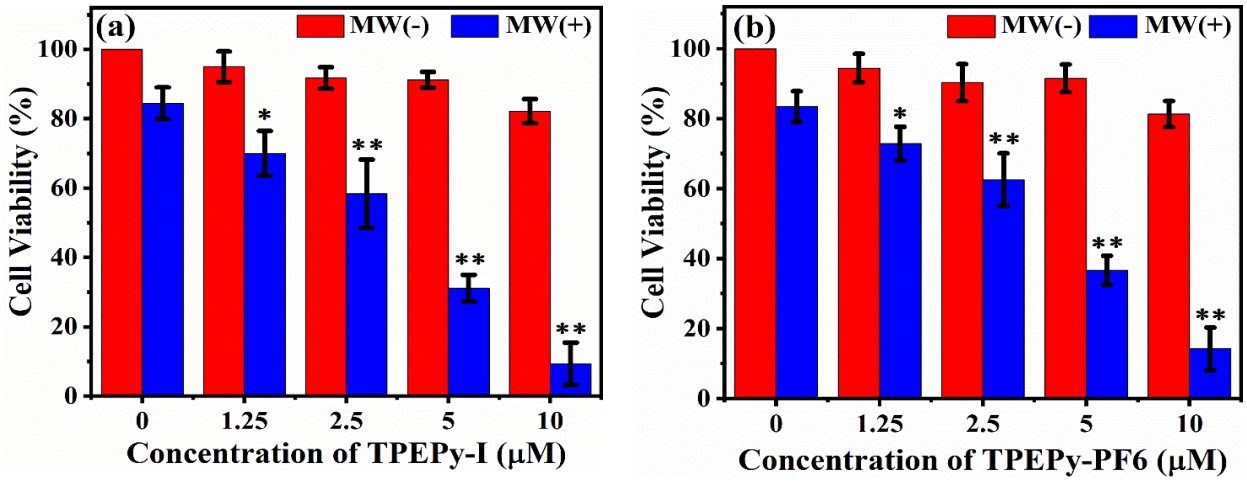

Figure 3.10. Evaluation of MWDT effect of (a) **TPEPy-I** and (b) **TPEPy-PF6** nanoaggregates under MW irradiation (10 W) on HeLa cells for 1.5 min. Statistical analysis was performed with respect to MW alone and the corresponding concentration of the nanoaggregate alone (*$p < 0.05$ and **$p < 0.0001$).

The IC-50 values of **TPEPy-I** and **TPEPy-PF6** nanoaggregates upon MW were found to be (2.73 ± 0.52) and (3.22 ± 0.55) µM, respectively (Figure 3.11). This means that **TPEPy-I** nanoaggregates showed a better MWDT effect on average, which agrees with the ROS production and cytotoxicity studies.

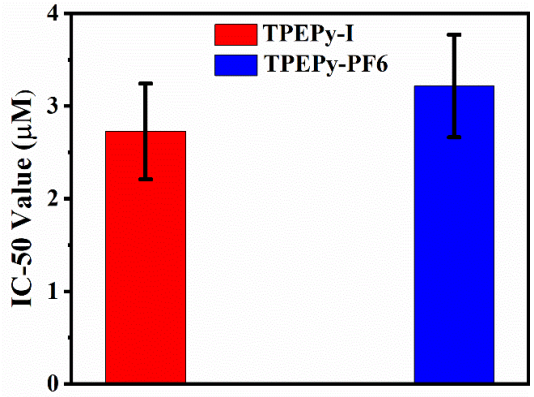

Figure 3.11. The plot of IC-50 values of **TPEPy-I** and **TPEPy-PF6** nanoaggregates against HeLa cells under 10 W (1.5 min) of MW exposure.

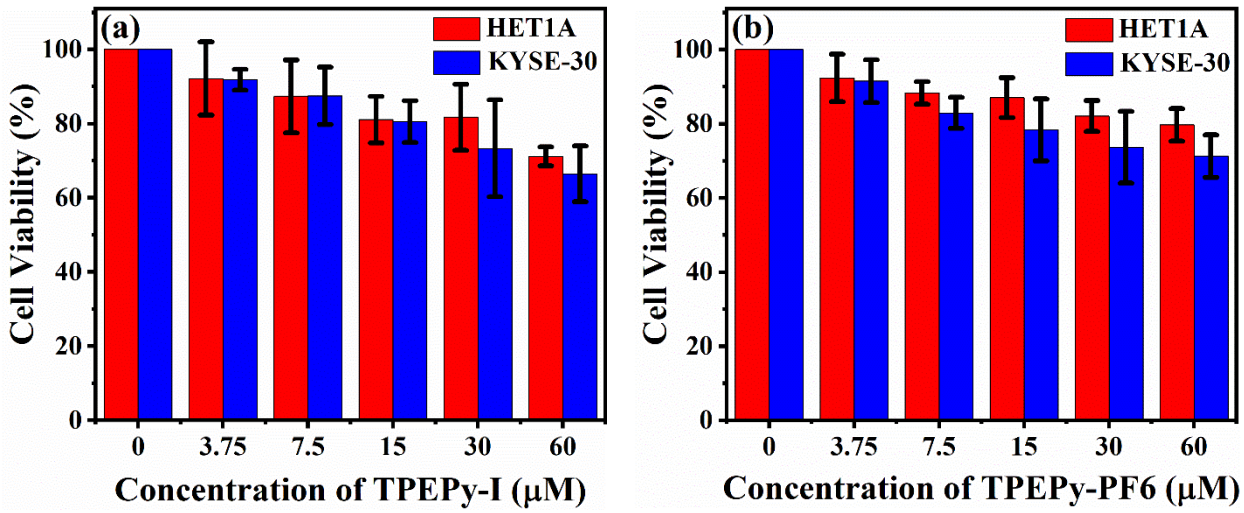

Figure 3.12. Cell viability of HET1A normal cells and KYSE-30 cancer cells under the dark condition after treating different concentrations of (a) **TPEPy-I** and (b) **TPEPy-PF6** nanoaggregates for 24 h.

The toxicity of materials is a very important factor to be evaluated for biological applications. Therefore, we further assessed the dark toxicity of the two nanoaggregates in both normal and cancer cells (other than HeLa cancer cells). As displayed in Figure 3.12, the nanoaggregates have relatively low dark toxicity in both cancer and normal cells up to tested

concentrations. Additionally, the average dark toxicity for HET1A (normal cells) for most concentrations was found to be slightly lower than that of KYSE-30 (cancer cells). These results suggest that these nanoaggregates should have acceptable biocompatibility in normal cells *in vivo*.

3.3.8. MWDT study by live/dead assay

The anti-tumor effect induced by **TPEPy-I** and **TPEPy-PF6** nanoaggregates upon MW exposure was also assessed by using the live/dead cell viability assay. HeLa cells were stained with calcein-AM for viable cells and PI for nonviable cells. Calcein-AM is a cell-permeable dye that has been widely employed for determining cell viability and/or cytotoxicity in most eukaryotic cells. In viable cells, the calcein-AM is switched to a green fluorescent calcein by intracellular esterases [151]. On the other hand, PI is excluded from live cells with intact plasma membranes but penetrates damaged cells, thereby binding to nucleic acids and detecting dead cells in a population [133].

For each group, the green (live) and red (dead) channels were merged, and the representative images of the live/dead assay are shown in Figure 3.13. When **TPEPy-I** or **TPEPy-PF6** nanoaggregates were activated by 1.5 or 2 min of MW (10 W), the cytotoxicity was significantly enhanced when compared to their corresponding controls (MW alone and nanoaggregates alone). The results presented in Figure 3.13 further show that more cells were destroyed while increasing the MW exposure time (from 1.5 to 2 min), uncovering that **TPEPy-I** and **TPEPy-PF6** nanoaggregates are promising candidates in MWDT for noninvasive treatment of deep tumors and infectious diseases. For the purpose of quantification, the number of live (green fluorescence) and dead (red fluorescence) cells were counted to determine the cell viability by using ImageJ software [70], and the results are displayed in Figure 3.14. The average cell viabilities of the HeLa cells in the presence of **TPEPy-I** and **TPEPy-PF6** nanoaggregates under 10 W of MW exposure were

found to be 23.8% and 29.1% for 1.5 min and 4.7% and 7.5% for 2 min, respectively (Figure 3.14). Again, this means that **TPEPy-I** nanoaggregates exhibited a better MWDT outcome on average than **TPEPy-PF6** nanoaggregates, which could be due to the effect of iodide ions, as pointed out in our recent publication [69].

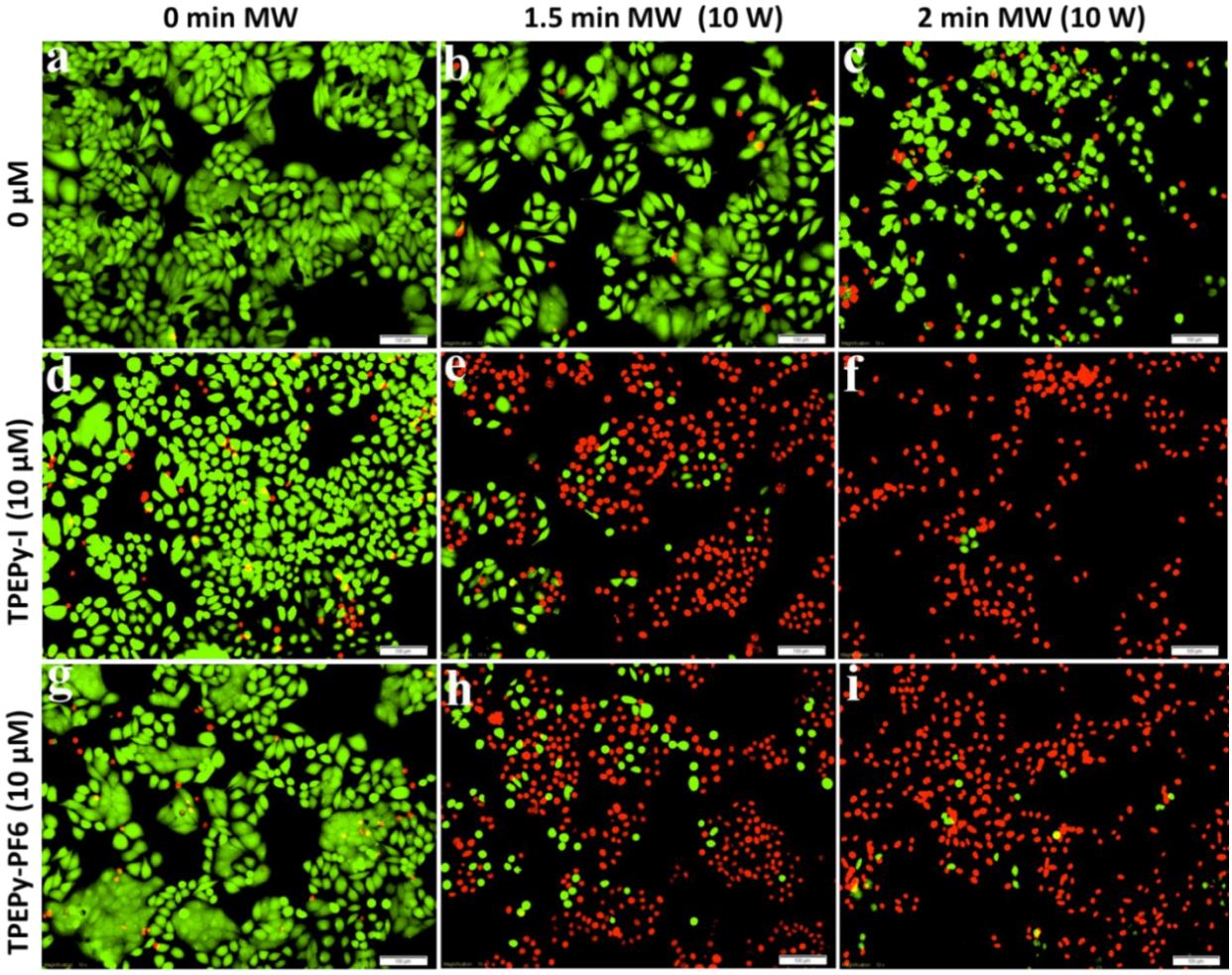

Figure 3.13. The effect of **TPEPy-I** and **TPEPy-PF6** nanoaggregates (10 µM) in HeLa cells upon 10 W of MW irradiation. (a) Cells without any treatments. (b) Cells treated with MW for 1.5 min. (c) Cells treated with MW for 2 min. (d) Cells treated with **TPEPy-I**. (e) Cells treated with **TPEPy-I** upon MW for 1.5 min. (f) Cells treated with **TPEPy-I** upon MW for 2 min. (g) Cells treated with **TPEPy-PF6**. (h) Cells treated with **TPEPy-PF6** upon MW for 1.5 min, and (i) cells treated with **TPEPy-PF6** upon MW for 2 min. Green fluorescence represents viable cells, whereas red fluorescence represents dead cells. Scale bar = 100 µm; magnification = 10×.

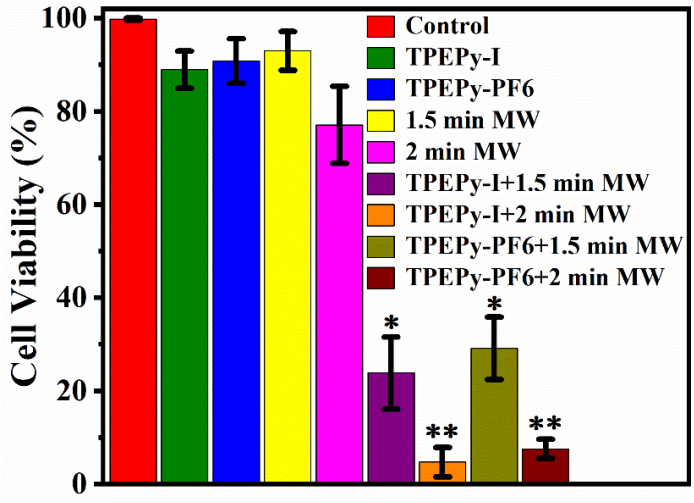

Figure 3.14. The quantitative analysis of the live/dead cell assay using ImageJ software. *p < 0.0001 compared with 1.5 min MW alone and the corresponding nanoaggregate alone; **p < 0.00001 compared with 2 min MW alone and the corresponding nanoaggregate alone.

3.3.9. Bright-field images

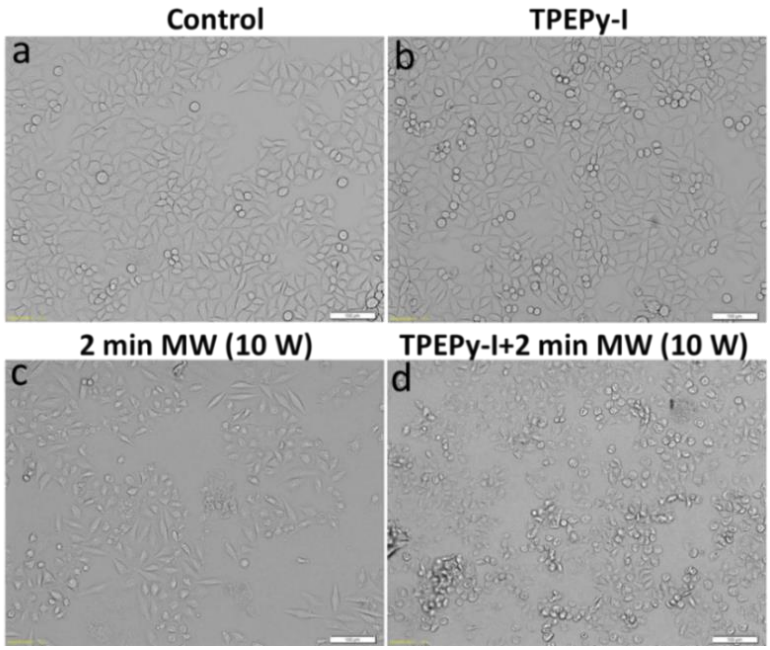

Figure 3.15. Bright-field images of HeLa cells (a) without any treatments (control), (b) treated with **TPEPy-I** (10 μM), (c) treated with MW for 2 min, and (d) treated with **TPEPy-I** (10 μM) upon MW for 2 min. Scale bar = 100 μm; magnification = 10×.

We also monitored the changes in the morphology of the HeLa cells following the MW treatments. As shown in Figure 3.15, the cells treated with **TPEPy-I** nanoaggregates alone retained their regular and normal cell morphology, indicating low dark cytotoxicity towards HeLa cells. In contrast, MW plus nanoaggregates induced a dramatic change in cell morphology, thus corroborating that the combination of the nanoaggregates and MW is highly toxic to cancer cells. The results agreed well with the results of the MTT and live/dead assays.

3.3.10. ROS production and MW heating

Despite several groups, including ours, great efforts in elucidating the mechanisms of MW induced ROS generation, the exact mechanism is not completely understood yet because MW irradiation does not have sufficient energy to break chemical bonds or to induce any chemical reactions [31, 50]. One of the plausible rationalities is that a portion of MW energy could be concentrated into hot spots, which could cause the transfer of electrons from the nanoaggregates to the surrounding water and oxygen, thereby producing ROS [31, 51]. Another possibility could be attributed to the catalytic effect of the nanoaggregates, similar to that of other materials such as Cu-Cy nanoparticles [29], g-C_3N_4 quantum dots [27], gold nanoparticles [103], and activated carbon [51]. Additionally, non-thermal effect of MW may cause excitation of reactant molecules to higher vibrational and rotational energy levels [60, 152, 153]. Shahin *et al.* [154] discussed that the non-thermal effect of MW could be responsible for increasing ROS production. Although the exact mechanism of ROS production is still controversial, it is well accepted that MW irradiation forces polar molecules to continuously realign with the oscillating electric field, enhancing their kinetic energy and, in turn, heat [41, 50]. Tissues with high water content (such as solid organs and tumors) are highly conducive to this type of heating [41]. Increasing evidence support that heat can mediate for ROS production, including $^1O_2$ [115, 133, 155].

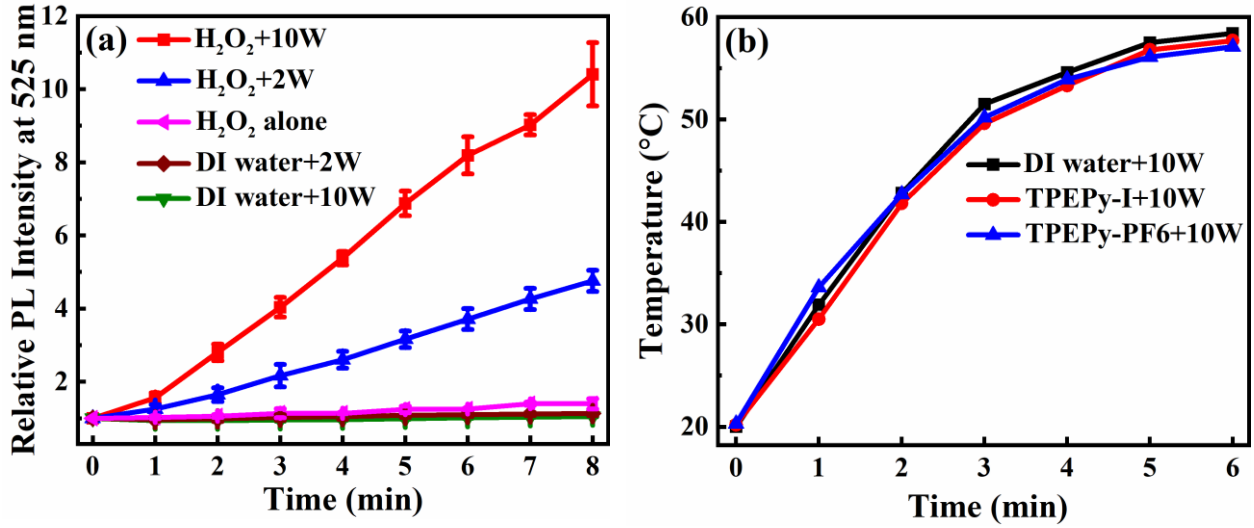

Figure 3.16. (a) The relative PL intensity of SOSG at 525 nm with or without H_2O_2 (100 μM) as a function of time upon 2 and 10 W of MW irradiation. The increase in PL intensity at 525 nm represents the $^1O_2$ generation. The excitation wavelength was 505 nm. (b) In vitro MW heating curves of **TPEPy-I** and **TPEPy-PF6** nanoaggregates dispersed in DI water upon 10 W of MW irradiation. DI water was set as a control.

To determine whether MW irradiation can produce $^1O_2$ through the dismutation of hydrogen peroxide (H_2O_2), we employed singlet oxygen sensor green (SOSG) reagent, which can react with $^1O_2$ and emit bright green fluorescence peaked at about 525 nm [156]. When H_2O_2 (100 μM) was stimulated by MW (2 and 10 W), the normalized PL intensity at 525 nm enhanced remarkably as compared to H_2O_2 alone and MW alone in both time- and dose-dependent manners (Figure 3.16a), thereby providing strong evidence that MW can generate $^1O_2$ by decomposing H_2O_2. In fact, ROS production by MW is a common phenomenon, which has been reported as a great concern for mobile phone impact on human health due to their increased use in daily life [157-159].

To elucidate the heating effect of MW, temperatures of DI water with or without the two nanoaggregates were recorded at 10 W of MW irradiation (2450 MHz) up to 6 min. As displayed in Figure 3.16b, the temperature of the DI water in the presence of **TPEPy-I** or **TPEPy-PF6**

nanoaggregates (20 μM) was not higher than in the DI water alone, suggesting MW thermal effect is unlikely to be a major factor for killing cancer cells and excluding the possibility that these nanoaggregates may increase the temperature of MW heating. Based on this observation and our findings as described above, it is reasonable to expect that the destruction of cancer cells is primarily due to ROS, and, therefore, we define it microwave dynamic therapy (MWDT).

It is known that photodynamic therapy (PDT) suffers from a key drawback associated with its oxygen-dependent nature, which limits its effective use against hypoxic tumors [24, 160]. Many strategies have been explored to solve this problem and improving blood flow in tumors is one of them [24]. Since tumor hypoxia is particularly caused by the alterations in tumor microenvironments and the chaotic blood flow, improving blood flow has become an effective approach to increase oxygenation in tumors. It has been reported that elevating local temperatures by a mild heating may increase blood flow in tumors and an increment of the oxygen level inside tumor [24]. Therefore, microwave induced photodynamic therapy with the microwave heating along with the dynamic therapy of ROS is a good combination on cancer treatment, not only improve the efficacy but also could provide a good solution for hypoxic issues.

3.4. Conclusions

For the first time, we presented that two AIEgens (**TPEPy-I** and **TPEPy-PF6**) can produce ROS and, in turn, kill cancer cells under MW irradiation. We employed different methods to affirm that the two AIEgens can induce ROS upon MW exposure. The AIEgens showed significant cytotoxicity when excited by MW toward HeLa cells as evaluated by the MTT and live/dead assays. Considering NIR emission, good stability, and effectiveness for killing cancer cells even under low concentration of **TPEPy-I** or **TPEPy-PF6** nanoaggregates, we anticipate that these

nanoaggregates could be deserving candidates for further investigation in the study of image-guided MWDT, either alone or in combination with other treatment modalities, such as radiotherapy, chemotherapy, immunotherapy, or surgery. This novel work opens a new door to provide an effective perspective on the molecular design of AIEgens to approach clinical application and improve the efficacy of cancer treatments.

Conflicts of interest

There are no conflicts to declare.

Acknowledgments

We would like to acknowledge the supports from Guangxi Jialouyuan Medical Inc., Solgro, and the distinguished award from UT Arlington as well as the supports from the China Scholarship Council (201906155012), the National Natural Science Foundation of China (22071065, 21772045), the Natural Science Foundation of Guangdong Province (2018B030311008), and the Technology Program of Guangzhou (201904010414). We would also like to acknowledge Dr. Kytai Nguyen for helping with DLS measurements and Alexios Papadimitratos for ESR measurements. LL would like to acknowledge support by the Welch Foundation grant number AT-1877-20180324 and the UT Dallas-NRUF Collaborative Biomedical Research Award (CoBRA).

Supplementary Information

Aggregation-Induced Emission Luminogens for Highly Effective Microwave Dynamic Therapy

Nil Kanatha Pandey[1], Wei Xiong[2], Lingyun Wang[1, 2*], Wei Chen[1]*, Brian Bui[1], Jian Yang[3], Eric Amador[1], Mingli Chen[4], Christina Xing[1], Aseem Atul Athavale[5], Yaowu Hao,[5] Wirya Feizi[6], and Lloyd Lumata[6]

[1] Department of Physics, The University of Texas at Arlington, Arlington, TX 76019, USA.

[2] Key Laboratory of Functional Molecular Engineering of Guangdong Province, School of Chemistry and Chemical Engineering, South China University of Technology, Guangzhou, China, 510640.

[3] Department of Biomedical Engineering, The Pennsylvania State University, University Park, PA, 16802, USA.

[4] Department of Chemistry, College of Sciences, Northeastern University, Box 332, Shenyang 110819, China.

[5] Department of Materials Science and Engineering, The University of Texas at Arlington, Arlington, TX 76019, USA.

[6] Department of Physics, The University of Texas at Dallas, 800 West Campbell Road, Richardson, TX 75080, USA.

*Corresponding authors:

lingyun@scut.edu.cn; weichen@uta.edu

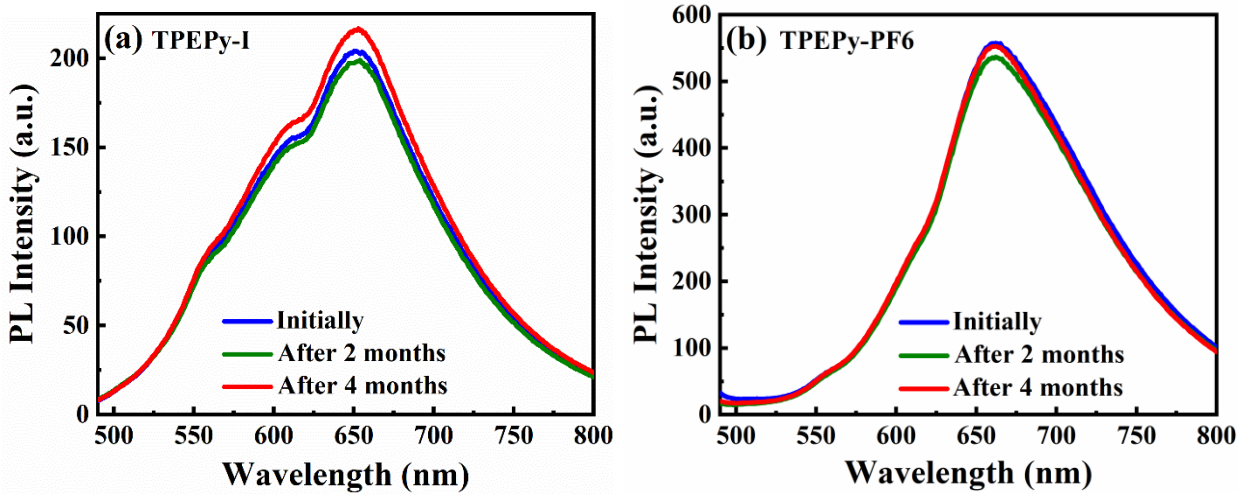

Figure S3.1. Stability study of **TPEPy-I** and **TPEPy-PF6**. (a) Photoluminescence (PL) spectra of the **TPEPy-I** initially and after 2 and 4 months of storage. (b) PL spectra of the **TPEPy-PF6** initially and after 2 and 4 months of storage. The excitation wavelength was 467 nm. Stock solutions were prepared in DMF and diluted with DI water immediately before the measurements. Water content in the DMF-water mixture was 99.75%.

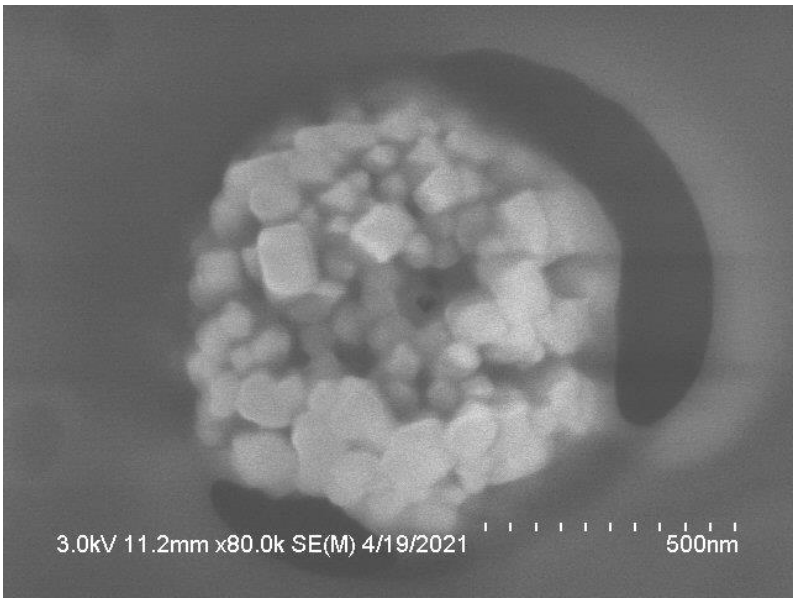

Figure S3.2. SEM image of **TPEPy-I** with 90% water content. The image shows the self-assembly of molecules.

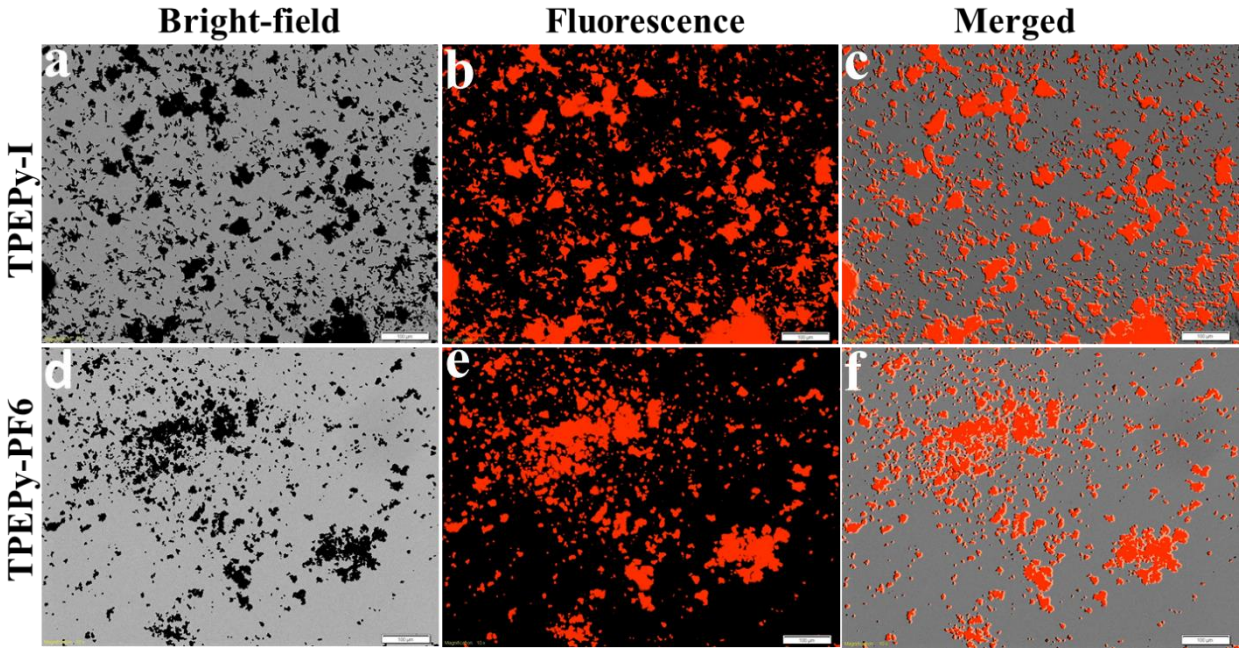

Figure S3.3. Representative fluorescence microscopy images of (a-c) **TPEPy-I** and (d-f) **TPEPy-PF6** in the solid-state. (a) Bright-field, (b) fluorescence, and (c) merged images of **TPEPy-I** powders. (d) Bright-field, (e) fluorescence, and (f) merged images of **TPEPy-PF6** powders. Scale bar = 100 µm.

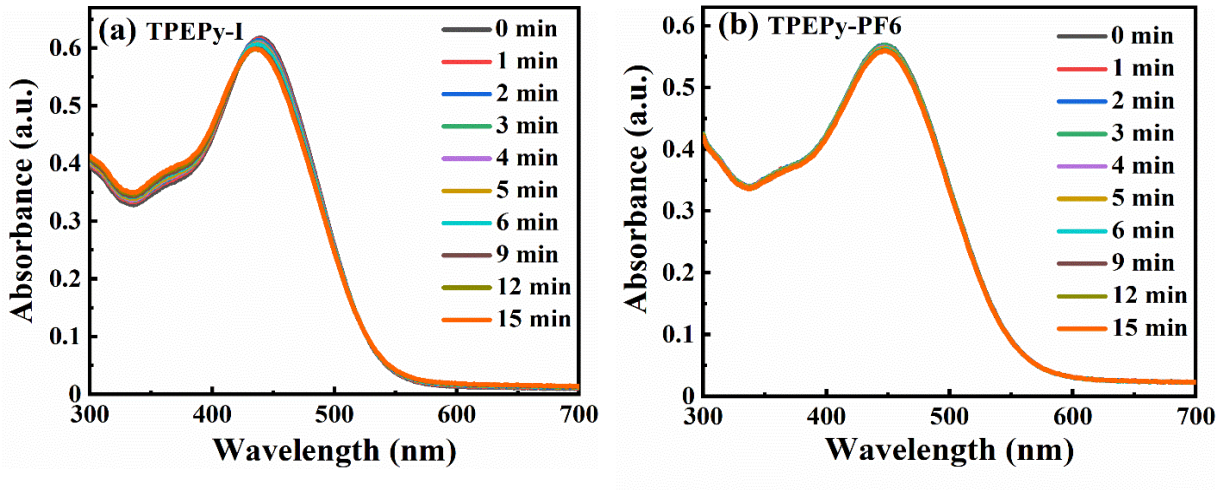

Figure S3.4. Time-dependent UV-vis absorption spectra of (a) **TPEPy-I** and (b) **TPEPy-PF6** nanoaggregates in DMF-water mixture with 99.67% water content for different periods.

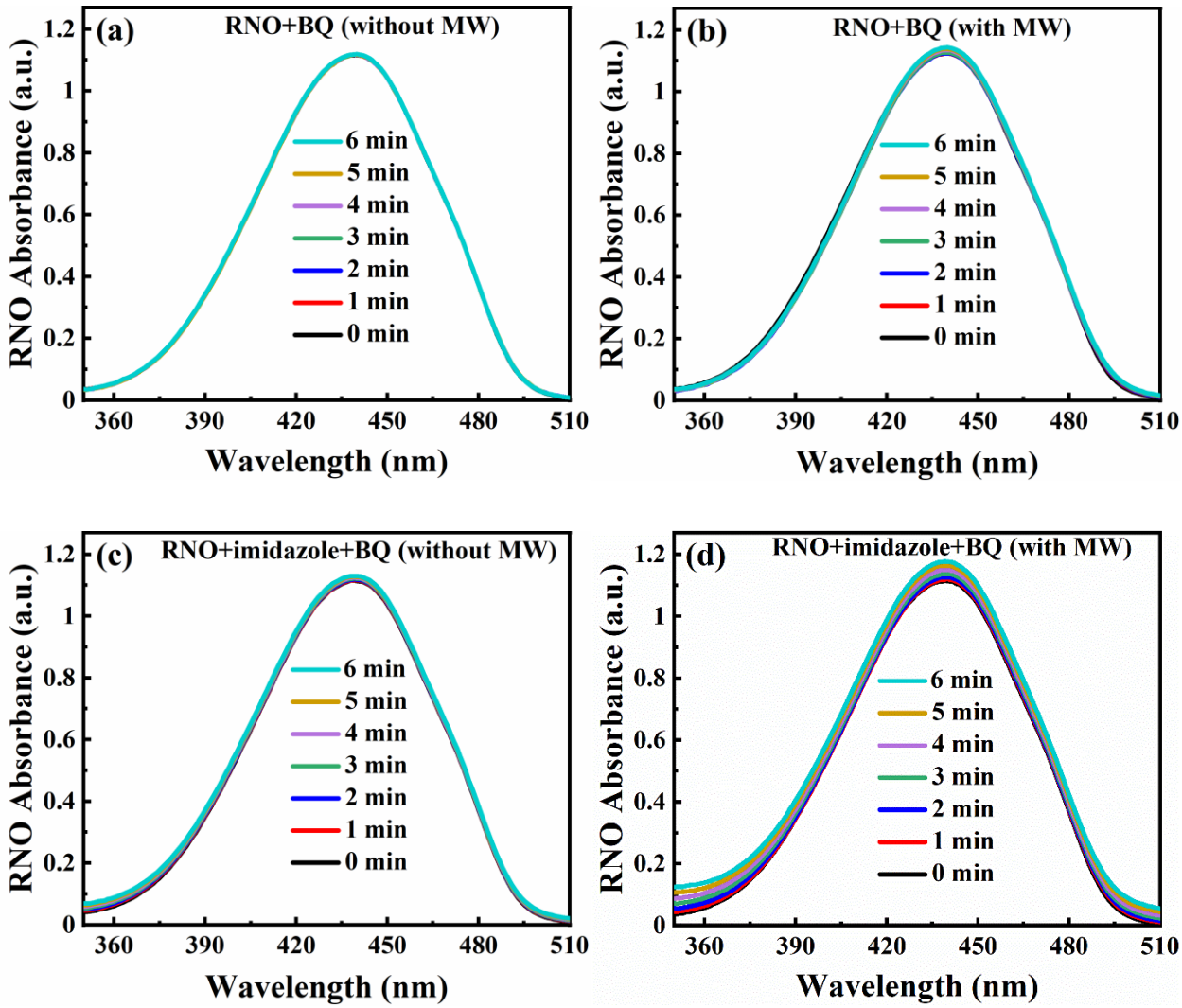

Figure S3.5. (a) Time-dependent absorption spectra of RNO in the presence of BQ (without MW). (b) Time-dependent absorption spectra of RNO in the presence of BQ under 10 W of MW exposure. (c) Time-dependent absorption spectra of RNO in the presence of imidazole and BQ (without MW), and (d) time-dependent absorption spectra of RNO in the presence of imidazole and BQ under 10 W of MW exposure.

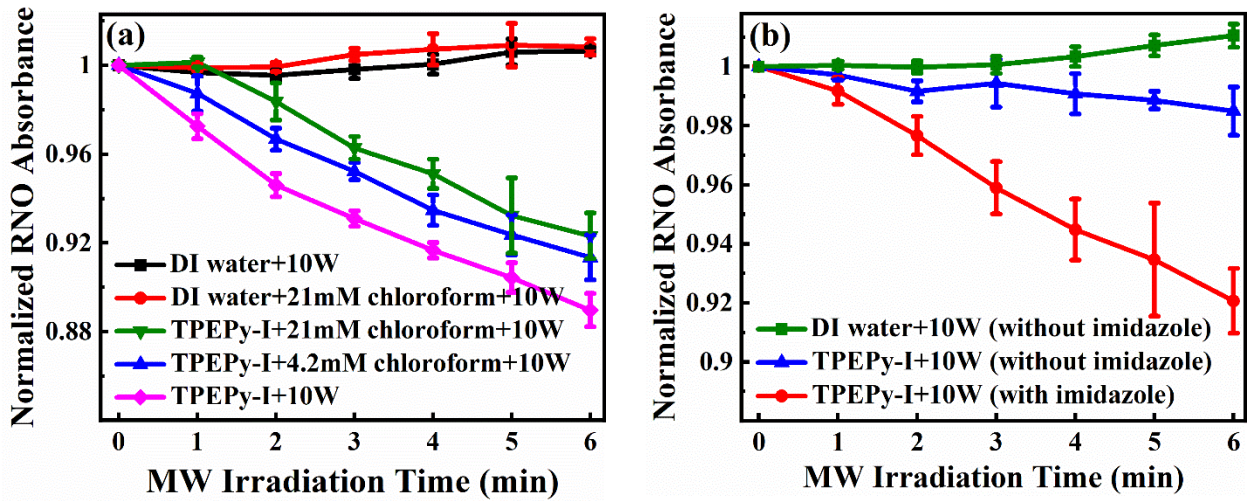

Figure S3.6. (a) Normalized absorption curves of RNO at 440 nm in the presence of DI water, chloroform, **TPEPy-I** (10 μM), or **TPEPy-I** (10 μM) + chloroform under 10 W of MW irradiation. (b) Normalized absorption curves of RNO at 440 nm with **TPEPy-I** (5 μM) in the presence and absence of imidazole upon 10 W of MW irradiation.

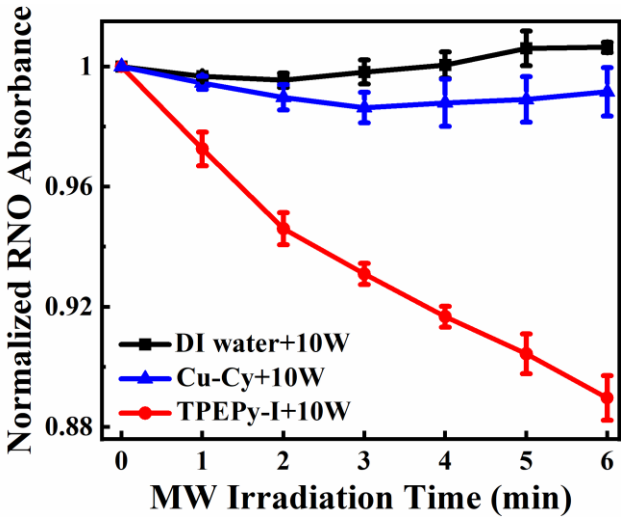

Figure S3.7. Comparison of ROS produced by copper-cysteamine (Cu-Cy) nanoparticles (10 μM) and **TPEPy-I** nanoaggregates (10 μM) under 10 W of MW irradiation using RNO bleaching (RNO-imidazole) method.

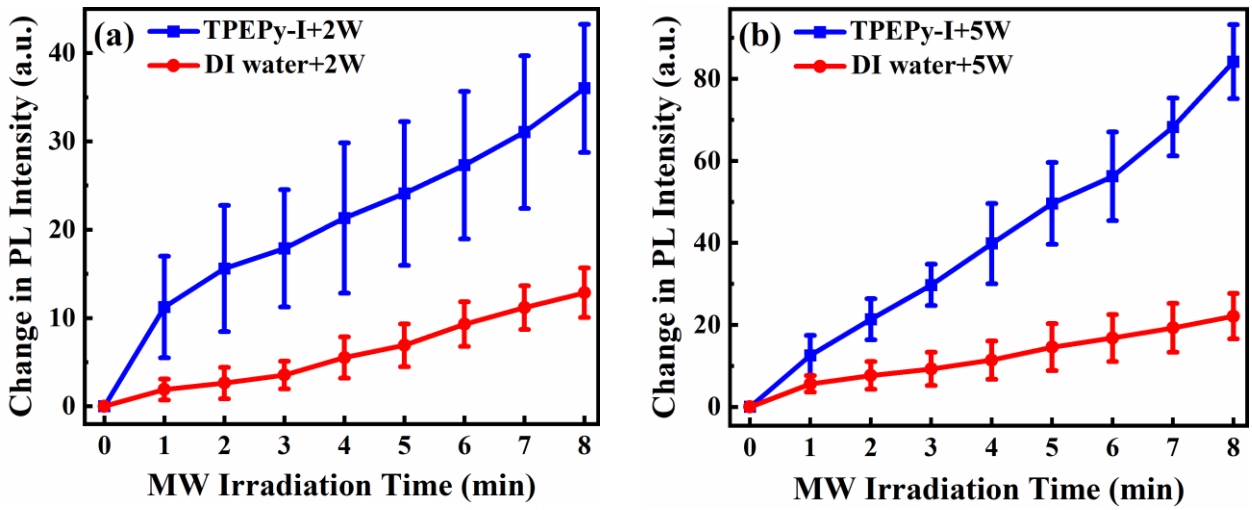

Figure S3.8. Extracellular ROS detection using the DCFH-DA probe. Change in photoluminescence (PL) intensities of DCF at 523 nm as a function of MW exposure time with or without **TPEPy-I** nanoaggregates (10 μM) under (a) 2 W and (b) 5 W of MW irradiation. The increase in PL intensity at 523 nm indicates the ROS generation.

Chapter 4

(In preparation for publication)

Exploration of Copper-Cysteamine Nanoparticles as an Efficient Heterogeneous Fenton-Like Catalyst for Wastewater Treatment

Abstract

Copper-cysteamine (Cu-Cy) is a new nanoparticle that can be stimulated by UV light, microwaves, X-rays, and ultrasound to produce various types of reactive oxygen species (ROS) for cancer and infectious disease treatments. Most importantly, our recent studies revealed that Cu-Cy nanoparticles (NPs) can be used for wastewater treatment as an effective heterogeneous Fenton-like catalyst, thereby adding one more important practical application of this interesting material. Herein, for the first time, we describe the use of Cu-Cy NPs with the assistance of hydrogen peroxide (H_2O_2) as an oxidizing agent for the oxidative degradation of organic contaminants, particularly rhodamine B (RhB), methylene blue (MB), and 4-nitrophenol (4-NP), for wastewater treatment. Additionally, we compared two H_2O_2 oxidation methods for the treatment of RhB and 4-NP: oxidation using H_2O_2/Cu-Cy with or without microwave (MW) irradiation. Our findings show that the degradation rate enhanced when activated by MW irradiation. Furthermore, recycling experiments revealed that Cu-Cy has good stability and recyclability. Overall, it is believed that the Cu-Cy/H_2O_2 system studied in this work could be used in advanced oxidation processes toward the degradation of organic pollutants.

Keywords: Copper-cysteamine; Coumarin; Reactive oxygen species; Methylene blue; Rhodamine B; 4-Nitrophenol

4.1. Introduction

With the excessive population growth, fast industrialization, and rapid urbanization, the influx of considerable amounts of inorganic, organic, and mineral substances into the environment has been increasing significantly over the past centuries. Approximately 2 million tons of sewage, agricultural, and industrial wastes are being discarded worldwide every day into natural aquatic sources, thereby adversely affecting the quality of fresh water and posing a serious threat to human beings and water-dwelling species [161, 162]. Therefore, exploring and developing highly effective and environmentally friendly treatment processes are of utmost importance for both human health and the environment.

Various methods have been used for the degradation of refractory organic contaminants from contaminated water, such as adsorption, precipitation, filtration, biological treatments, and advanced oxidation processes (AOPs) [52, 56, 163]. Among them, AOPs are emerging alternative methods for the efficient removal of many recalcitrant organic contaminants. AOPs operate at near-ambient conditions and produce highly oxidizing radicals (mainly •OH) for the complete destruction of organic contaminants into non-toxic products, such as H_2O and CO_2 [56, 57]. AOPs can also be employed either on their own or in combination with other existing treatments, such as coagulation, filtration, and biological treatments, depending on the chemical composition of pollutants and final treatment objectives [57, 164]. For instance, AOPs can be employed as pre-treatment steps to convert organic contaminants into more readily biodegradable products, which can then be degraded by using biological post-treatments. On the other hand, residual organic fraction from pollutants pre-treated using biological methods can be effectively degraded by applying post-treatment AOPs [57, 164]. Additionally, AOPs are appealing treatment options for decentralized water treatments [58].

Among all AOPs, Fenton-based oxidation systems are the most widely used AOPs since •OH can be generated through the catalytic decomposition of H_2O_2. The Fe-Fenton system (H_2O_2 and Fe catalyst) is the most widely explored Fenton-based technology to remove hazardous organic compounds during wastewater treatment. However, it has two main drawbacks; (1) a narrow pH window (~2.5–3.5), leading to the increased treatment cost due to the pH adjustment, and (2) an excessive amount of generation of ferric hydroxide sludge, resulting in secondary pollution [57, 60]. To circumvent the narrow working pH range of the homogeneous iron catalysts, various heterogeneous catalysts containing iron species (mostly Fe^{3+}) have been exploited. However, heterogeneous iron catalysts also show some shortcomings, such as the reaction between Fe^{3+} and H_2O_2 is at least 3-orders of magnitude slower than that of the classical homogeneous Fenton reaction [57, 163]. Consequently, several studies have concentrated on investigating alternative metal catalysts to replace iron [57, 60]. One approach to overcome this problem is to use Cu (rather than Fe) as Cu-based materials are considered as an effective Fenton-like catalyst in a broad pH range [57, 165, 166]. Additionally, the reaction rate of Cu^+ with H_2O_2 ($k = 1 \times 10^4\ M^{-1}s^{-1}$) is ~150 times higher than that of Fe^{2+} ($k = 63\text{─}76\ M^{-1}s^{-1}$) [57, 165].

Accordingly, if a Cu-based heterogeneous catalyst is to be utilized for wastewater treatment, one of the ways to improve the efficacy of a Cu-containing heterogeneous catalyst is synthesizing the catalyst that has Cu in its reduced state (Cu^+) rather than in its oxidized state (Cu^{2+}) because the reaction rate of Cu^+ is ~22 times faster than that of Cu^{2+} (Eqs. (4.1) and (4.2)) [57].

$$Cu^+ + H_2O_2 \rightarrow Cu^{2+} + OH^- + \bullet OH\ (k = 1.0 \times 10^4\ M^{-1}s^{-1}) \quad (4.1)$$

$$Cu^{2+} + H_2O_2 \rightarrow Cu^+ + \bullet HO_2 + H^+\ (k = 4.6 \times 10^2\ M^{-1}s^{-1}) \quad (4.2)$$

To date, various Cu^{+}-based heterogeneous catalysts have been extensively studied for degrading organic pollutants [166-170]. All of these catalysts are attractive and sensitive for degrading organic pollutants; however, most of these catalysts usually suffer from complicated and/or relatively lengthy synthesis processes. Therefore, exploring a material having an easier and faster synthesis method that exhibits remarkable catalytic properties is very crucial to successfully deal with the increasingly complex problems arising in the field of industrial wastewater treatment for practical applications.

It is worth mentioning the synthesis method of Cu-Cy is straightforward, environment-friendly, easy to approach, and cost-effective [29]. Notably, Cu-Cy has been found as a promising agent for destroying cancer and bacteria cells [29, 62, 65-67, 69-71, 171-173]. However, its application in wastewater treatment has not been previously studied. Herein, for the first time, the degradation of aqueous solutions of two organic dyes (RhB and MB) and one toxic nitroaromatic pollutant (4-NP) were investigated by using Cu-Cy NPs as catalysts. Notably, the catalytic degradation efficiency of Cu-Cy was remarkably enhanced when exposed to MW irradiation. Considering the facile as well as green synthesis method and ROS production ability of Cu-Cy NPs upon different excitation sources, Cu-Cy NPs could be a deserving candidate as a heterogeneous Fenton-like catalyst for rapid degradation of recalcitrant organic contaminants in wastewater.

4.2. Experimental section

4.2.1. Materials

Cysteamine hydrochloride, copper chloride dihydrate ($CuCl_2.2H_2O$), polyethylene glycol 4000 (PEG-4000), sodium hydroxide (NaOH), rhodamine B (RhB), methylene blue (MB), 4-

nitrophenol (4-NP), and coumarin were purchased from Sigma-Aldrich, USA. All chemicals were used without further purification.

4.2.2. Degradation experiments

The catalytic reaction was conducted in a 50 mL glass beaker, which contained 10 mL of appropriate amounts of either RhB or MB dye solution and Cu-Cy NPs. Before adding H_2O_2, the mixture was allowed to react at room temperature and pressure with continuous magnetic stirring in the dark for 30 min to allow the establishment of adsorption/desorption equilibrium. After that, a certain amount of H_2O_2 was added, and the reaction time was noted. At regular time intervals of 3 min, an aliquot (1.3 mL) was withdrawn from the reaction mixture, and the sample was immediately centrifuged at 12,500 rpm for ~25 min. The supernatant was then collected and diluted with deionized (DI) water to determine the rate of dye degradation. In order to monitor the progress of the degradation of the dyes, the absorption spectra were recorded using a Shimadzu spectrophotometer (UV-2450 UV-Vis), and the absorption intensities of RhB and MB were monitored at 553 and 663 nm, respectively. Meanwhile, for the control, the same experiment was performed in the presence of Cu-Cy alone and H_2O_2 alone to determine if Cu-Cy alone and H_2O_2 alone had any influence on the degradation of the dyes. Degradation percentage was determined by using Eq. (4.3).

$$\text{Degradation (\%)} = \frac{(A_0 - A_t)}{A_0} \times 100\% \quad (4.3)$$

where A_0 and A_t are initial and final absorptions of RhB (at 553 nm) or MB (663 nm) after 't' time, respectively. For comparison, $CuCl_2.2H_2O$ with an equivalent concentration of copper was used under the same experimental conditions. All experiments were performed at the natural pH of the pollutants.

4.2.3. Detection of hydroxyl radical (•OH) using a photoluminescence (PL) method

•OH generated by Cu–Cy with H_2O_2 was also verified by a PL method using coumarin as a •OH tracking agent [7, 112]. All experiments were performed in a 50 mL glass beaker under constant magnetic stirring. First, Cu-Cy (0.5 mg/mL) was mixed with coumarin (0.45 mM), and then H_2O_2 (50 mM) was added into the reaction mixture to initiate the reaction. At a designated time, 1.3 mL of the mixture was collected and immediately centrifuged at 12,500 rpm for ~25 min to remove the NPs from the mixture. Afterward, 1 mL of supernatant was collected and diluted three times before each measurement. The PL intensity was subsequently recorded at 452 nm using a Shimadzu spectrofluorophotometer (RF-5301PC) after different reaction times with an excitation wavelength of 332 nm. The control experiments were conducted by taking Cu-Cy alone and H_2O_2 alone under the same experimental conditions.

4.2.4. Investigation of catalytic performance of Cu-Cy upon MW irradiation

The catalytic degradation performance of Cu-Cy NPs under MW exposure was evaluated against RhB and 4-NP. Briefly, the degradation experiment was carried out in a 50 mL measuring cylinder that contained 10 mL mixture of Cu-Cy and RhB or 4-NP solution. Afterward, the mixture was stirred under dark conditions for 30 min to achieve the adsorption/desorption equilibrium. The desired amount of H_2O_2 was then added to the mixture, and MW was applied to the reaction system through a radiator probe using a microwave therapy apparatus (WB-3100AI, China). At fixed time intervals of 2 min, aliquots (0.9 mL) were withdrawn, and the catalysts were removed by centrifuging at 12,500 rpm for ~25 min. Then, the supernatant was collected and diluted with DI water. Finally, the diluted supernatant was analyzed by the UV-vis spectrophotometer. Trapping

experiments were conducted to determine the ROS produced during the catalytic degradation by adding tert-butanol (TBA) and chloroform. To investigate the stability and reusability of the catalyst, the used catalyst was separated by centrifugation, washed with DI water, and then used for the next cycle.

4.3. Results and discussion

4.3.1. Characterizations of Cu-Cy NPs

Cu-Cy NPs were fabricated using the previously published protocol [29]. The detailed characterizations of Cu-Cy have been described in our recent publications [29, 62]. Figure 4.1a illustrates the UV-vis absorption curve of Cu-Cy NPs in DI water, with an absorption maximum at ~365 nm. Figure 4.1b presents the pictures of Cu-Cy in DI water under room light (left) and UV light (right). The photoluminescence excitation (PLE) and emission (PL) spectra of Cu-Cy in DI water are depicted in Figure 4.1c. The emission peaks of Cu-Cy NPs were found to be at ~607 nm and ~633 nm, as pointed out in the literature [29, 62]. Figure 4.1d illustrates the X-ray excited luminescence spectrum of Cu-Cy NPs, with an emission peak at ~633 nm, which is different from PL peak at 607 nm, suggesting that X-ray excited luminescence of Cu-Cy is related to different coordination of Cu ions. Figure 4.1e presents the XRD pattern of Cu-Cy NPs, which matched well with the previous reports [29, 62]. A representative transmission electron microscopy (TEM) image of Cu-Cy NPs used in the present study is depicted in Figure 4.1f.

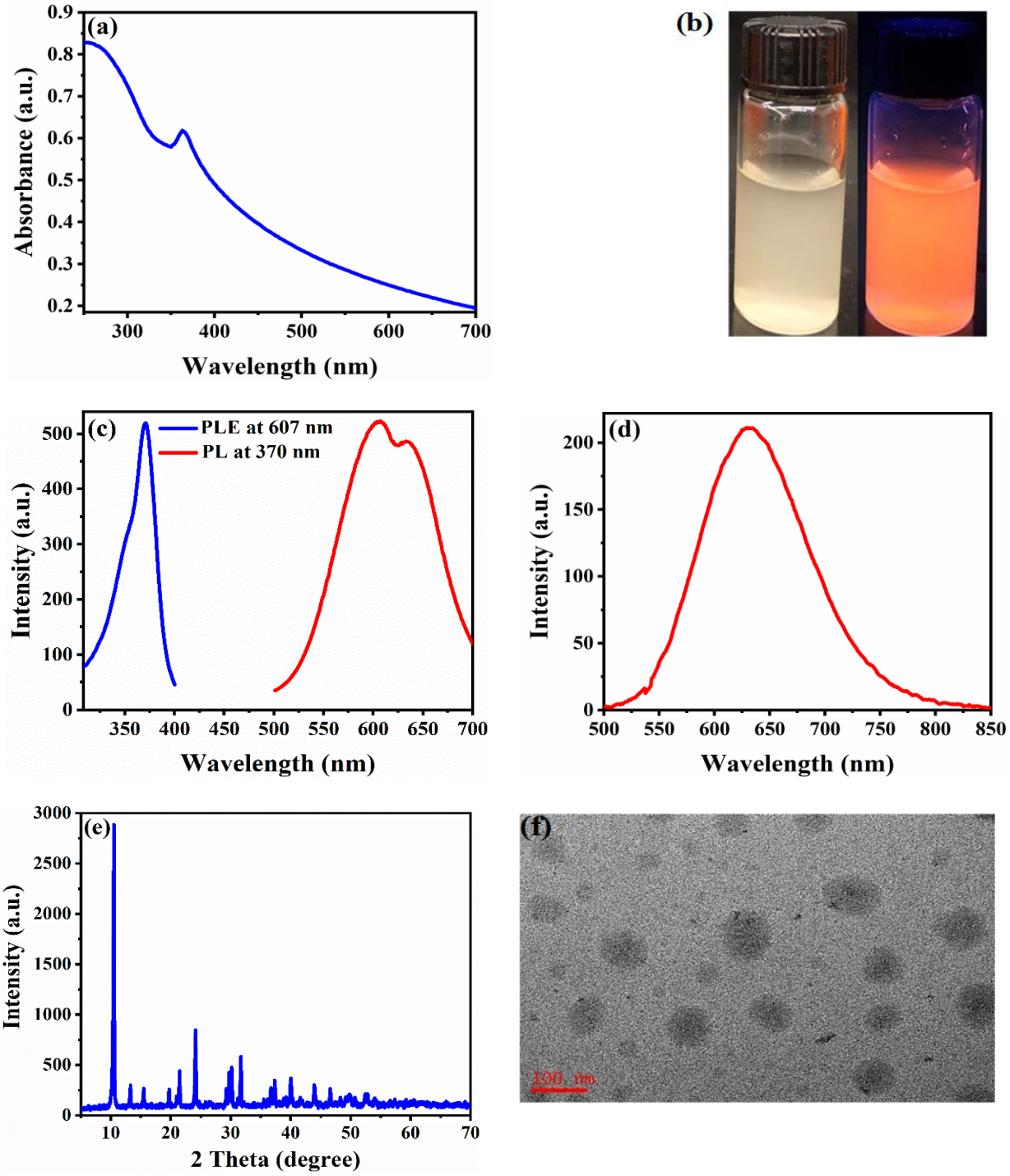

Figure 4.1. (a) UV-visible absorption curve of Cu-Cy NPs dispersed in deionized (DI) water. (b) Images of Cu-Cy suspended in DI water under room light (left) and UV light (right). (c) Photoluminescence excitation (PLE, left) at 607 nm and emission (PL, right) at 370 nm of Cu-Cy in DI water. (d) X-ray excited luminescence spectrum of Cu-Cy NPs. (e) XRD pattern of Cu-Cy NPs. (f) A representative TEM image of Cu-Cy NPs. Scale bar: 100 nm.

4.3.2. Degradation of RhB

The representative UV-vis absorption spectra of RhB dye (24 mg/L) as a function of reaction time up to 15 min with H_2O_2 (50 mM) and Cu-Cy (0.5 mg/mL) are presented in Figure 4.2a. It was found that the removal of RhB proceeded almost instantaneously, with more than 95% of the dye being removed within the first 6 min of operation. The degradation of RhB was the highest during the first 3 min of the reaction, and then it reached a relatively stable value. The control experiments were performed in the presence of Cu-Cy alone (Figure S4.1a) and in the presence of H_2O_2 alone (Figure S4.1b). Neither Cu-Cy nor H_2O_2 alone showed significant degradation of RhB, indicating that the RhB degradation in the present study is indeed through a catalytic process.

In order to compare the catalytic performance of Cu-Cy with $CuCl_2.2H_2O$, a homogenous reaction system containing $CuCl_2.2H_2O$ under the same experimental conditions was also carried out. As depicted in Figure 4.2b, the degradation of RhB with $CuCl_2.2H_2O$ (3.96 mM, which is equivalent to the Cu amount in Cu-Cy) is very slow, in which only ~13% of degradation was seen within 15 min of reaction. This demonstrates that although there could be a homogeneous catalytic contribution resulted from copper leaching, the rapid degradation of RhB observed in the presence of Cu-Cy is mainly accelerated by a heterogeneous process. Furthermore, the color change from pink to colorless in the presence of Cu-Cy suggests the RhB degradation, whereas no such visible color change was observed after adding $CuCl_2.2H_2O$ (Figure 4.2c). For comparison, Figure 4.2d was plotted. Remarkably, Cu-Cy NPs were ~7-fold more effective in degrading RhB than their raw material $CuCl_2.2H_2O$ as Cu^+ is much more reactive than Cu^{2+} toward the activation of H_2O_2 [57].

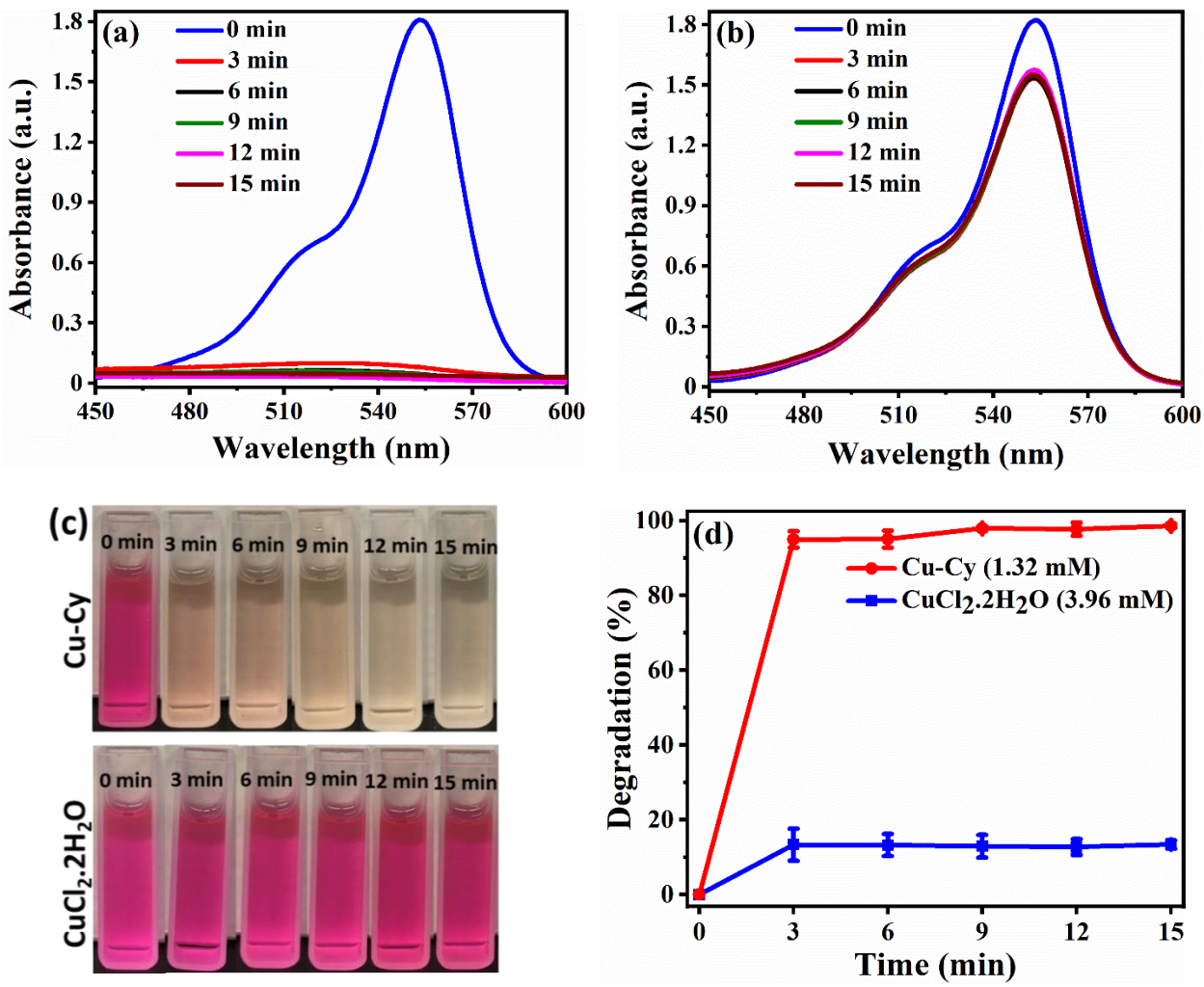

Figure 4.2. (a) Time-dependent UV-vis absorption spectra of RhB with Cu-Cy and H_2O_2. (b) Time-dependent UV-vis absorption spectra of RhB with $CuCl_2.2H_2O$ and H_2O_2. (c) Representative images of RhB solutions at different time in the presence of Cu-Cy + H_2O_2 (top) and $CuCl_2.2H_2O$ + H_2O_2 (bottom), and (d) comparison of degradation performance of Cu-Cy with $CuCl_2.2H_2O$. Reaction conditions: $[RhB]_0$ = 24 mg/L, $[Cu\text{-}Cy]_0$ = 0.5 mg/mL (1.32 mM), $[CuCl_2.2H_2O]_0$ = 3.96 mM, and $[H_2O_2]_0$ = 50 mM.

4.3.2.1. Effect of operational parameters on RhB degradation

4.3.2.1.1. Effect of initial concentration of RhB on the RhB degradation

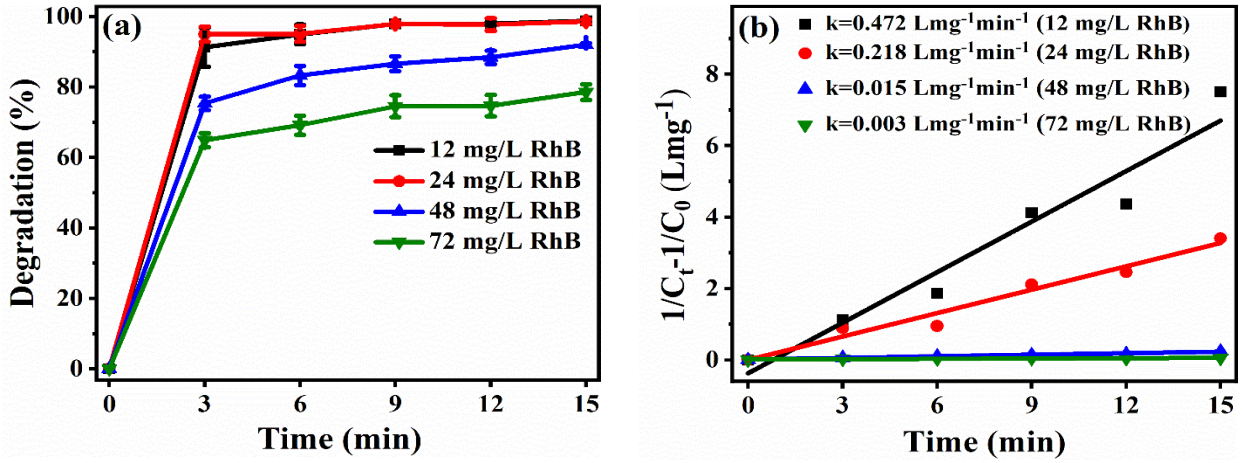

Figure 4.3. (a) Effect of the initial concentration of RhB on the RhB degradation. (b) Second-order reaction kinetics for degradation of different concentrations of RhB. Reaction conditions: $[Cu\text{-}Cy]_0$ = 0.5 mg/mL and $[H_2O_2]_0$ = 50 mM. The data in Figure 4.3b represent the average value of three experiments.

It is crucial to investigate the dependence of the degradation rate on the dye concentration both from a mechanistic and from an application perspective. The influence of the initial concentration of RhB on the rate of dye degradation was performed by changing the concentration of RhB from 12 mg/L to 72 mg/L with constant Cu-Cy (0.5 mg/mL) and H_2O_2 (50 mM). Figure 4.3a reveals that the degradation rate is related to the initial RhB concentration. It was found that the degradation percentage decreased with the increase in RhB concentration. The decrease in degradation rate with an increase in dye concentration could be due to the blocking of active sites on the Cu-Cy surface by the dye molecules [174, 175].

The catalytic degradation kinetics of RhB was probed using the first- and second-order rate equations (Eqs. (4.4) and (4.5), respectively) [73, 176, 177].

$$\ln (C_0/C_t) = k_1 t \quad (4.4)$$

$$1/C_t - 1/C_0 = k_2 t \quad (4.5)$$

where C_0 is the initial RhB concentration, C_t represents the RhB concentration after time t, k_1 is the first-order rate constant, k_2 is the second-order rate constant, and t is reaction time. Both reaction kinetics were tested, but first-order kinetics deviated much from linearity compared with second-order reaction kinetics, signifying the degradation reaction follows the second-order kinetics with respect to the RhB concentration. As the slope of the plot of $(1/C_t - 1/C_0)$ vs. time (t) gives the second-order rate constant, it was found that the increase in dye concentration decreased the rate constant (Figure 4.3b).

4.3.2.1.2. Effect of Cu-Cy concentration on the degradation of RhB

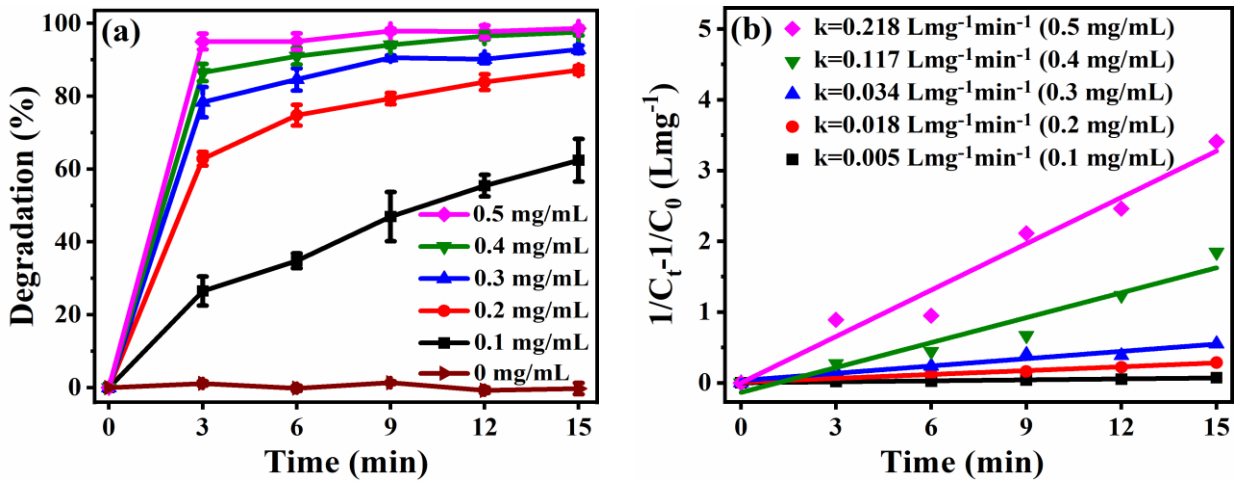

Figure 4. 4. (a) Effect of various concentrations of Cu-Cy on the degradation of RhB. (b) Second-order reaction kinetics for degradation of RhB with respect to Cu-Cy concentration. Reaction conditions: $[RhB]_0$ = 24 mg/L and $[H_2O_2]_0$ = 50 mM. The data in Figure 4.4b represent the average value of three experiments.

Five different dosages of Cu-Cy (0.1-0.5 mg/mL) were used to determine the optimum catalyst concentration. As presented in Figure 4.4a, the degradation of RhB enhanced with the increase in catalyst dosage, which can be attributed to the increase in the availability of active sites

on the Cu-Cy surface for reaction with H_2O_2 to produce more ROS [174, 175, 178]. Catalyst dosage of 0.5 mg/mL gave a slightly better efficiency than 0.4 mg/mL and, therefore, 0.5 mg/mL of Cu-Cy was used for the later studies. It was found that all the degradation rate constants under various Cu-Cy concentrations were followed by second-order kinetics (Figure 4.4b).

4.3.2.1.3. Effect of H_2O_2 concentration on the RhB degradation

In order to determine the optimum H_2O_2 concentration giving the maximum degradation efficiency, a detailed investigation in a broad H_2O_2 concentration was conducted by keeping other parameters constant. As can be seen in Figure 4.5, the catalytic degradation strongly depended on the initial H_2O_2 concentration, and the degradation rate increased while increasing the dose of H_2O_2 up to 50 mM. The increase in degradation after increasing the H_2O_2 amount is ascribed to the enhancement in the •OH concentration to attack the aromatic rings. However, when the concentration of H_2O_2 was further increased to 60 mM, the degradation of RhB slightly reduced up to 6 min and then remained almost the same as that of 50 mM of H_2O_2. This phenomenon is explained by the scavenging effect of excess H_2O_2, thereby decreasing the number of •OH in the reaction system (Eqs. (4.6) and (4.7)) [178-180]. Furthermore, the radical-radical reaction leads to more consumption of •OH (Eq. (4.8)) [178, 179]. Accordingly, selecting the optimized dose of H_2O_2 is crucial for practical applications from the considerations of the scavenging effect of H_2O_2 and the cost of H_2O_2. Therefore, the dose of 50 mM was taken as an optimum dose for throughout the experiments.

$$H_2O_2 + \bullet OH \rightarrow H_2O + \bullet HO_2 \ (k = 2.7 \times 10^7\ M^{-1}s^{-1}) \quad (4.6)$$

$$\bullet HO_2 + \bullet OH \rightarrow O_2 + H_2O \ (k = 6.6 \times 10^9\ M^{-1}s^{-1}) \quad (4.7)$$

$$\bullet OH + \bullet OH \rightarrow H_2O_2 \ (k = 5.5 \times 10^9\ M^{-1}s^{-1}) \quad (4.8)$$

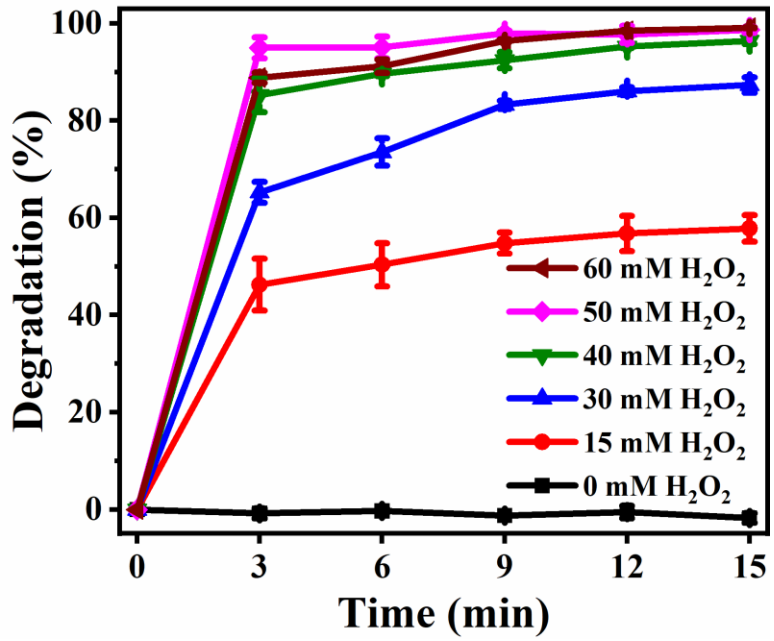

Figure 4.5. Effect of various concentrations of H_2O_2 on the degradation of RhB (24 mg/L) in the presence of Cu-Cy (0.5 mg/mL).

4.3.2.2. Effect of naturally occurring ions on the catalytic activity of Cu-Cy

It is worthwhile investigating the effect of dissolved ions on the rate and extent of degradation of industrial effluents as real wastewater and natural water contain various ions [180]. In order to elucidate the effects of various ions on the degradation of RhB, a final concentration of 1 mg/mL of sodium salt containing chloride, nitrate, sulfate, carbonate, or phosphate was added to the reaction solution. As displayed in Figure 4.6, all of the investigated ions inhibited the degradation percentage of RhB to various extent. SO_4^{2-} and NO_3^- had comparable percent degradation, while Cl^- had a slightly higher inhibition effect on the degradation of RhB. Cl^- has been reported as a scavenger of •OH, thereby negatively affecting the RhB degradation (Eqs. (4.9) and (4.10)) [181, 182]. Similarly, the inhibitive effect of SO_4^{2-} and NO_3^- can be attributed to the scavenging effect of these ions to •OH as shown in Eqs. (4.11) and (4.12), respectively [181, 182].

PO_4^{3-} and CO_3^{2-} inhibited the degradation efficiency of RhB significantly when compared to other ions, which can be explained as follows. Firstly, PO_4^{3-} and CO_3^{2-} are scavengers of •OH as depicted in Eqs. (4.13) and (4.14), respectively [143, 182]. Secondly, a higher pH can lead to the decomposition of H_2O_2 to water and oxygen, rather than the formation of •OH [153] as PO_4^{3-} and CO_3^{2-} can increase the pH of the solution [143]. Thirdly, the activity of •OH decreases remarkably in alkaline solution [182]. Fourthly, the scavenging role of H_2O_2 toward •OH increases at alkaline circumstances [153]. Lastly, alkaline conditions may make Cu-Cy unstable and unreactive.

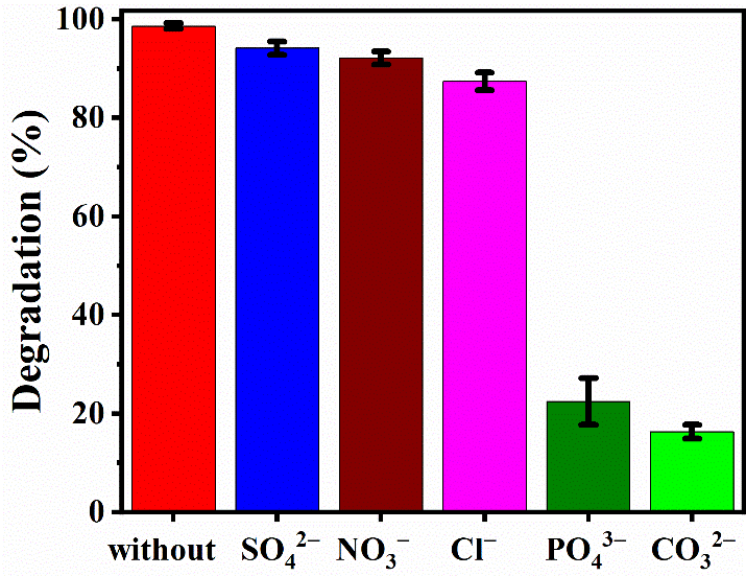

Figure 4.6. Effect of different anions on the degradation of RhB. Reaction conditions: $[RhB]_0$ = 24 mg/L, $[H_2O_2]_0$ = 50 mM, $[Cu\text{-}Cy]_0$ = 0.5 mg/mL, and $[NaCl]_0$ = $[NaNO_3]_0$ = $[Na_2SO_4]_0$ = $[Na_2CO_3]_0$ = $[Na_3PO_4]_0$ = 1 mg/mL.

$$Cl^- + \bullet OH \rightarrow HOCl^{\bullet -} \quad (4.9)$$

$$HOCl^{\bullet -} + Cl^- \rightarrow OH^- + Cl_2^{\bullet -} \quad (4.10)$$

$$SO_4^{2-} + \bullet OH \rightarrow OH^- + SO_4^{\bullet -} \quad (4.11)$$

$$NO_3^- + \bullet OH \rightarrow OH^- + NO_3^{\bullet} \quad (4.12)$$

$$PO_4^{3-} + \bullet OH \rightarrow PO_4^{\bullet 2-} + OH^- \quad (4.13)$$

$$CO_3^{2-} + \bullet OH \rightarrow CO3^{\bullet -} + OH^- \quad (4.14)$$

4.3.2.3. Effect of •OH quencher on the degradation of RhB

In order to test whether •OH was produced in the reaction system, methanol (a well-known quencher of •OH [143, 183]) was mixed to the reaction system. The addition of methanol remarkably reduced the degradation of RhB (Figure 4.7), confirming the production of •OH. To further ensure that •OH was the main ROS responsible for degrading RhB, an excessive amount of methanol (310 mM) was used to scavenge all possible •OH that was generated in the reaction system. As expected, the large amount of methanol almost inhibited the degradation of RhB (Figure 4.7). Accordingly, it is reasonable to claim that the dominant ROS produced by the reaction system is •OH.

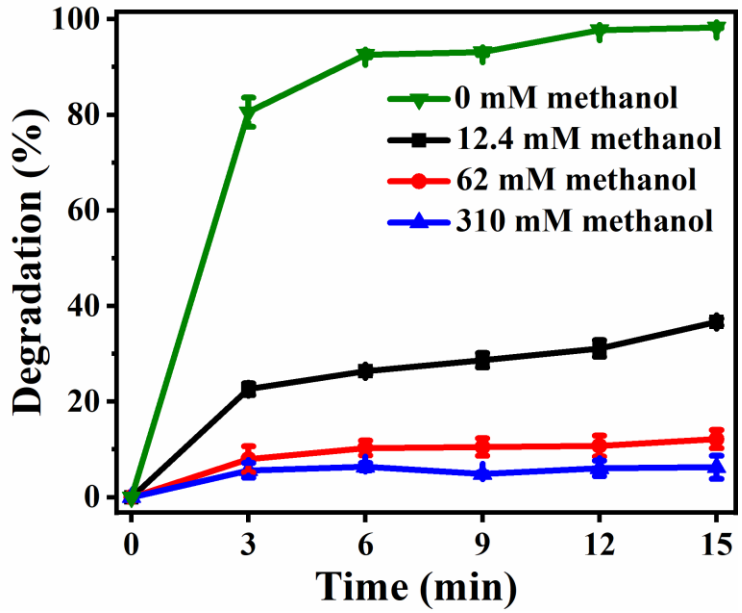

Figure 4.7. Effect of •OH scavenger on the RhB degradation (24 mg/L) in the presence of Cu-Cy (0.5 mg/mL) and H_2O_2 (50 mM).

4.3.2.4. Confirmation of •OH production using PL technique

The involvement of •OH in the degradation of the organic pollutants was further corroborated by the PL method using coumarin as a tracking molecule. Coumarin is a weakly fluorescent molecule that produces the strongly fluorescent molecule, 7-hydroxycoumarin (umbelliferone), with •OH as depicted in Scheme 4.1 [7, 112].

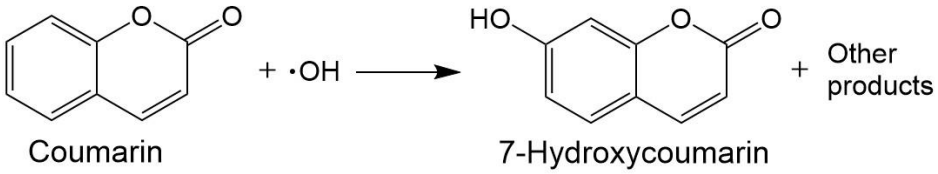

Scheme 4.1. Generation of 7-hydroxycoumarin as a result of the reaction between coumarin and •OH.

The plot of the PL intensity of 7-hydroxycoumarin at 452 nm against reaction time (Figure 4.8a) demonstrates that Cu-Cy + H_2O_2 enhanced the PL intensity at 452 nm remarkably as compared to Cu-Cy alone or H_2O_2 alone, suggesting the Cu-Cy + H_2O_2 produced a significant amount of •OH in the reaction system. In contrast, after using RhB, the PL intensity of Cu-Cy + H_2O_2 + RhB was noticeably reduced because some of •OH was used to degrade RhB. Figure 4.8b shows the representative PL spectra of generated 7-hydroxycoumarin after 15 min of reaction time at different conditions.

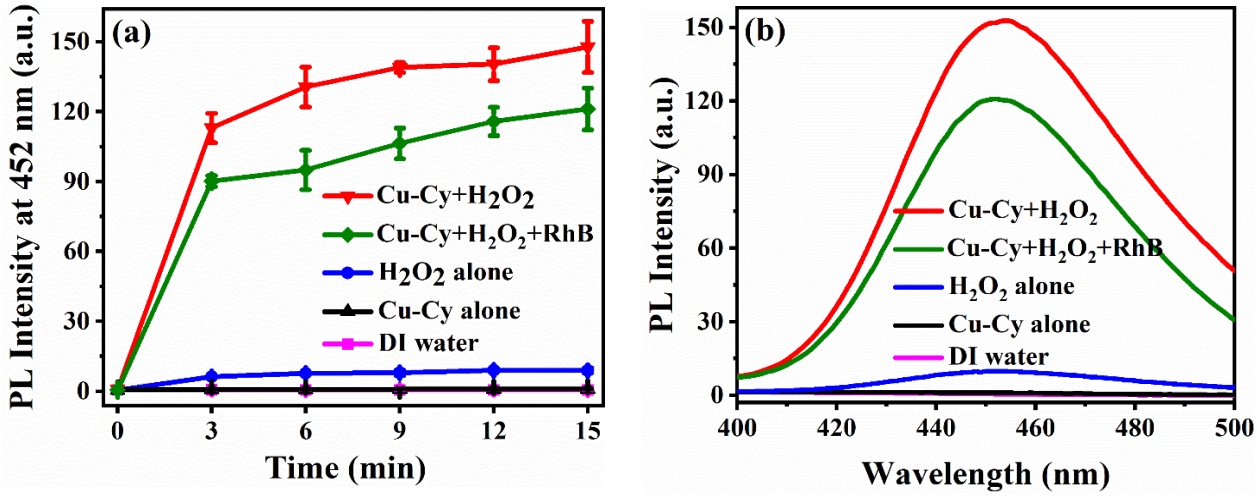

Figure 4.8. (a) Plot of the PL intensity of 7-hydroxycoumarin at 452 nm as a function of time. (b) The PL spectra of generated 7-hydroxycoumarin monitored after 15 min of reaction time under various conditions. The increase in the PL intensity at 452 nm demonstrates the generation of •OH.

4.3.3. Degradation study of methylene blue (MB)

To evaluate the versatility of Cu-Cy NPs, the catalytic behavior was also explored for the catalytic oxidation of MB. The control experiments conducted in the presence of Cu-Cy alone and H_2O_2 alone exhibited very little to no MB degradation (Figure S4.2). In contrast, a markedly

synergistic effect of Cu-Cy and H_2O_2 was observed, degrading more than 98% of MB within 6 min. The representative absorption spectra of MB (12 mg/L) as a function of reaction time up to 15 min with Cu-Cy (0.5 mg/mL) and H_2O_2 (50 mM) are displayed in Figure 4.9a. Additionally, Figure S4.3a depicts that degradation rate is related to dye concentration. Furthermore, R^2 values for second-order kinetics were found to be greater than that of first-order kinetics, showing that catalytic degradation of MB proceeds via second-order kinetics with regards to MB concentration (Figure S4.3b).

We also compared the catalytic activity of Cu-Cy with $CuCl_2.2H_2O$. As shown in Figure 4.9b, the degradation of MB with $CuCl_2.2H_2O$ (3.96 mM, which is equivalent to the Cu amount in Cu-Cy) is slow, in which only ~20% of degradation was seen after 15 min of reaction. The color of the solution turned from blue to colorless in the presence of Cu-Cy owing to MB degradation. However, no such visible color change was observed with $CuCl_2.2H_2O$ (Figure 4.9c). For comparison, Figure 4.9d was plotted.

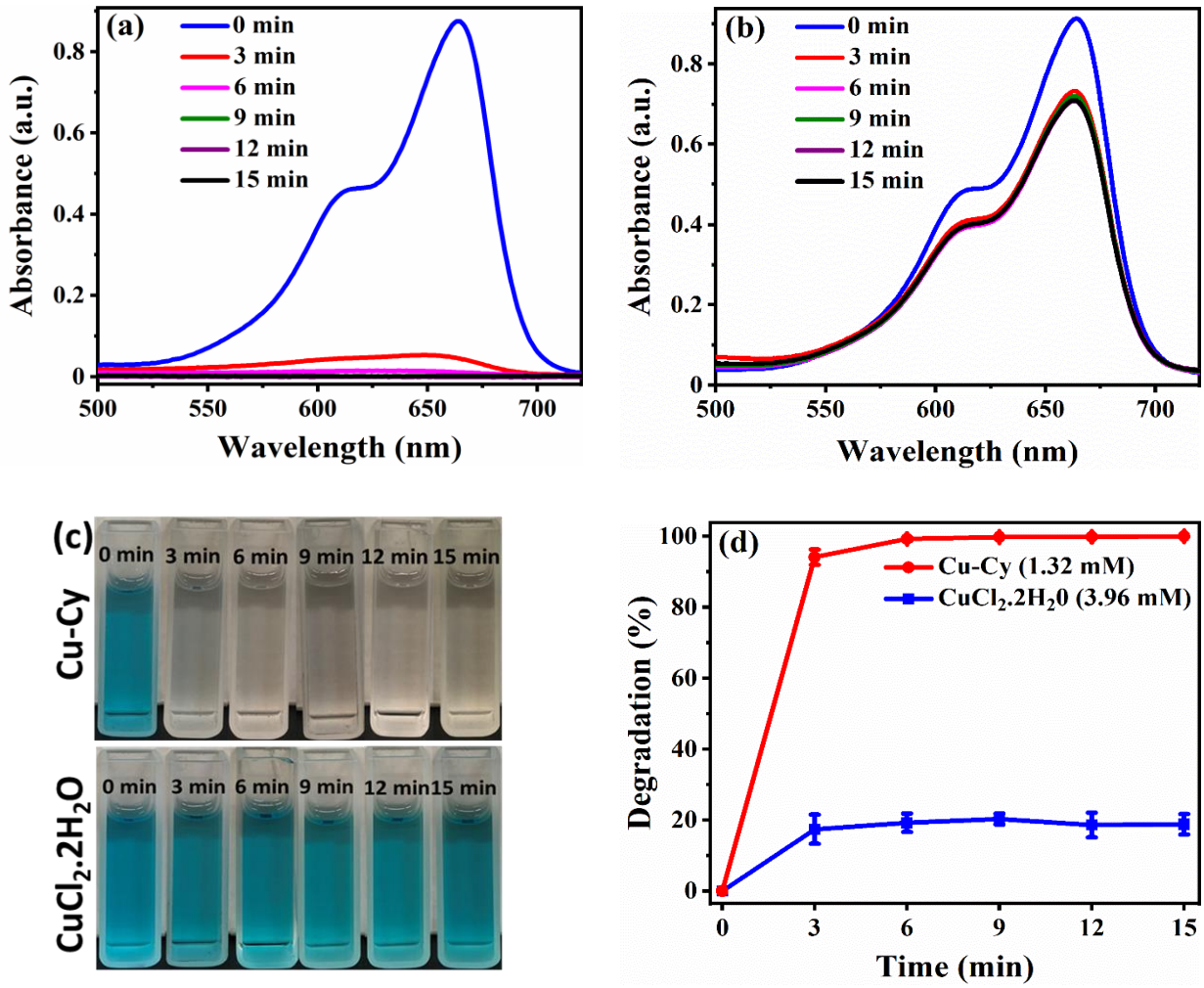

Figure 4.9. (a) Time-dependent UV-vis absorption spectra of MB with Cu-Cy and H_2O_2. (b) Time-dependent UV-vis absorption spectra of MB with $CuCl_2.2H_2O$ and H_2O_2. (c) Representative images of MB solutions with different reaction time in the presence of Cu-Cy + H_2O_2 (top) and $CuCl_2.2H_2O$ + H_2O_2 (bottom), and (d) comparison of degradation performance of Cu-Cy with $CuCl_2.2H_2O$. Reaction conditions: $[MB]_0$ = 12 mg/L, $[Cu\text{-}Cy]_0$ = 0.5 mg/mL (1.32 mM), $[CuCl_2.2H_2O]_0$ = 3.96 mM, and $[H_2O_2]_0$ = 50 mM.

Although it may not be fully reasonable to compare our results with the reported results in the literature due to differences in experimental conditions, some results of the previous works and the system proposed in this work are compared in Table 4.1. As seen in Table 4.1, the degradation efficiencies of Cu-Cy are comparable to most of the heterogeneous catalysts.

Table 4.1. Comparison of RhB and MB removal efficiencies (%) of Cu-Cy with various heterogeneous catalysts.

S.No.	Catalyst	Dye Amount (mg/L)	Operation Time (min)	H_2O_2 Amount (mM)	Catalyst Amount (mg/mL)	Removal Efficiency (%)	Ref.
1.	Fe_3O_4 (S1)	4.79 at 55°C (RhB)	120	40	0.5	97.8	[177]
2.	Fe_3O_4 (S1)	3.2 at 55°C (MB)	120	40	0.5	80	[177]
3.	$5Cu/Al_2O_3$-750	10 at 50°C (RhB)	30	29.4	1	98.53	[179]
4.	$LaTi_{0.4}Cu_{0.6}O_3$	8 (RhB)	120	20	1.4	~ 94	[184]
5.	$BiFeO_3$ MNPs	4.79 (RhB)	90	10	0.5	95.2	[185]
6.	$BiFeO_3$ MNPs	6.4 (MB)	150[a]	10	0.5	79.5	[185]
7.	Au/ZnO	14.25 (MB)	120	490	1	90	[186]
8.	$Fe_3O_4/FeMnO_X$	23.13 (MB)	240	735	0.5	~90	[187]
9.	FeCeOx	100 at 35°C (RhB)	150	80	1.5	~98	[188]
10.	CuO-MeOH	8.33 (MB)	240	1633.33	0.17	~100	[189]
11.	Plate-like CuO	8.33 (MB)	600	1633.33	0.17	97.2	[190]
12.	Cu-Cy	24 (RhB)	15	50	0.5	~99	This work
13.	Cu-Cy	12 (MB)	15	50	0.5	~100	This work

[a] estimated from the figure.

4.3.4. Effect of microwave (MW) irradiation on the degradation of RhB

MWs are electromagnetic radiations with frequencies ranging from 0.3 GHz to 300 GHz. MW-irradiated Fenton/Fenton-like catalysts exhibit a stronger oxidation performance with high catalytic efficiency and short reaction time when compared to nonirradiated catalysts [6, 56, 163]. The above experiments showed that Cu-Cy can degrade organic pollutants with the assistance of H_2O_2. However, one of the disadvantages of the above process is that a higher concentration of H_2O_2 is required to achieve sufficient removal efficiency. An excess amount of H_2O_2 is not recommended as the residual H_2O_2 contributes to chemical oxygen demand (COD) [180]. Also, the use of H_2O_2 in large quantities is harmful to many microorganisms [180]. Another adverse effect of H_2O_2, if present in large amounts, is that it acts as a quencher of •OH [178-180]. Additionally, excessive H_2O_2 corrodes equipment, thereby increasing the operating costs [191]. Therefore, the use of H_2O_2 alone is not a good strategy. Instead, H_2O_2 should be used in combination with other external energies, such as UV/visible light, heat, electricity, ultrasound, and MWs. Among them, MW-assisted Fenton reaction is a more attractive and promising method to degrade organic pollutants [56]. Due to the thermal and non-thermal effects of MWs, MWs have played a vital role in wastewater treatment [60, 152].

In this contribution, we investigated the oxidative degradation of RhB and 4-NP by Cu-Cy NPs with H_2O_2 as an oxidizing agent in the presence of low-power MW exposure. The effects of MW power, Cu-Cy concentration, initial RhB concentration, and applied H_2O_2 dose have been investigated to determine optimum conditions to degrade RhB.

4.3.4.1. Effect of MW power on the degradation of RhB

In order to explore the influence of MW power on RhB degradation, a series of experiments were conducted at different MW powers (2, 10, and 20 W). As depicted in Figure 4.10a, the highest degradation activity was obtained at 20 W of MW radiation. Accordingly, 20 W of MW was chosen for further experiments. Moreover, it was confirmed that MW alone had no noticeable effect on the degradation of RhB (Figure S4.4).

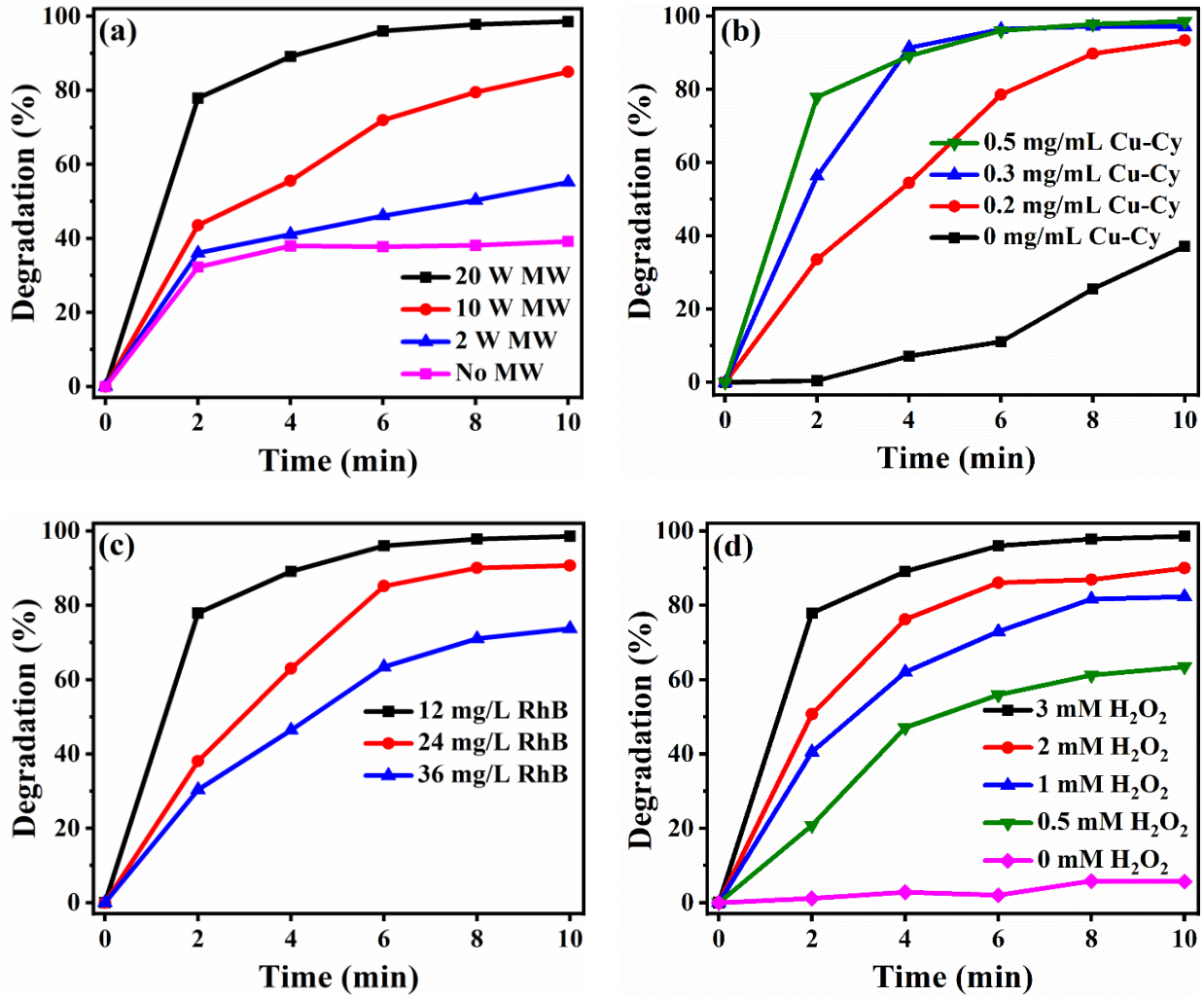

Figure 4.10. (a) Effect of various MW powers on the degradation of RhB (12 mg/L) with Cu-Cy (0.5 mg/mL) and H_2O_2 (3 mM). (b) Effect of various concentrations of Cu-Cy on the degradation of RhB (12 mg/L) under 20 W of MW exposure with 3 mM of H_2O_2. (c) Effect of the initial concentration of RhB on the degradation of RhB under 20 W of MW exposure with Cu-Cy (0.5 mg/mL) and H_2O_2 (3 mM). (d) Effect of various concentrations of H_2O_2 on the degradation of RhB (12 mg/L) under 20 W of MW exposure with Cu-Cy (0.5 mg/mL).

4.3.4.2. Effect of catalyst on the RhB degradation

In order to explore the effect of the dosage of the catalyst, experiments were conducted with different masses of Cu-Cy (0-0.5 mg/mL). As displayed in Figure 4.10b, the higher catalyst dosage increased the degradation of RhB, which can be ascribed to increase in the availability of active sites on Cu-Cy's surface [174, 175, 178]. Catalyst dosages of 0.3 and 0.5 mg/mL resulted in almost similar performances, and 0.5 mg/mL of Cu-Cy was taken for further studies.

4.3.4.3. Effect of dye concentration on the RhB degradation

Experiments were conducted to further study the influence of the initial concentration of RhB on the rate of dye degradation by changing the initial concentration of RhB from 12 to 36 mg/L with constant Cu-Cy (0.5 mg/mL) and H_2O_2 (3 mM) under 20 W of MW exposure. As displayed in Figure 4.10c, the degradation rate of RhB decreased with the increase in dye concentration. This might be due to the fact that the increase in the dye concentration resulted in an increase in dye molecules but not the number of •OH. Also, active sites of Cu-Cy could be covered by dye molecules, thereby decreasing degradation efficiency with an increase in dye concentration [174, 175].

4.3.4.4. Effect of H_2O_2 concentration on the degradation of RhB

We conducted a detailed investigation in a broad H_2O_2 concentration to determine the optimum H_2O_2 concentration. As shown in Figure 4.10d, the degradation strongly depended on the initial H_2O_2 concentration, and the degradation rate was enhanced with the increase in H_2O_2 amount. The increase in degradation after increasing H_2O_2 concentration is due to the enhancement in the generation of •OH.

Additionally, to determine the reaction order for the degradation of RhB at the optimum reaction conditions, we examined both first-order and second-order reaction kinetics. As illustrated in Figure S4.5, the second-order model gave a better fit, thereby suggesting the degradation reaction followed the second-order kinetics, and the second-order rate constant was determined to be 0.217 $Lmg^{-1}min^{-1}$ (Figure S4.5b).

4.3.5. Effect of MW radiation on the degradation of 4-nitrophenol (4-NP)

The above findings demonstrated that Cu-Cy, with the assistance of a low amount of H_2O_2, can degrade RhB when excited by MW. These results further inspired us to investigate the catalytic performances of Cu-Cy on the degradation of 4-NP.

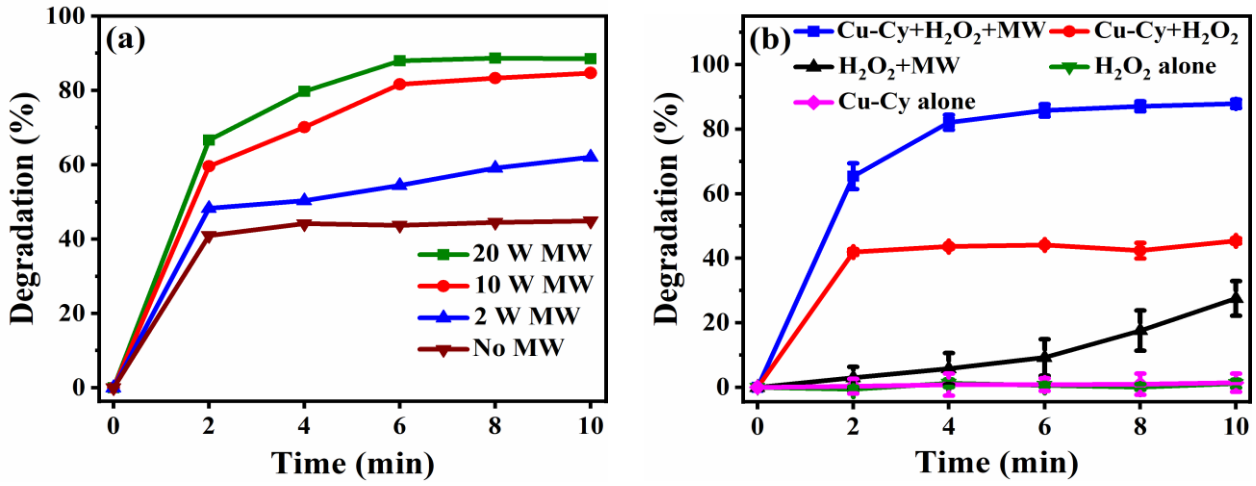

Figure 4.11. (a) Effect of various MW power on the oxidative degradation of 4-NP (30 mg/L) with Cu-Cy (0.5 mg/mL) and H_2O_2 (10 mM). (b) Comparison of 4-NP (30 mg/L) degradation under various conditions. Reaction conditions: $[Cu\text{-}Cy]_0$ = 0.5 mg/mL (if used), $[H_2O_2]_0$ = 10 mM (if used), and MW power = 20 W (if used).

The absorption spectrum of the aqueous 4-NP solution showed two bands at ~318 nm and ~400 nm (Figure S4.6), as discussed in the literature [192]. The absorption peak of 4-NP at ~318 nm did not change noticeably upon MW irradiation, although there was a slight increase in

intensity at ~400 nm due to the formation of p-nitrophenolate ions (Figure S4.6). It should be noted that the addition of Cu-Cy alone to 4-NP solution resulted in a decrease in the intensity of the former band (~318 nm) but an increase of the later band (~400 nm) (Figure S4.7). On the contrary, both the absorption peaks rapidly decreased in the presence of Cu-Cy and H_2O_2 when excited by MW (Figure S4.7), indicating oxidative degradation of 4-NP. Interestingly, the 4-NP degradation happened in a relatively short time, thereby providing a novel strategy for environmental remediation.

As displayed in Figure 4.11a, the degradation rate of 4-NP was strongly dependent on the MW dose. The degradation efficiency of 4-NP increased after increasing the MW dose (Figure 4.11a), which means a higher MW dose has a positive effect on the oxidative degradation of 4-NP. Figure 4.11b displays the comparison of the degradation of 4-NP under various conditions. Taken together, these results demonstrate that the activity of Cu-Cy/H_2O_2 on the degradation of 4-NP can be increased by MW irradiation. According to the R^2 values, oxidative degradation of 4-NP followed the second-order kinetics rather than the first-order kinetics (Figure S4.8).

4.3.6. Radical trapping experiments and degradation mechanism

To elucidate the reaction mechanism of MW assisted Fenton-like reaction and identify the ROS that played a major role in the reaction system, radical scavenging experiments were conducted using tert-butanol (TBA) and chloroform as •OH [143, 183, 193] and $\bullet O_2^-$ scavengers, respectively [35, 143, 147].

To evaluate whether •OH was produced in the reaction system, we added various TBA concentrations to the reaction system. The addition of TBA significantly reduced the degradation of RhB (Figure 4.12a), which confirms the generation of •OH. Interestingly, an excess amount of

TBA (81 mM) almost inhibited the degradation of RhB, signifying that although other ROS could have some contributions toward the degradation of pollutants, •OH is the important ROS during the catalytic degradation reaction.

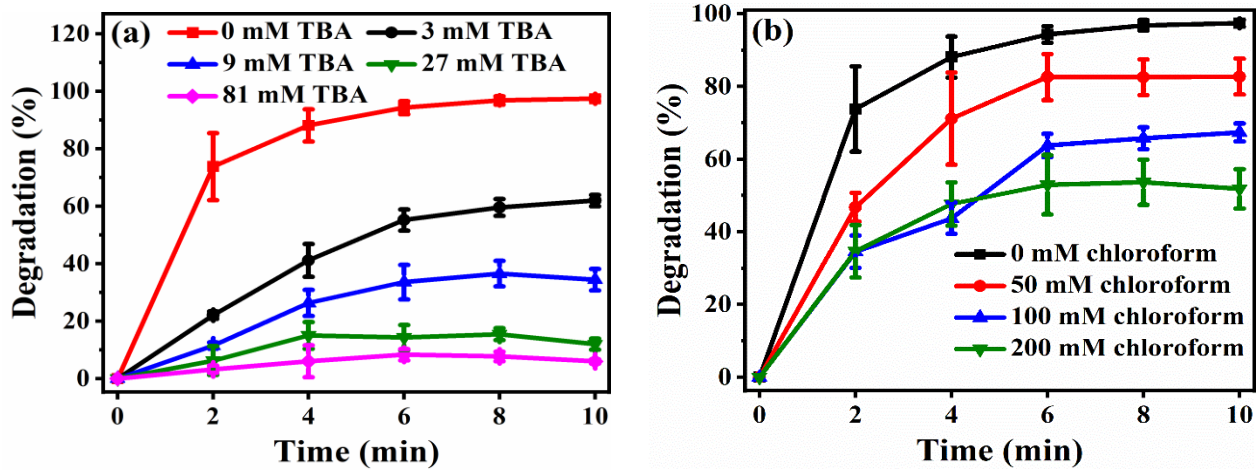

Figure 4.12. Effect of (a) TBA and (b) chloroform on the degradation of RhB (12 mg/L) upon 20 W of MW irradiation with Cu-Cy (0.5 mg/mL) and H_2O_2 (3 mM).

In order to further identify whether the reaction system could produce $•O_2^-$, we performed a series of experiments after adding the various amounts of chloroform. As can be seen in Figure 4.12b, the degradation gradually decreased with the increase in chloroform concentration. The results indicated that the reaction system could produce $•O_2^-$. Moreover, it was confirmed that TBA alone (81 mM) and chloroform alone (200 mM) had no noticeable effect on the degradation of RhB (Figure S4.9).

The production of $•O_2^-$ and a significant decrease in RhB degradation with the excess amount of TBA indicated that most of $•O_2^-$ radicals could be generated by Eq. (4.15).

$$H_2O_2 + •OH \rightarrow •O_2^- + H_2O + H^+ \quad (4.15)$$

As produced $\bullet O_2^-$ may also react with H_2O_2 to regenerate •OH (Eq. (4.16)) [187] because $\bullet O_2^-$ is the precursor of most of the ROS [144].

$$H_2O_2 + \bullet O_2^- \rightarrow \bullet OH + O_2 + OH^- \quad (4.16)$$

Indeed, radical reactions are very complicated, involving various parallel and consecutive reactions. ROS may be generated through at least three pathways: (i) self-decomposition of H_2O_2 could occur upon MW irradiation as presented in Eq. (4.17) [6, 56],

$$H_2O_2 + MW \rightarrow 2\bullet OH \quad (4.17)$$

(ii) H_2O_2 decomposition could occur via heterogeneous Fenton-like process on Cu^+ sites [6, 56], and (iii) MW could efficiently accelerate the Cu^{2+}/Cu^+ redox cycles, similar to that of Fe^{3+}/Fe^{2+} [163, 194].

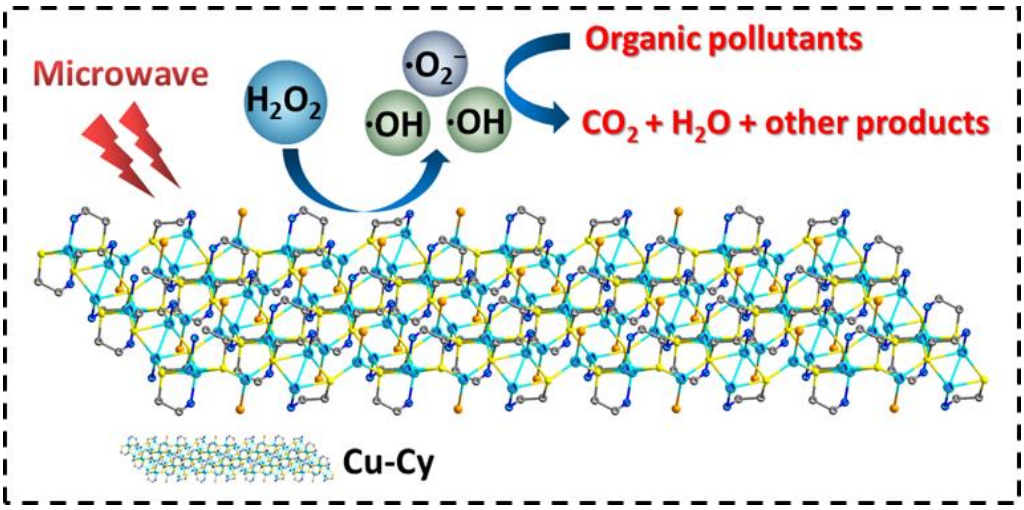

Figure 4.13. Proposed mechanism of catalytic degradation of organic pollutants using Cu-Cy with the assistance of H_2O_2 upon MW irradiation.

Based on the above discussion, a plausible catalytic mechanism of Cu-Cy for H_2O_2 activation and degradation of organic pollutants upon MW irradiation is schematically represented in Figure

4.13. Although many literatures have reported the MW-induced ROS generation, the detailed mechanism of ROS production upon MW is not clear yet and needs to be further explored.

4.3.7. Recycling Study of Cu-Cy

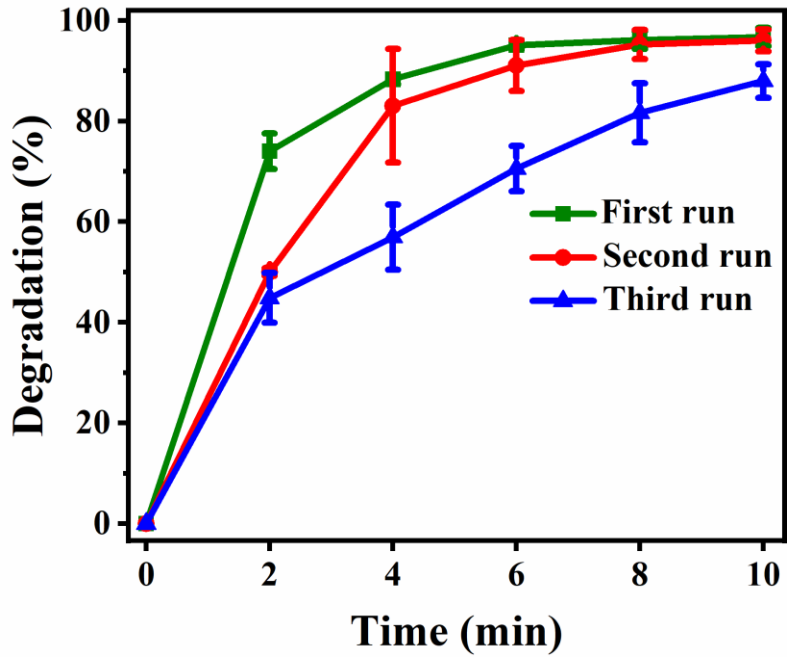

Figure 4.14. Recycling study of the Cu-Cy catalyst in the degradation of RhB (12 mg/L) upon 20 W of MW irradiation with Cu-Cy (0.5 mg/mL) and H_2O_2 (3 mM).

Recycling is one of the most important parameters for the practical applicability of a catalyst. We took RhB as an example to investigate the stability of Cu-Cy. For determining stability, the Cu-Cy catalyst was used up to three cycles under the same experimental conditions. After every cycle, the catalyst was recovered by centrifugation and used for the subsequent cycle. Figure 4.14 shows that Cu-Cy has good stability and reusability. The slight decrease in degradation efficiency in the third run was due to the loss of some mass during centrifugation, as certain catalyst loss is

unavoidable during the washing process. Additionally, Cu leaching from Cu-Cy may have some contribution to the slight decrease in degradation efficiency.

4.4. Conclusions

In conclusion, this work presents that Cu-Cy NPs can be used for the oxidative degradation of toxic organic contaminants for wastewater purification. The results of degradation of RhB, MB, and 4-NP established the strong catalytic performance of Cu-Cy NPs and revealed their utility for degrading a variety of toxic water pollutants in a relatively shorter time by a heterogenous Fenton-like reaction. The degradation pathway followed the second-order kinetics rather than the first-order kinetics. Moreover, the degradation activity of Cu-Cy enhanced when stimulated by MW irradiation. Radical quenching experiments showed that •OH was the dominant species for degrading pollutants. Additionally, recycling studies demonstrated that Cu-Cy has good stability and sustainability. This study offers a simple yet effective, robust, and economical catalyst ideal for the treatment of toxic and nonbiodegradable organic pollutants in wastewater. It is anticipated that the material is very likely a promising candidate in future applications of wastewater treatment.

Conflicts of interest

There are no conflicts to declare.

Supporting Information

Exploration of Copper-Cysteamine Nanoparticles as an Efficient Heterogeneous Fenton-Like Catalyst for Wastewater Treatment

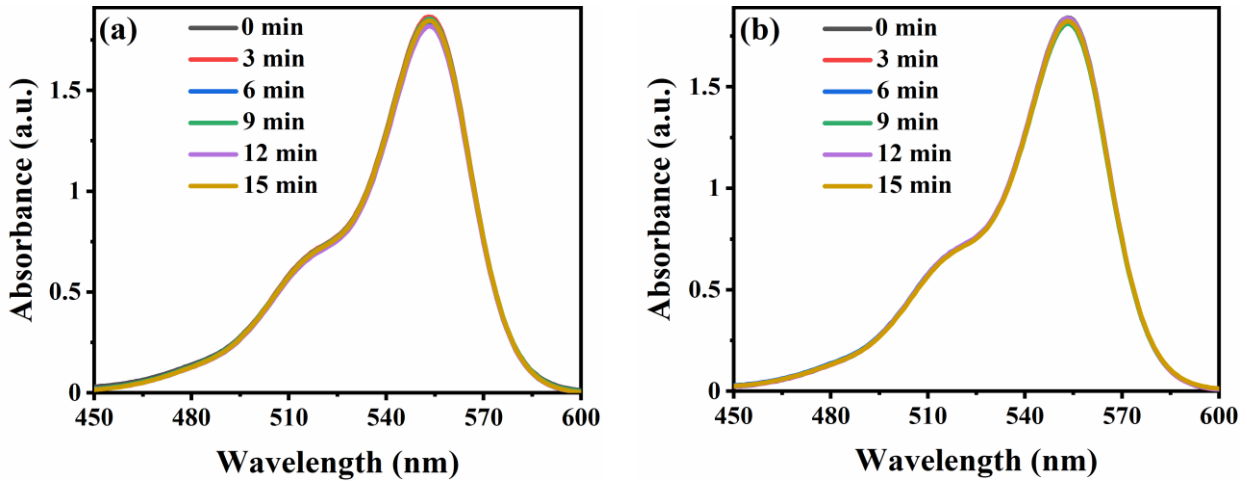

Figure S4.1. Representative time-dependent UV-vis absorption spectra of RhB (24 mg/L) in the presence of (a) Cu-Cy (0.5 mg/mL) alone and (b) H_2O_2 (50 mM) alone.

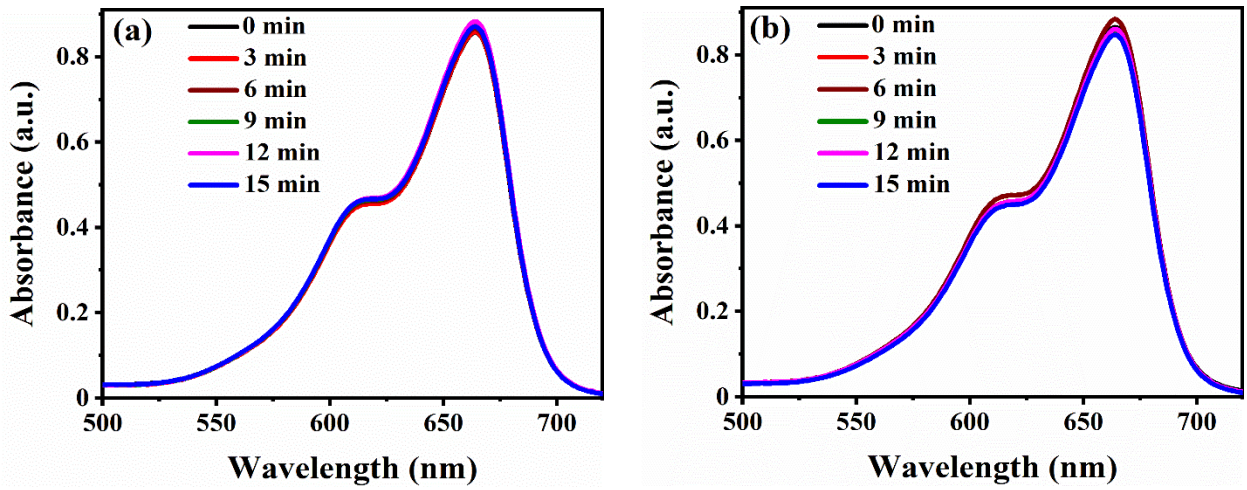

Figure S4.2. Representative time-dependent UV-vis absorption spectra of MB (12 mg/L) in the presence of (a) Cu-Cy (0.5 mg/mL) alone and (b) H_2O_2 (50 mM) alone.

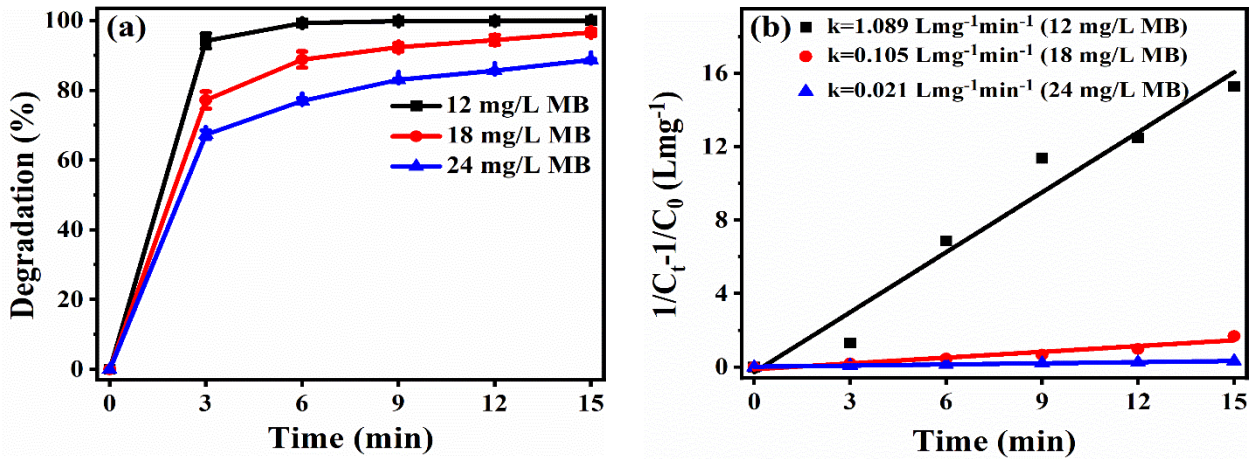

Figure S4.3. (a) Effect of MB concentration on the degradation of MB in the presence of Cu-Cy (0.5 mg/mL) and H_2O_2 (50 mM). (b) Second-order reaction kinetics for degradation of different concentrations of MB in the presence of Cu-Cy (0.5 mg/mL) and H_2O_2 (50 mM). The data in Figure S4.3b represent the average value of three experiments.

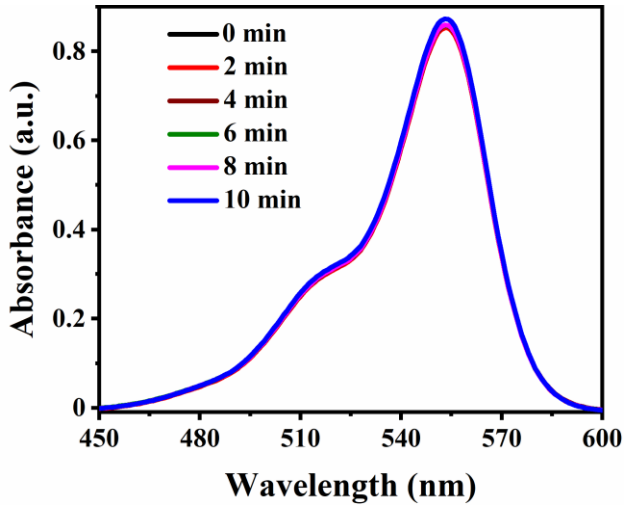

Figure S4.4. Representative time-dependent UV-vis absorption spectra of RhB (12 mg/L) upon 20 W of MW irradiation in the absence of Cu-Cy and H_2O_2.

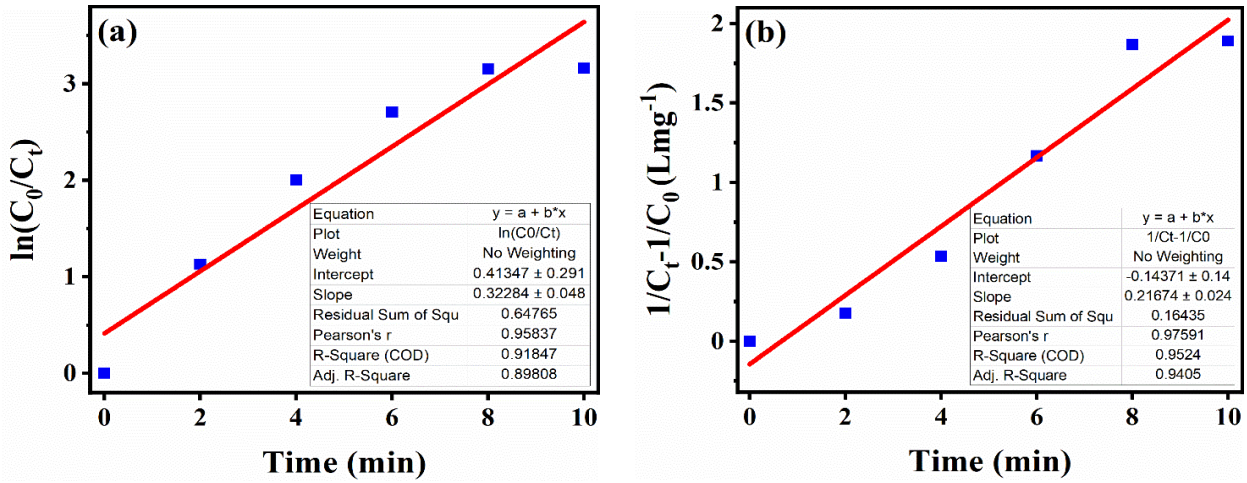

Figure S4.5. Plot of (a) first-order and (b) second-order kinetics for degradation of RhB (12 mg/L) in the presence of Cu-Cy (0.5 mg/mL) and H_2O_2 (3 mM) upon 20 W of MW irradiation. The data in each plot represent the average value of four experiments.

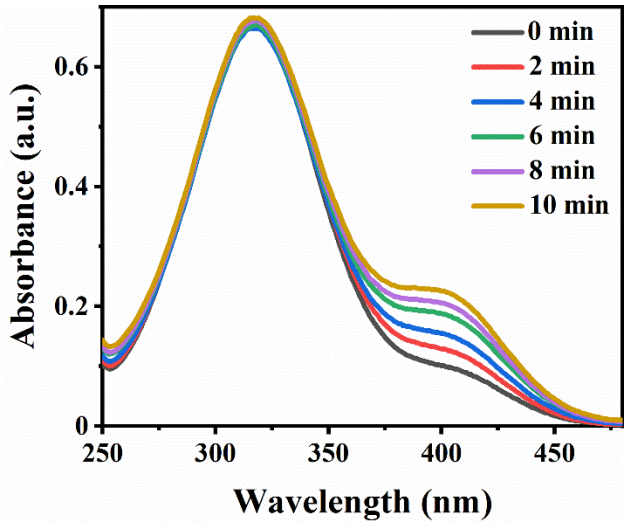

Figure S4.6. Representative time-dependent UV-vis absorption spectra of 4-NP (30 mg/L) upon 20 W of MW irradiation in the absence of Cu-Cy and H_2O_2.

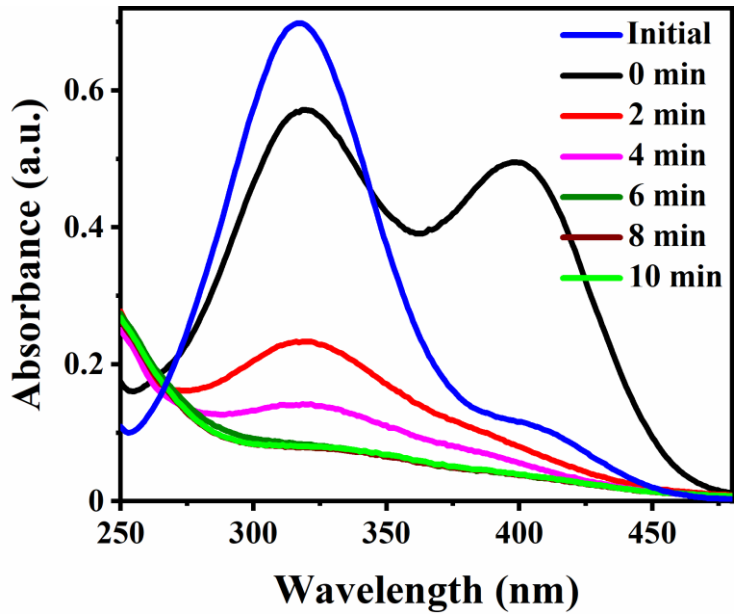

Figure S4.7. Representative time-dependent UV-vis absorption spectra of 4-NP (30 mg/L) upon 20 W of MW irradiation in the presence of Cu-Cy (0.5 mg/mL) and H_2O_2 (10 mM). Initial and 0 min indicate the absorption spectra of 4-NP measured before and after 30 min of adsorption/desorption equilibrium, respectively.

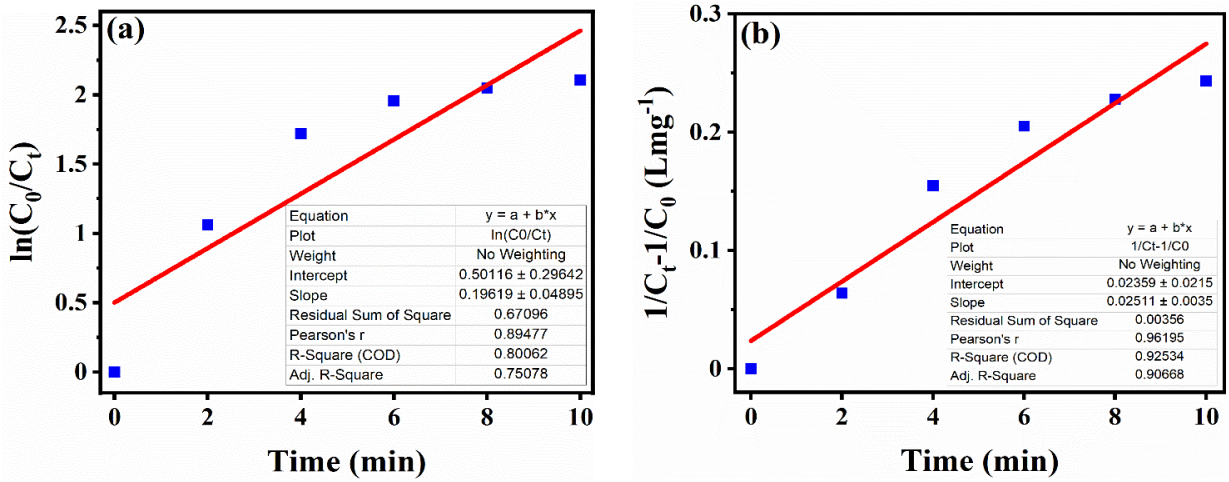

Figure S4.8. Plot of (a) first-order and (b) second-order kinetics for degradation of 4-NP (30 mg/L) in the presence of Cu-Cy (0.5 mg/mL) and H_2O_2 (10 mM) upon 20 W of MW irradiation. The data in each plot represent the average value of three experiments.

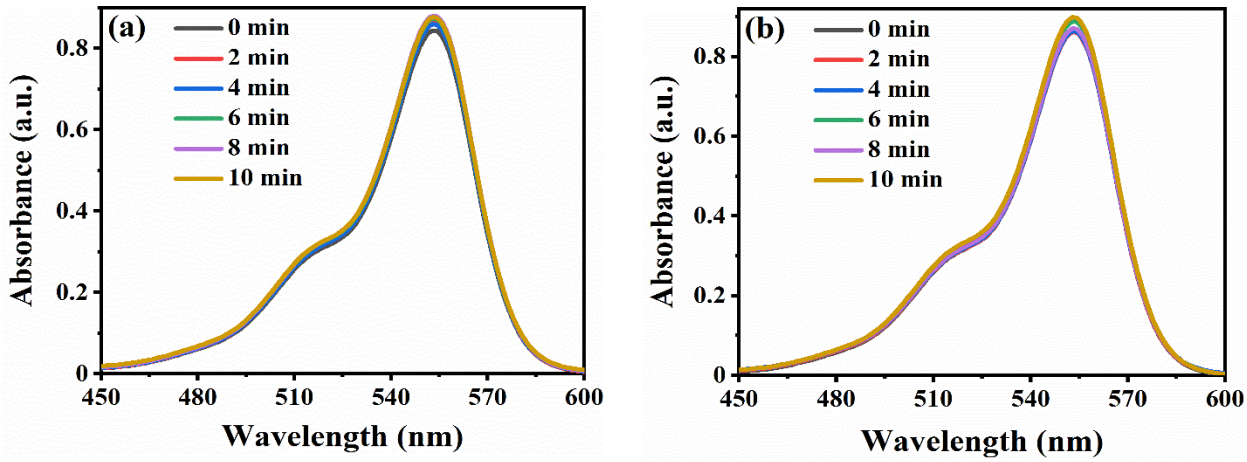

Figure S4.9. Representative time-dependent UV-vis absorption spectra of RhB (12 mg/L) in the presence of (a) 81 mM of tert-butanol (TBA) and (b) 200 mM of chloroform upon 20 W of MW irradiation.

Chapter 5

General Conclusions and Future Research Directions

In recent years, several methods have been explored for cancer treatment. One of the most widely investigated treatments is the ROS-mediated strategy as the majority of cancer cells contain more ROS, and cancer cells are more sensitive to the elevation of ROS level compared to normal cells. Among different ROS-based therapeutics, PDT has the potential to meet various currently unmet medical needs. However, the limited penetration depth of light and the hypoxic nature of solid tumors severely limits PDT's practicality in clinical settings. In addition, traditional PSs usually suffer from aggregation-caused fluorescence quenching and a significant decrease in ROS generation in aqueous solutions.

In the first part of the dissertation, a faster way of fabricating Cu-Cy nanoparticles was discussed. We utilized various characterization methods to confirm that the as-formed material was Cu-Cy. RNO bleaching assay was used to affirm that newly fabricated Cu-Cy can generate ROS upon UV and MW irradiations. Inhibition of RNO bleaching by DABCO, a well-known quencher of $^1O_2$, provided additional evidence of the $^1O_2$ production in the reaction system. Additionally, •OH generated by Cu-Cy under MW exposure was evaluated by the PL technique employing coumarin as a probe molecule. Notably, our findings demonstrated that newly made Cu-Cy is more effective for generating ROS and destroying cancerous cells than previously reported Cu-Cy. Our future work will concentrate on the synthesis of monodisperse Cu-Cy nanoparticles. Additionally, we will focus on the exploitation of active targeting to improve tumor accumulation *in vivo*.

In the second project, two MW-responsive AIEgens (**TPEPy-I** and **TPEPy-PF6**) were designed, and their ROS production and *in vitro* cancer cell killing capabilities upon MW exposure were investigated. Different methods were used to confirm that these AIEgens can produce ROS, including $^1O_2$, when excited by MW. The AIEgens showed significant toxicity upon MW exposure toward HeLa cells as evaluated by the MTT and live/dead assays. It is anticipated that these AIEgens are promising candidates for image-guided microwave dynamic therapy (MWDT). Overall, the capability of these two AIEgens to be stimulated by MW not only solves the issues of traditional PDT but also helps to improve conventional MW ablation therapy by decreasing the MW dose needed to achieve the same therapeutic outcome, thereby decreasing the occurrence of side-effects of MW irradiation.

Even though our preliminary results reveal that the proposed MWDT could overcome the main issues of conventional PDT, this method is just at the beginning, and it could have some problems for future translation from bench to bedside. Although MWs penetrate deeper than light (UV, visible, and NIR), they cannot penetrate as deep as ultrasound and X-rays. Accordingly, the applicability of MWs toward cancer treatment still can have some limitations regarding its depth. Another limitation of the present study is that the proposed method is not effective against metastatic lesions, which are the leading cause of cancer death. This problem could be solved by combining MWDT with chemotherapy or immunotherapy. Most of AIEgens, including **TPEPy-I** and **TPEPy-PF6**, possess high hydrophobicity, which severely limits their biological applications *in vivo*. Therefore, our future work will also concentrate on the utilization of drug delivery systems to load and deliver these AIEgens into the tumor.

The third part of the dissertation explored the oxidative degradation of organic pollutants using Cu-Cy nanoparticles as a heterogeneous Fenton-like catalyst. The strong H_2O_2-activating

capability of Cu-Cy nanoparticles showed promising applications in the oxidative degradation of recalcitrant organic contaminants. We found that the degradation rate can be further enhanced when excited by MWs. Radical scavenging experiments revealed that the dominant species responsible for the degradation of the pollutants were •OH. Additionally, the result of the recycling study suggested that Cu-Cy has good stability and recyclability. Our future work will concentrate on further improving the lifetime of the catalyst for its potential application in practical pollutant treatment. Our future work will also identify intermediate and end products. Moreover, the degree of mineralization will be studied in terms of total organic carbon (TOC) removal and chemical oxygen demand (COD) removal.

References

[1] J.A. Imlay, Pathways of oxidative damage, Annual Reviews in Microbiology 57(1) (2003) 395-418.

[2] K. Krumova, G. Cosa, Chapter 1 Overview of Reactive Oxygen Species, Singlet Oxygen: Applications in Biosciences and Nanosciences, Volume 1, The Royal Society of Chemistry2016, pp. 1-21.

[3] H.J.H. Fenton, LXXIII.—Oxidation of tartaric acid in presence of iron, Journal of the Chemical Society, Transactions 65 (1894) 899-910.

[4] B. Yang, Y. Chen, J. Shi, Reactive oxygen species (ROS)-based nanomedicine, Chemical Reviews 119(8) (2019) 4881-4985.

[5] O. Warburg, Beobachtungen über die Oxydationsprozesse im Seeigelei, Zeitschrift für Physiologische Chemie 57 (1908) 1-16.

[6] Z. Tang, P. Zhao, H. Wang, Y. Liu, W. Bu, Biomedicine Meets Fenton Chemistry, Chemical Reviews 121(4) (2021) 1981–2019.

[7] Y. Nosaka, A.Y. Nosaka, Generation and detection of reactive oxygen species in photocatalysis, Chemical Reviews 117(17) (2017) 11302-11336.

[8] R.L. Siegel, K.D. Miller, H.E. Fuchs, A. Jemal, Cancer Statistics, 2021, CA: A Cancer Journal for Clinicians 71(1) (2021) 7-33.

[9] P. Agostinis, K. Berg, K.A. Cengel, T.H. Foster, A.W. Girotti, S.O. Gollnick, S.M. Hahn, M.R. Hamblin, A. Juzeniene, D. Kessel, Photodynamic therapy of cancer: An update, CA: A Cancer Journal for Clinicians 61(4) (2011) 250-281.

[10] Á. Juarranz, P. Jaén, F. Sanz-Rodríguez, J. Cuevas, S. González, Photodynamic therapy of cancer. Basic principles and applications, Clinical and Translational Oncology 10(3) (2008) 148-154.

[11] L. Chudal, N.K. Pandey, J. Phan, O. Johnson, X. Li, W. Chen, Investigation of PPIX-Lipo-MnO_2 to enhance photodynamic therapy by improving tumor hypoxia, Materials Science and Engineering: C 104 (2019) 109979.

[12] D.E. Dolmans, D. Fukumura, R.K. Jain, Photodynamic therapy for cancer, Nature Reviews Cancer 3(5) (2003) 380-387.

[13] R. Ackroyd, C. Kelty, N. Brown, M. Reed, The history of photodetection and photodynamic therapy¶, Photochemistry and Photobiology 74(5) (2001) 656-669.

[14] C. Sibata, V. Colussi, N. Oleinick, T. Kinsella, Photodynamic therapy: a new concept in medical treatment, Brazilian Journal of Medical and Biological Research 33(8) (2000) 869-880.

[15] R.L. Lipson, E.J. Baldes, A.M. Olsen, The use of a derivative of hematoporphyrin in tumor detection, Journal of the National Cancer Institute 26(1) (1961) 1-11.

[16] T.J. Dougherty, G. Grindey, R. Fiel, K.R. Weishaupt, D. Boyle, Photoradiation therapy. II. Cure of animal tumors with hematoporphyrin and light, Journal of the National Cancer Institute 55(1) (1975) 115-121.

[17] T.J. Dougherty, A brief history of clinical photodynamic therapy development at Roswell Park Cancer Institute, Journal of Clinical Laser Medicine & Surgery 14(5) (1996) 219-221.

[18] R.R. Allison, V.S. Bagnato, C.H. Sibata, Future of oncologic photodynamic therapy, Future Oncology 6(6) (2010) 929-940.

[19] R. Baskaran, J. Lee, S.-G. Yang, Clinical development of photodynamic agents and therapeutic applications, Biomaterials Research 22(1) (2018) 1-8.

[20] X. Zheng, Y. Jin, X. Liu, T. Liu, W. Wang, H. Yu, Photoactivatable nanogenerators of reactive species for cancer therapy, Bioactive Materials 6(12) (2021) 4301-4318.

[21] J.-J. Hu, Q. Lei, X.-Z. Zhang, Recent advances in photonanomedicines for enhanced cancer photodynamic therapy, Progress in Materials Science 114 (2020) 100685.

[22] M.H. Raza, S. Siraj, A. Arshad, U. Waheed, F. Aldakheel, S. Alduraywish, M. Arshad, ROS-modulated therapeutic approaches in cancer treatment, Journal of Cancer Research and Clinical Oncology 143(9) (2017) 1789-1809.

[23] D. Trachootham, J. Alexandre, P. Huang, Targeting cancer cells by ROS-mediated mechanisms: a radical therapeutic approach?, Nature Reviews Drug Discovery 8(7) (2009) 579-591.

[24] X. Li, N. Kwon, T. Guo, Z. Liu, J. Yoon, Innovative strategies for hypoxic-tumor photodynamic therapy, Angewandte Chemie International Edition 57(36) (2018) 11522-11531.

[25] J. Hu, Y.a. Tang, A.H. Elmenoufy, H. Xu, Z. Cheng, X. Yang, Nanocomposite-based photodynamic therapy strategies for deep tumor treatment, Small 11(44) (2015) 5860-5887.

[26] R. Weissleder, A clearer vision for in vivo imaging, Nature Biotechnology 19(4) (2001) 316-317.

[27] X. Chu, K. Li, H.Y. Guo, H.B. Zheng, S. Shuda, X.L. Wang, J.Y. Zhang, W. Chen, Y. Zhang, Exploration of graphitic-C_3N_4 quantum dots for microwave-induced photodynamic therapy, ACS Biomaterials Science & Engineering 3(8) (2017) 1836-1844.

[28] X. Chu, L. Mao, O. Johnson, K. Li, J. Phan, Q. Yin, L. Li, J. Zhang, W. Chen, Y. Zhang, Exploration of TiO_2 nanoparticle mediated microdynamic therapy on cancer treatment, Nanomedicine 18 (2019) 272-281.

[29] N.K. Pandey, L. Chudal, J. Phan, L. Lin, O. Johnson, M. Xing, J.P. Liu, H. Li, X. Huang, Y. Shu, W. Chen, A facile method for the synthesis of copper-cysteamine nanoparticles and study of ROS production for cancer treatment, Journal of Materials Chemistry B 7(42) (2019) 6630-6642.

[30] X. Ma, X. Ren, X. Guo, C. Fu, Q. Wu, L. Tan, H. Li, W. Zhang, X. Chen, H. Zhong, Multifunctional iron-based metal−organic framework as biodegradable nanozyme for microwave enhancing dynamic therapy, Biomaterials 214 (2019) 119223.

[31] Q. Wu, N. Xia, D. Long, L. Tan, W. Rao, J. Yu, C. Fu, X. Ren, H. Li, L. Gou, P. Liang, J. Ren, L. Li, X. Meng, Dual-functional supernanoparticles with microwave dynamic therapy and microwave thermal therapy, Nano Letters 19(8) (2019) 5277-5286.

[32] T. Tang, X. Xu, Z. Wang, J. Tian, Y. Yang, C. Ou, H. Bao, T. Liu, Cu_2ZnSnS_4 nanocrystals for microwave thermal and microwave dynamic combination tumor therapy, Chemical Communications 55(87) (2019) 13148-13151.

[33] C. Fu, H. Zhou, L. Tan, Z. Huang, Q. Wu, X. Ren, J. Ren, X. Meng, Microwave-activated Mn-doped zirconium metal–organic framework nanocubes for highly effective combination of microwave dynamic and thermal therapies against cancer, ACS Nano 12(3) (2017) 2201-2210.

[34] M. Yao, L. Ma, L. Li, J. Zhang, R. Lim, W. Chen, Y. Zhang, A new modality for cancer treatment--nanoparticle mediated microwave induced photodynamic therapy, Journal of Biomedical Nanotechnology 12(10) (2016) 1835-1851.

[35] N.K. Pandey, W. Xiong, L. Wang, W. Chen, B. Bui, J. Yang, E. Amador, M. Chen, C. Xing, A.A. Athavale, Aggregation-induced emission luminogens for highly effective microwave dynamic therapy, Bioactive Materials (2021) https://doi.org/10.1016/j.bioactmat.2021.05.031.

[36] M. Yang, J. Li, P. Gu, X. Fan, The application of nanoparticles in cancer immunotherapy: Targeting tumor microenvironment, Bioactive Materials 6(7) (2021) 1973-1987.

[37] M. Yang, T. Yang, C. Mao, Enhancement of photodynamic cancer therapy by physical and chemical factors, Angewandte Chemie International Edition 58(40) (2019) 14066-14080.

[38] K.F. Chu, D.E. Dupuy, Thermal ablation of tumours: biological mechanisms and advances in therapy, Nature Reviews Cancer 14(3) (2014) 199-208.

[39] H. Shi, T. Liu, C. Fu, L. Li, L. Tan, J. Wang, X. Ren, J. Ren, J. Wang, X. Meng, Insights into a microwave susceptible agent for minimally invasive microwave tumor thermal therapy, Biomaterials 44 (2015) 91-102.

[40] D. Long, T. Liu, L. Tan, H. Shi, P. Liang, S. Tang, Q. Wu, J. Yu, J. Dou, X. Meng, Multisynergistic platform for tumor therapy by mild microwave irradiation-activated chemotherapy and enhanced ablation, ACS Nano 10(10) (2016) 9516-9528.

[41] M.G. Lubner, C.L. Brace, J.L. Hinshaw, F.T. Lee, Jr., Microwave tumor ablation: mechanism of action, clinical results, and devices, Journal of Vascular and Interventional Radiology 21(8 Suppl) (2010) S192-S203.

[42] H. Wang, E. Zhao, J.W. Lam, B.Z. Tang, AIE luminogens: emission brightened by aggregation, Materials Today 18(7) (2015) 365-377.

[43] Y. Hong, J.W. Lam, B.Z. Tang, Aggregation-induced emission, Chemical Society Reviews 40(11) (2011) 5361-5388.

[44] J. Mei, Y. Hong, J.W. Lam, A. Qin, Y. Tang, B.Z. Tang, Aggregation-induced emission: the whole is more brilliant than the parts, Advanced Materials 26(31) (2014) 5429-5479.

[45] M. Li, Y. Gao, Y. Yuan, Y. Wu, Z. Song, B.Z. Tang, B. Liu, Q.C. Zheng, One-step formulation of targeted aggregation-induced emission dots for image-guided photodynamic therapy of cholangiocarcinoma, ACS Nano 11(4) (2017) 3922-3932.

[46] Z. Liu, H. Zou, Z. Zhao, P. Zhang, G.-G. Shan, R.T. Kwok, J.W. Lam, L. Zheng, B.Z. Tang, Tuning organelle specificity and photodynamic therapy efficiency by molecular function design, ACS Nano 13(10) (2019) 11283-11293.

[47] Y. Li, Q. Wu, M. Kang, N. Song, D. Wang, B.Z. Tang, Boosting the photodynamic therapy efficiency by using stimuli-responsive and AIE-featured nanoparticles, Biomaterials 232 (2020) 119749.

[48] S. Lv, X. Chen, Y. Ye, S. Yin, J. Cheng, M. Xia, Rice hull/$MnFe_2O_4$ composite: Preparation, characterization and its rapid microwave-assisted COD removal for organic wastewater, Journal of Hazardous Materials 171(1-3) (2009) 634-639.

[49] K.E. Haque, Microwave energy for mineral treatment processes—a brief review, International Journal of Mineral Processing 57(1) (1999) 1-24.

[50] C.O. Kappe, Controlled microwave heating in modern organic synthesis, Angewandte Chemie International Edition 43(46) (2004) 6250-6284.

[51] X. Quan, Y.B. Zhang, S. Chen, Y.Z. Zhao, F.L. Yang, Generation of hydroxyl radical in aqueous solution by microwave energy using activated carbon as catalyst and its potential in removal of persistent organic substances, Journal of Molecular Catalysis A: Chemical 263(1-2) (2007) 216-222.

[52] S. An, G. Zhang, T. Wang, W. Zhang, K. Li, C. Song, J.T. Miller, S. Miao, J. Wang, X. Guo, High-density ultra-small clusters and single-atom Fe sites embedded in graphitic carbon nitride (g-C_3N_4) for highly efficient catalytic advanced oxidation processes, ACS Nano 12(9) (2018) 9441-9450.

[53] C.-C. Wang, J.-R. Li, X.-L. Lv, Y.-Q. Zhang, G. Guo, Photocatalytic organic pollutants degradation in metal–organic frameworks, Energy & Environmental Science 7(9) (2014) 2831-2867.

[54] D. Wang, T. Silbaugh, R. Pfeffer, Y. Lin, Removal of emulsified oil from water by inverse fluidization of hydrophobic aerogels, Powder Technology 203(2) (2010) 298-309.

[55] E. Brillas, I. Sirés, M.A. Oturan, Electro-Fenton process and related electrochemical technologies based on Fenton's reaction chemistry, Chemical Reviews 109(12) (2009) 6570-6631.

[56] T. Yao, Y. Qi, Y. Mei, Y. Yang, R. Aleisa, X. Tong, J. Wu, One-step preparation of reduced graphene oxide aerogel loaded with mesoporous copper ferrite nanocubes: A highly efficient catalyst in microwave-assisted Fenton reaction, Journal of Hazardous Materials 378 (2019) 120712.

[57] A.D. Bokare, W. Choi, Review of iron-free Fenton-like systems for activating H_2O_2 in advanced oxidation processes, Journal of Hazardous Materials 275 (2014) 121-135.

[58] B.C. Hodges, E.L. Cates, J.-H. Kim, Challenges and prospects of advanced oxidation water treatment processes using catalytic nanomaterials, Nature Nanotechnology 13(8) (2018) 642-650.

[59] D. Mantzavinos, E. Psillakis, Enhancement of biodegradability of industrial wastewaters by chemical oxidation pre-treatment, Journal of Chemical Technology and Biotechnology 79(5) (2004) 431-454.

[60] S. Li, G. Zhang, P. Wang, H. Zheng, Y. Zheng, Microwave-enhanced Mn-Fenton process for the removal of BPA in water, Chemical Engineering Journal 294 (2016) 371-379.

[61] Y. Wang, Y. Ding, D. Yao, H. Dong, C. Ji, J. Wu, Y. Hu, A. Yuan, Copper-Based Nanoscale Coordination Polymers Augmented Tumor Radioimmunotherapy for Immunogenic Cell Death Induction and T-Cell Infiltration, Small 17(8) (2021) 2006231.

[62] L. Ma, W. Chen, G. Schatte, W. Wang, A.G. Joly, Y. Huang, R. Sammynaiken, M. Hossu, A new Cu–cysteamine complex: structure and optical properties, Journal of Materials Chemistry C 2(21) (2014) 4239-4246.

[63] X. Huang, F. Wan, L. Ma, J.B. Phan, R.X. Lim, C. Li, J. Chen, J. Deng, Y. Li, W. Chen, M. He, Investigation of copper-cysteamine nanoparticles as a new photosensitizer for anti-hepatocellular carcinoma, Cancer Biology & Therapy 20(6) (2019) 812-825.

[64] S. Shrestha, J. Wu, B. Sah, A. Vanasse, L.N. Cooper, L. Ma, G. Li, H. Zheng, W. Chen, M.P. Antosh, X-ray Induced Photodynamic Therapy with pH-Low Insertion Peptide Targeted Copper-Cysteamine Nanoparticles in Mice, PNAS 116(34) (2019) 16823–16828.

[65] L. Ma, X. Zou, W. Chen, A New X-ray Induced Nanoparticle Photosensitizers for Cancer Treatment, Journal of Biomedical Nanotechnology 10 (2014) 1501-1508.

[66] B. Sah, J. Wu, A. Vanasse, N.K. Pandey, L. Chudal, Z. Huang, W. Song, H. Yu, L. Ma, W. Chen, Effects of Nanoparticle Size and Radiation Energy on Copper-Cysteamine Nanoparticles for X-ray Induced Photodynamic Therapy, Nanomaterials 10(6) (2020) 1087.

[67] Q. Zhang, X. Guo, Y. Cheng, L. Chudal, N.K. Pandey, J. Zhang, L. Ma, Q. Xi, G. Yang, Y. Chen, Use of copper-cysteamine nanoparticles to simultaneously enable radiotherapy, oxidative therapy and immunotherapy for melanoma treatment, Signal Transduction and Targeted Therapy 5(1) (2020) 1-3.

[68] P. Wang, X. Wang, L. Ma, S. Sahi, L. Li, X. Wang, Q. Wang, Y. Chen, W. Chen, Q. Liu, Nanosonosensitization by using copper-cysteamine nanoparticles augmented sonodynamic cancer treatment, Particle & Particle Systems Characterization 35(4) (2018) 1700378.

[69] X. Zhen, L. Chudal, N.K. Pandey, J. Phan, X. Ran, E. Amandor, X. Huang, O. Johnson, Y. Ran, W. Chen, A powerful combination of copper-cysteamine nanoparticles with potassium iodide for bacterial destruction, Materials Science and Engineering: C 110 (2020) 110659.

[70] L. Chudal, N.K. Pandey, J. Phan, O. Johnson, L. Lin, H. Yu, Y. Shu, Z. Huang, M. Xing, J.P. Liu, M.-L. Chen, W. Chen, Copper-cysteamine nanoparticles as a heterogeneous Fenton-like catalyst for highly selective cancer treatment ACS Applied Bio Materials 3(3) (2020) 1804-1814.

[71] Y. Chang, F. Wu, N.K. Pandey, L. Chudal, M. Xing, X. Zhang, L. Nguyen, X. Liu, J.P. Liu, W. Chen, Combination of Disulfiram and Copper–Cysteamine Nanoparticles for an Enhanced Antitumor Effect on Esophageal Cancer, ACS Applied Bio Materials 3(10) (2020) 7147-7157.

[72] Y. Huang, X. Zheng, S. Feng, Z. Guo, S. Liang, Enhancement of rhodamine B removal by modifying activated carbon developed from Lythrum salicaria L. with pyruvic acid, Colloids and Surfaces A: Physicochemical and Engineering Aspects 489 (2016) 154-162.

[73] M. Sundararajan, V. Sailaja, L.J. Kennedy, J.J. Vijaya, Photocatalytic degradation of rhodamine B under visible light using nanostructured zinc doped cobalt ferrite: Kinetics and mechanism, Ceramics International 43(1) (2017) 540-548.

[74] S. Chowdhury, K.G. Bhattacharyya, Use of Cu(II)-incorporated zeolite Y for decolourization of dyes in water: a case study with aqueous methylene blue and Congo red, SN Applied Sciences 1(1) (2019) 87.

[75] H.R. Pouretedal, A. Norozi, M.H. Keshavarz, A. Semnani, Nanoparticles of zinc sulfide doped with manganese, nickel and copper as nanophotocatalyst in the degradation of organic dyes, Journal of Hazardous Materials 162(2-3) (2009) 674-681.

[76] V. Yadav, P. Verma, H. Sharma, S. Tripathy, V.K. Saini, Photodegradation of 4-nitrophenol over B-doped TiO_2 nanostructure: effect of dopant concentration, kinetics, and mechanism, Environmental Science and Pollution Research 27(10) (2020) 10966–10980.

[77] A.A. Kassem, H.N. Abdelhamid, D.M. Fouad, S.A. Ibrahim, Catalytic reduction of 4-nitrophenol using copper terephthalate frameworks and CuO@C composite, Journal of Environmental Chemical Engineering 9(1) (2021) 104401.

[78] R.W. Sun, D.L. Ma, E.L. Wong, C.M. Che, Some uses of transition metal complexes as anti-cancer and anti-HIV agents, Dalton Transactions (43) (2007) 4884-4892.

[79] K. Kalyanasundaram, M. Gratzel, Applications of functionalized transition metal complexes in photonic and optoelectronic devices, Coordination Chemistry Reviews 177(1) (1998) 347-414.

[80] D.L. Ma, H.Z. He, K.H. Leung, D.S. Chan, C.H. Leung, Bioactive luminescent transition-metal complexes for biomedical applications, Angewandte Chemie International Edition 52(30) (2013) 7666-7682.

[81] S. Rafique, M. Idrees, A. Nasim, H. Akbar, A. Athar, Transition metal complexes as potential therapeutic agents, Biotechnology and Molecular Biology Reviews 5(2) (2010) 38-45.

[82] V. Fernandez-Moreira, F.L. Thorp-Greenwood, M.P. Coogan, Application of d^6 transition metal complexes in fluorescence cell imaging, Chemical Communications 46(2) (2010) 186-202.

[83] A. Warra, Transition metal complexes and their application in drugs and cosmetics-a Review, Journal of Chemical and Pharmaceutical Research 3(4) (2011) 951-958.

[84] V.W. Yam, K.M. Wong, Luminescent metal complexes of d^6, d^8 and d^{10} transition metal centres, Chemical communications 47(42) (2011) 11579-11592.

[85] A. Laviecambot, M. Cantuel, Y. Leydet, G. Jonusauskas, D. Bassani, N. McClenaghan, Improving the photophysical properties of copper(I) bis(phenanthroline) complexes, Coordination Chemistry Reviews 252(23-24) (2008) 2572-2584.

[86] N. Armaroli, G. Accorsi, F. Cardinali, A. Listorti, Photochemistry and photophysics of coordination compounds: Copper, Photochemistry and Photophysics of Coordination Compounds I, Springer2007, pp. 69-115.

[87] C.W. Hsu, C.C. Lin, M.W. Chung, Y. Chi, G.H. Lee, P.T. Chou, C.H. Chang, P.Y. Chen, Systematic investigation of the metal-structure-photophysics relationship of emissive d^{10}-complexes of group 11 elements: the prospect of application in organic light emitting devices, Journal of the American Chemical Society 133(31) (2011) 12085-12099.

[88] S. Ahmad, A. Espinosa, T. Ahmad, M. Sohail, A.A. Isab, M. Saleem, A. Hameed, M. Monim-ul-Mehboob, E. de las Heras, Synthesis, theoretical calculations and antimicrobial studies of copper(I) complexes of cysteamine, cysteine and 2-mercaptonicotinic acid, Polyhedron 85 (2015) 239-245.

[89] Z. Salehi, R. Parish, R.G. Pritchard, A polymeric cationic copper(I) complex involving a quadruply bridging, zwitterionic thiolate ligand: $\{[Cu_8Cl_6(SCH_2CH_2NH_3)_6]Cl_2\}_n$, Journal of the Chemical Society, Dalton Transactions (22) (1997) 4241-4246.

[90] R.V. Parish, Z. Salehi, R.G. Pritchard, Five-coordinate sulfur in a polymeric copper(I) thiolate complex, Angewandte Chemie-International Edition in English 36(3) (1997) 251-253.

[91] Z. Liu, L. Xiong, G. Ouyang, L. Ma, S. Sahi, K. Wang, L. Lin, H. Huang, X. Miao, W. Chen, Y. Wen, Investigation of Copper Cysteamine Nanoparticles as a New Type of Radiosensitiers for Colorectal Carcinoma Treatment, Scientific Reports 7(1) (2017) 9290.

[92] L. Shi, P. Liu, J. Wu, L. Ma, H. Zheng, M.P. Antosh, H. Zhang, B. Wang, W. Chen, X. Wang, The effectiveness and safety of X-PDT for cutaneous squamous cell carcinoma and melanoma, Nanomedicine 14(15) (2019) 2027-2043.

[93] L. Huang, L. Ma, W. Xuan, X. Zhen, H. Zheng, W. Chen, M.R. Hamblin, Exploration of Copper-Cysteamine Nanoparticles as a New Type of Agents for Antimicrobial Photodynamic Inactivation, Journal of Biomedical Nanotechnology 15(10) (2019) 2142-2148.

[94] H.Y. Guo, J.Z.Y. Zhang, L. Ma, J.L. Chavez, L.Q. Yin, H. Gao, Z.L. Tang, W. Chen, A Non-rare-Earth Ions Self-Activated White Emitting Phosphor under Single Excitation, Advanced Functional Materials 25(44) (2015) 6833-6838.

[95] W. Dai, Y. Lei, M. Xu, P. Zhao, Z. Zhang, J. Zhou, Rare-Earth Free Self-Activated Graphene Quantum Dots and Copper-Cysteamine Phosphors for Enhanced White Light-Emitting-Diodes under Single Excitation, Scientific Reports 7(1) (2017) 12872.

[96] J. Wang, J. Yi, Cancer cell killing via ROS: to increase or decrease, that is the question, Cancer Biology & Therapy 7(12) (2008) 1875-1884.

[97] A.T. Dharmaraja, Role of Reactive Oxygen Species (ROS) in Therapeutics and Drug Resistance in Cancer and Bacteria, Journal of Medicinal Chemistry 60(8) (2017) 3221-3240.

[98] I. Kraljić, S.E. Mohsni, A new method for the detection of singlet oxygen in aqueous solutions, Photochemistry and Photobiology 28(4-5) (1978) 577-581.

[99] J.P. Crow, Dichlorodihydrofluorescein and dihydrorhodamine 123 are sensitive indicators of peroxynitritein vitro: implications for intracellular measurement of reactive nitrogen and oxygen species, Nitric oxide 1(2) (1997) 145-157.

[100] A. Gomes, E. Fernandes, J.L. Lima, Fluorescence probes used for detection of reactive oxygen species, Journal of Biochemical and Biophysical Methods 65(2-3) (2005) 45-80.

[101] J. Zhang, Y. Nosaka, Quantitative Detection of OH Radicals for Investigating the Reaction Mechanism of Various Visible-Light TiO_2 Photocatalysts in Aqueous Suspension, The Journal of Physical Chemistry C 117(3) (2013) 1383-1391.

[102] M. Kurzyp, H.A. Girard, Y. Cheref, E. Brun, C. Sicard-Roselli, S. Saada, J.C. Arnault, Hydroxyl radical production induced by plasma hydrogenated nanodiamonds under X-ray irradiation, Chemical Communications 53(7) (2017) 1237-1240.

[103] N.R. Paudel, D. Shvydka, E.I. Parsai, A novel property of gold nanoparticles: Free radical generation under microwave irradiation, Medical Physics 43(4) (2016) 1598-1602.

[104] L.W. Aurand, N.H. Boone, G.G. Giddings, Superoxide and Singlet Oxygen in Milk Lipid Peroxidation, Journal of Dairy Science 60(3) (1977) 363-369.

[105] C. Schweitzer, R. Schmidt, Physical mechanisms of generation and deactivation of singlet oxygen, Chemical Reviews 103(5) (2003) 1685-757.

[106] Q. Cai, J. Xu, D. Yang, Y. Dai, G. Yang, C. Zhong, S. Gai, F. He, P. Yang, Polypyrrole-coated UCNPs@mSiO_2@ZnO nanocomposite for combined photodynamic and photothermal therapy, Journal of Materials Chemistry B 6(48) (2018) 8148-8162.

[107] K. Zheng, M.I. Setyawati, T.P. Lim, D.T. Leong, J. Xie, Antimicrobial Cluster Bombs: Silver Nanoclusters Packed with Daptomycin, ACS Nano 10(8) (2016) 7934-7942.

[108] K. Zheng, M.I. Setyawati, D.T. Leong, J. Xie, Antimicrobial Gold Nanoclusters, ACS Nano 11(7) (2017) 6904-6910.

[109] K.Y. Zheng, X. Yuan, N. Goswami, Q.B. Zhang, J.P. Xie, Recent advances in the synthesis, characterization, and biomedical applications of ultrasmall thiolated silver nanoclusters, RSC Advances 4(105) (2014) 60581-60596.

[110] I. Chakraborty, T. Udayabhaskararao, G.K. Deepesh, T. Pradeep, Sunlight mediated synthesis and antibacterial properties of monolayer protected silver clusters, Journal of Materials Chemistry B 1(33) (2013) 4059-4064.

[111] C. Vergely, V. Maupoil, G. Clermont, A. Bril, L. Rochette, Identification and quantification of free radicals during myocardial ischemia and reperfusion using electron paramagnetic resonance spectroscopy, Archives of Biochemistry and Biophysics 420(2) (2003) 209-216.

[112] G. Louit, S. Foley, J. Cabillic, H. Coffigny, F. Taran, A. Valleix, J.P. Renault, S. Pin, The reaction of coumarin with the OH radical revisited: hydroxylation product analysis determined by fluorescence and chromatography, Radiation Physics and Chemistry 72(2-3) (2005) 119-124.

[113] N.N. Cheng, Z. Starkewolf, R.A. Davidson, A. Sharmah, C. Lee, J. Lien, T. Guo, Chemical enhancement by nanomaterials under X-ray irradiation, Journal of the American Chemical Society 134(4) (2012) 1950-1953.

[114] R.A. Davidson, T. Guo, An Example of X-ray Nanochemistry: SERS Investigation of Polymerization Enhanced by Nanostructures under X-ray Irradiation, The Journal of Physical Chemistry Letters 3(22) (2012) 3271-3275.

[115] V.I. Bruskov, L.V. Malakhova, Z.K. Masalimov, A.V. Chernikov, Heat-induced formation of reactive oxygen species and 8-oxoguanine, a biomarker of damage to DNA, Nucleic Acids Research 30(6) (2002) 1354-1363.

[116] C. Yang, J. Uertz, D. Yohan, B.D. Chithrani, Peptide modified gold nanoparticles for improved cellular uptake, nuclear transport, and intracellular retention, Nanoscale 6(20) (2014) 12026-12033.

[117] C. Yang, J. Uertz, D.B. Chithrani, Colloidal Gold-Mediated Delivery of Bleomycin for Improved Outcome in Chemotherapy, Nanomaterials 6(3) (2016) 48.

[118] T. Bezabeh, M.R. Mowat, L. Jarolim, A.H. Greenberg, I.C. Smith, Detection of drug-induced apoptosis and necrosis in human cervical carcinoma cells using ^{1}H NMR spectroscopy, Cell Death & Differentiation 8(3) (2001) 219-24.

[119] S. Mukhopadhyay, R.S. Singh, R.P. Paitandi, G. Sharma, B. Koch, D.S. Pandey, Influence of substituents on DNA and protein binding of cyclometalated Ir(III) complexes and anticancer activity, Dalton Transactions 46(26) (2017) 8572-8585.

[120] M. Ganeshpandian, R. Loganathan, E. Suresh, A. Riyasdeen, M.A. Akbarsha, M. Palaniandavar, New ruthenium(II) arene complexes of anthracenyl-appended diazacycloalkanes: effect of ligand intercalation and hydrophobicity on DNA and protein binding and cleavage and cytotoxicity, Dalton Transactions 43(3) (2014) 1203-19.

[121] R.P. Paitandi, S. Mukhopadhyay, R.S. Singh, V. Sharma, S.M. Mobin, D.S. Pandey, Anticancer Activity of Iridium(III) Complexes Based on a Pyrazole-Appended Quinoline-Based BODIPY, Inorganic Chemistry 56(20) (2017) 12232-12247.

[122] G. Majno, I. Joris, Apoptosis, oncosis, and necrosis. An overview of cell death, The American Journal of Pathology 146(1) (1995) 3-15.

[123] S. Li, L. Tan, X. Meng, Nanoscale metal-organic frameworks: synthesis, biocompatibility, imaging applications, and thermal and dynamic therapy of tumors, Advanced Functional Materials 30(13) (2020) 1908924.

[124] J. Mei, N.L. Leung, R.T. Kwok, J.W. Lam, B.Z. Tang, Aggregation-induced emission: together we shine, united we soar!, Chemical Reviews 115(21) (2015) 11718-11940.

[125] M. Gao, B.Z. Tang, AIE-based cancer theranostics, Coordination Chemistry Reviews 402 (2020) 213076.

[126] J. Qian, B.Z. Tang, AIE luminogens for bioimaging and theranostics: from organelles to animals, Chem 3(1) (2017) 56-91.

[127] A.J. Moy, J.W. Tunnell, Combinatorial immunotherapy and nanoparticle mediated hyperthermia, Advanced Drug Delivery Reviews 114 (2017) 175-183.

[128] H.A. Albarqi, L.H. Wong, C. Schumann, F.Y. Sabei, T. Korzun, X. Li, M.N. Hansen, P. Dhagat, A.S. Moses, O. Taratula, Biocompatible nanoclusters with high heating efficiency for systemically delivered magnetic hyperthermia, ACS Nano 13(6) (2019) 6383-6395.

[129] X. Zhang, J. Tang, C. Li, Y. Lu, L. Cheng, J. Liu, A targeting black phosphorus nanoparticle based immune cells nano-regulator for photodynamic/photothermal and photo-immunotherapy, Bioactive Materials 6(2) (2021) 472-489.

[130] C.J. Simon, D.E. Dupuy, W.W. Mayo-Smith, Microwave ablation: principles and applications, Radiographics 25(suppl_1) (2005) S69-S83.

[131] W. Xiong, L. Wang, X. Chen, H. Tang, D. Cao, G. Zhang, W. Chen, Pyridinium-substituted tetraphenylethylene salts-based photosensitizers by varying counter anions: highly efficient photodynamic therapy for cancer cell ablation and bacteria inactivation, Journal of Materials Chemistry B 8(24) (2020) 5234-5244.

[132] L. Chen, Y. Chen, W. Zhou, J. Li, Y. Zhang, Y. Liu, Mitochondrion-targeting chemiluminescent ternary supramolecular assembly for in situ photodynamic therapy, Chemical Communications 56(62) (2020) 8857-8860.

[133] A. Fedyaeva, A. Stepanov, I. Lyubushkina, T. Pobezhimova, E. Rikhvanov, Heat shock induces production of reactive oxygen species and increases inner mitochondrial membrane potential in winter wheat cells, Biochemistry (Moscow) 79(11) (2014) 1202-1210.

[134] T. Wu, J. Huang, Y. Yan, Self-assembly of aggregation-induced-emission molecules, Chemistry–An Asian Journal 14(6) (2019) 730-750.

[135] B.S. Li, X. Huang, H. Li, W. Xia, S. Xue, Q. Xia, B.Z. Tang, Solvent and surface/interface effect on the hierarchical assemblies of chiral aggregation-induced emitting molecules, Langmuir 35(10) (2019) 3805-3813.

[136] A. Abdal Dayem, M.K. Hossain, S.B. Lee, K. Kim, S.K. Saha, G.-M. Yang, H.Y. Choi, S.-G. Cho, The role of reactive oxygen species (ROS) in the biological activities of metallic nanoparticles, International Journal of Molecular Sciences 18(1) (2017) 120.

[137] K. Mothilal, J.J. Inbaraj, R. Gandhidasan, R. Murugesan, Photosensitization with anthraquinone derivatives: optical and EPR spin trapping studies of photogeneration of reactive oxygen species, Journal of Photochemistry and Photobiology A: Chemistry 162(1) (2004) 9-16.

[138] E.A. Mayeda, A.J. Bard, Production of singlet oxygen in electrogenerated radical ion electron transfer reactions, Journal of the American Chemical Society 95(19) (1973) 6223-6226.

[139] D. Min, J. Boff, Chemistry and reaction of singlet oxygen in foods, Comprehensive Reviews in Food Science and Food Safety 1(2) (2002) 58-72.

[140] D.R. Kearns, Physical and chemical properties of singlet molecular oxygen, Chemical Reviews 71(4) (1971) 395-427.

[141] A.U. Khan, Singlet molecular oxygen from superoxide anion and sensitized fluorescence of organic molecules, Science 168(3930) (1970) 476-477.

[142] G. Afreen, M. Shoeb, S. Upadhyayula, Effectiveness of reactive oxygen species generated from rGO/CdS QD heterostructure for photodegradation and disinfection of pollutants in waste water, Materials Science and Engineering: C 108 (2020) 110372.

[143] J. Wang, S. Wang, Reactive species in advanced oxidation processes: Formation, identification and reaction mechanism, Chemical Engineering Journal 401 (2020) 126158.

[144] J.F. Turrens, Mitochondrial formation of reactive oxygen species, The Journal of Physiology 552(2) (2003) 335-344.

[145] K. Kouno, C. Ogawa, Y. Shimomura, H. Yano, Y. Ueda, Interaction of imidazole derivatives with electron acceptors. II. Reaction products of imidazole with p-benzoquinone, Chemical and Pharmaceutical Bulletin 29(2) (1981) 301-307.

[146] S. Bae, D. Kim, W. Lee, Degradation of diclofenac by pyrite catalyzed Fenton oxidation, Applied Catalysis B: Environmental 134 (2013) 93-102.

[147] X. Luo, H. Hu, Z. Pan, F. Pei, H. Qian, K. Miao, S. Guo, W. Wang, G. Feng, Efficient and stable catalysis of hollow Cu_9S_5 nanospheres in the Fenton-like degradation of organic dyes, Journal of Hazardous Materials 396 (2020) 122735.

[148] R. Gao, X. Mei, D. Yan, R. Liang, M. Wei, Nano-photosensitizer based on layered double hydroxide and isophthalic acid for singlet oxygenation and photodynamic therapy, Nature Communications 9(1) (2018) 1-10.

[149] W. He, Y. Liu, W.G. Wamer, J.-J. Yin, Electron spin resonance spectroscopy for the study of nanomaterial-mediated generation of reactive oxygen species, Journal of Food and Drug Analysis 22(1) (2014) 49-63.

[150] T. Mosmann, Rapid colorimetric assay for cellular growth and survival: application to proliferation and cytotoxicity assays, Journal of Immunological Methods 65(1-2) (1983) 55-63.

[151] D. Bratosin, L. Mitrofan, C. Palii, J. Estaquier, J. Montreuil, Novel fluorescence assay using calcein-AM for the determination of human erythrocyte viability and aging, Cytometry Part A: The Journal of the International Society for Analytical Cytology 66(1) (2005) 78-84.

[152] N. Wang, T. Zheng, J. Jiang, P. Wang, Cu(II)–Fe(II)–H_2O_2 oxidative removal of 3-nitroaniline in water under microwave irradiation, Chemical Engineering Journal 260 (2015) 386-392.

[153] J. Sanz, J. Lombrana, A. De Luis, M. Ortueta, F. Varona, Microwave and Fenton's reagent oxidation of wastewater, Environmental Chemistry Letters 1(1) (2003) 45-50.

[154] S. Shahin, V.P. Singh, R.K. Shukla, A. Dhawan, R.K. Gangwar, S.P. Singh, C.M. Chaturvedi, 2.45 GHz microwave irradiation-induced oxidative stress affects implantation or pregnancy in mice, Mus musculus, Applied Biochemistry and Biotechnology 169(5) (2013) 1727-1751.

[155] N. Getoff, Generation of $^1O_2$ by microwave discharge and some characteristic reactions: A short review, Radiation Physics and Chemistry 45(4) (1995) 609-614.

[156] H. Lin, Y. Shen, D. Chen, L. Lin, B.C. Wilson, B. Li, S. Xie, Feasibility study on quantitative measurements of singlet oxygen generation using singlet oxygen sensor green, Journal of Fluorescence 23(1) (2013) 41-47.

[157] G.N. De Iuliis, R.J. Newey, B.V. King, R.J. Aitken, Mobile phone radiation induces reactive oxygen species production and DNA damage in human spermatozoa in vitro, PloS ONE 4(7) (2009) e6446.

[158] Y.-S. Lu, B.-T. Huang, Y.-X. Huang, Reactive oxygen species formation and apoptosis in human peripheral blood mononuclear cell induced by 900 MHz mobile phone radiation, Oxidative Medicine and Cellular Longevity 2012 (2012) 740280.

[159] J. Friedman, S. Kraus, Y. Hauptman, Y. Schiff, R. Seger, Mechanism of short-term ERK activation by electromagnetic fields at mobile phone frequencies, Biochemical Journal 405(3) (2007) 559-568.

[160] M. Wu, Z. Liu, W. Zhang, An ultra-stable bio-inspired bacteriochlorin analogue for hypoxia-tolerant photodynamic therapy, Chemical Science 12 (2021) 1295-1301.

[161] S.K. Kansal, A. Kumari, Potential of M. oleifera for the treatment of water and wastewater, Chemical Reviews 114(9) (2014) 4993-5010.

[162] A. Shah, S. Shahzad, A. Munir, M.N. Nadagouda, G.S. Khan, D.F. Shams, D.D. Dionysiou, U.A. Rana, Micelles as soil and water decontamination agents, Chemical Reviews 116(10) (2016) 6042-6074.

[163] Y. Zhu, R. Zhu, Y. Xi, J. Zhu, G. Zhu, H. He, Strategies for enhancing the heterogeneous Fenton catalytic reactivity: A review, Applied Catalysis B: Environmental 255 (2019) 117739.

[164] A. Jaén-Gil, G. Buttiglieri, A. Benito, J.A. Mir-Tutusaus, R. Gonzalez-Olmos, G. Caminal, D. Barceló, M. Sarrà, S. Rodriguez-Mozaz, Combining biological processes with UV/H_2O_2 for metoprolol and metoprolol acid removal in hospital wastewater, Chemical Engineering Journal 404 (2021) 126482.

[165] B. Ma, S. Wang, F. Liu, S. Zhang, J. Duan, Z. Li, Y. Kong, Y. Sang, H. Liu, W. Bu, Self-assembled copper–amino acid nanoparticles for in situ glutathione "and" H_2O_2 sequentially triggered chemodynamic therapy, Journal of the American Chemical Society 141(2) (2018) 849-857.

[166] J. Li, A.N. Pham, R. Dai, Z. Wang, T.D. Waite, Recent advances in Cu-Fenton systems for the treatment of industrial wastewaters: Role of Cu complexes and Cu composites, Journal of Hazardous Materials 392 (2020) 122261.

[167] F. Gao, L. Zhu, Y. Wang, H. Xie, J. Li, Room temperature facile synthesis of Cu_2Se hexagonal nanoplates array film and its high photodegradation activity to methyl blue with the assistance of H_2O_2, Materials Letters 183 (2016) 425-428.

[168] L. Kang, M. Zhou, H. Zhou, F. Zhang, Z. Zhong, W. Xing, Controlled synthesis of Cu_2O microcrystals in membrane dispersion reactor and comparative activity in heterogeneous Fenton application, Powder Technology 343 (2019) 847-854.

[169] B. Sun, H. Li, X. Li, X. Liu, C. Zhang, H. Xu, X. Zhao, Degradation of organic dyes over Fenton-like Cu_2O–Cu/C catalysts, Industrial & Engineering Chemistry Research 57(42) (2018) 14011-14021.

[170] J. Ma, N. Jia, C. Shen, W. Liu, Y. Wen, Stable cuprous active sites in Cu^+-graphitic carbon nitride: Structure analysis and performance in Fenton-like reactions, Journal of Hazardous Materials 378 (2019) 120782.

[171] M. Yao, L. Ma, L. Li, J. Zhang, R.X. Lim, W. Chen, Y. Zhang, A new modality for cancer treatment—nanoparticle mediated microwave induced photodynamic therapy, Journal of Biomedical Nanotechnology 12 (2016) 1835–1851.

[172] X. Chen, J. Liu, Y. Li, N.K. Pandey, T. Chen, L. Wang, E.H. Amador, W. Chen, F. Liu, E. Xiao, Study of copper-cysteamine based X-ray induced photodynamic therapy and its effects on cancer cell proliferation and migration in a clinical mimic setting, Bioactive Materials (2021) https://doi.org/10.1016/j.bioactmat.2021.05.016.

[173] Y. Wang, N.D. Alkhaldi, N.K. Pandey, L. Chudal, L. Wang, L. Lin, M. Zhang, Y. Yong, E.H. Amador, M.N. Huda, A New Type of Cuprous-Cysteamine Sensitizers: Synthesis, Optical Properties and Potential Applications, Materials Today Physics (2021) 100435.

[174] H. Zhu, R. Jiang, L. Xiao, Y. Chang, Y. Guan, X. Li, G. Zeng, Photocatalytic decolorization and degradation of Congo Red on innovative crosslinked chitosan/nano-CdS composite catalyst under visible light irradiation, Journal of Hazardous Materials 169(1-3) (2009) 933-940.

[175] S. Erdemoglu, S.K. Aksu, F. Sayilkan, B. Izgi, M. Asilturk, H. Sayilkan, F. Frimmel, S. Gucer, Photocatalytic degradation of Congo Red by hydrothermally synthesized nanocrystalline TiO_2 and identification of degradation products by LC-MS, Journal of Hazardous Materials 155(3) (2008) 469-76.

[176] E. Basturk, M. Karatas, Decolorization of antraquinone dye Reactive Blue 181 solution by UV/H_2O_2 process, Journal of Photochemistry and Photobiology A: Chemistry 299 (2015) 67-72.

[177] F.X. Chen, S.L. Xie, X.L. Huang, X.H. Qiu, Ionothermal synthesis of Fe_3O_4 magnetic nanoparticles as efficient heterogeneous Fenton-like catalysts for degradation of organic pollutants with H_2O_2, Journal of Hazardous Materials 322 (2017) 152-162.

[178] C. Cai, Z.Y. Zhang, J. Liu, N. Shan, H. Zhang, D.D. Dionysiou, Visible light-assisted heterogeneous Fenton with $ZnFe_2O_4$ for the degradation of Orange II in water, Applied Catalysis B: Environmental 182 (2016) 456-468.

[179] Y.Y. Sheng, Y. Sun, J. Xu, J. Zhang, Y.F. Han, Fenton-like degradation of rhodamine B over highly durable Cu-embedded alumina: Kinetics and mechanism, Aiche Journal 64(2) (2018) 538-549.

[180] P.R. Gogate, A.B. Pandit, A review of imperative technologies for wastewater treatment I: oxidation technologies at ambient conditions, Advances in Environmental Research 8(3-4) (2004) 501-551.

[181] P.V. Nidheesh, R. Gandhimathi, S. Velmathi, N.S. Sanjini, Magnetite as a heterogeneous electro Fenton catalyst for the removal of Rhodamine B from aqueous solution, RSC Advances 4(11) (2014) 5698-5708.

[182] J. Wang, S. Wang, Effect of inorganic anions on the performance of advanced oxidation processes for degradation of organic contaminants, Chemical Engineering Journal 411 (2021) 128392.

[183] S. Ai, X. Guo, L. Zhao, D. Yang, H. Ding, Zeolitic imidazolate framework-supported Prussian blue analogues as an efficient Fenton-like catalyst for activation of peroxymonosulfate, Colloids and Surfaces A: Physicochemical and Engineering Aspects 581 (2019) 123796.

[184] L.L. Zhang, Y.L. Nie, C. Hu, J.H. Qu, Enhanced Fenton degradation of Rhodamine B over nanoscaled Cu-doped $LaTiO_3$ perovskite, Applied Catalysis B: Environmental 125 (2012) 418-424.

[185] W. Luo, L.H. Zhu, N. Wang, H.Q. Tang, M.J. Cao, Y.B. She, Efficient Removal of Organic Pollutants with Magnetic Nanoscaled $BiFeO_3$ as a Reusable Heterogeneous Fenton-Like Catalyst, Environmental Science & Technology 44(5) (2010) 1786-1791.

[186] L. Wolski, A. Walkowiak, M. Ziolek, Formation of reactive oxygen species upon interaction of Au/ZnO with H_2O_2 and their activity in methylene blue degradation, Catalysis Today 333 (2019) 54-62.

[187] S. Xing, Z. Zhou, Z. Ma, Y. Wu, Characterization and reactivity of $Fe_3O_4/FeMnO_x$ core/shell nanoparticles for methylene blue discoloration with H_2O_2, Applied Catalysis B: Environmental 107(3-4) (2011) 386-392.

[188] N. Zhang, E.P. Tsang, J. Chen, Z. Fang, D. Zhao, Critical role of oxygen vacancies in heterogeneous Fenton oxidation over ceria-based catalysts, Journal of colloid and interface science 558 (2020) 163-172.

[189] R. Srivastava, M.U.A. Prathap, R. Ore, Morphologically controlled synthesis of copper oxides and their catalytic applications in the synthesis of propargylamine and oxidative

degradation of methylene blue, Colloids and Surfaces A: Physicochemical and Engineering Aspects 392(1) (2011) 271-282.

[190] M.Q. Yang, J.H. He, Fine tuning of the morphology of copper oxide nanostructures and their application in ambient degradation of methylene blue, Journal of Colloid and Interface Science 355(1) (2011) 15-22.

[191] M. Xing, W. Xu, C. Dong, Y. Bai, J. Zeng, Y. Zhou, J. Zhang, Y. Yin, Metal sulfides as excellent co-catalysts for H_2O_2 decomposition in advanced oxidation processes, Chem 4(6) (2018) 1359-1372.

[192] G. Sangami, R. Nirmala, H. Kim, N. Dharmaraj, Photodegradation of 4-nitrophenol using cadmium sulphide nanoparticles, Journal of Nanoscience and Nanotechnology 14(3) (2014) 2299-2306.

[193] Y. Wang, Y. Tan, N.K. Pandey, L. Chudal, E. Amador, L. Sun, S. Zhang, M. Zhang, W. Chen, FeS_2 Loaded Porous SiO_2 Ball as a Tweezers Recoverable Heterogeneous Fenton Catalyst with Enhanced Recyclability, Journal of Nanoscience and Nanotechnology 21(3) (2021) 1474-1482.

[194] Y. Wang, H. Zhao, J. Gao, G. Zhao, Y. Zhang, Y. Zhang, Rapid mineralization of azo-dye wastewater by microwave synergistic electro-Fenton oxidation process, The Journal of Physical Chemistry C 116(13) (2012) 7457-7463.